



PREPARATION AND PERFORMANCE OF FUNCTIONAL MATERIALS FOR  
CATALYST AND ENERGY APPLICATIONS



A Thesis Submitted in Partial Fulfillment of the Requirements  
for Doctor of Philosophy (POLYMER SCIENCE AND ENGINEERING)  
Department of MATERIALS SCIENCE AND ENGINEERING  
Graduate School, Silpakorn University  
Academic Year 2017  
Copyright of Graduate School, Silpakorn University

Preparation and performance of functional materials for catalyst and energy applications



วิทยานิพนธ์นี้เป็นส่วนหนึ่งของการศึกษาตามหลักสูตรปรัชญาดุษฎีบัณฑิต  
สาขาวิชาวิทยาการและวิศวกรรมพอลิเมอร์ แบบ 1.1 ปรัชญาดุษฎีบัณฑิต

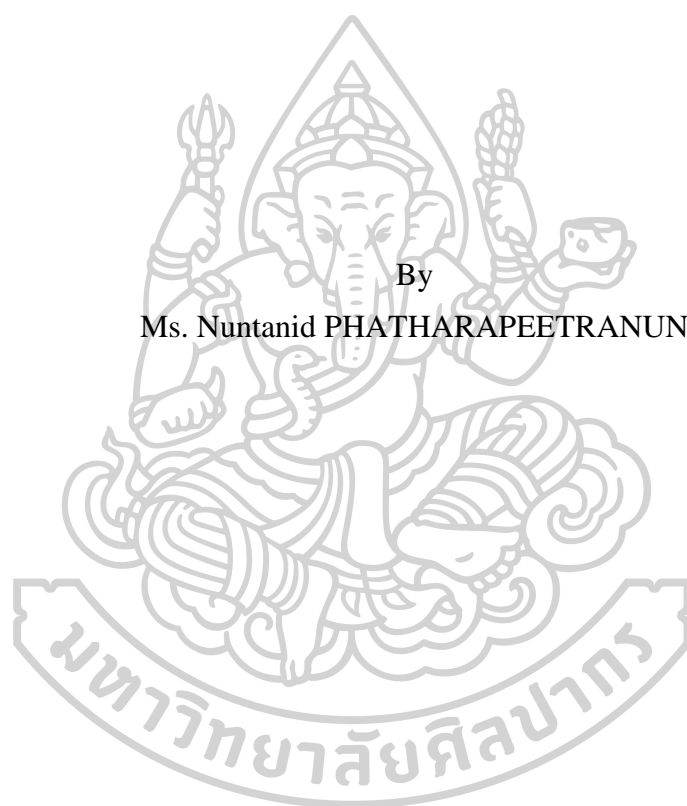
ภาควิชาวิทยาการและวิศวกรรมวัสดุ

บัณฑิตวิทยาลัย มหาวิทยาลัยศิลปากร

ปีการศึกษา 2560

ลิขสิทธิ์ของบัณฑิตวิทยาลัย มหาวิทยาลัยศิลปากร

PREPARATION AND PERFORMANCE OF FUNCTIONAL  
MATERIALS FOR CATALYST AND ENERGY APPLICATIONS



A Thesis Submitted in Partial Fulfillment of the Requirements  
for Doctor of Philosophy (POLYMER SCIENCE AND ENGINEERING)  
Department of MATERIALS SCIENCE AND ENGINEERING  
Graduate School, Silpakorn University  
Academic Year 2017  
Copyright of Graduate School, Silpakorn University

Title	Preparation and performance of functional materials for catalyst and energy applications
By	Nuntanid PHATHARAPEETRANUN
Field of Study	(POLYMER SCIENCE AND ENGINEERING)
Advisor	Bussarin Ksapabutr

---

Graduate School Silpakorn University in Partial Fulfillment of the Requirements for the Doctor of Philosophy

..... Dean of graduate school  
(Associate Professor Jurairat Nunthanid, Ph.D.)

Approved by

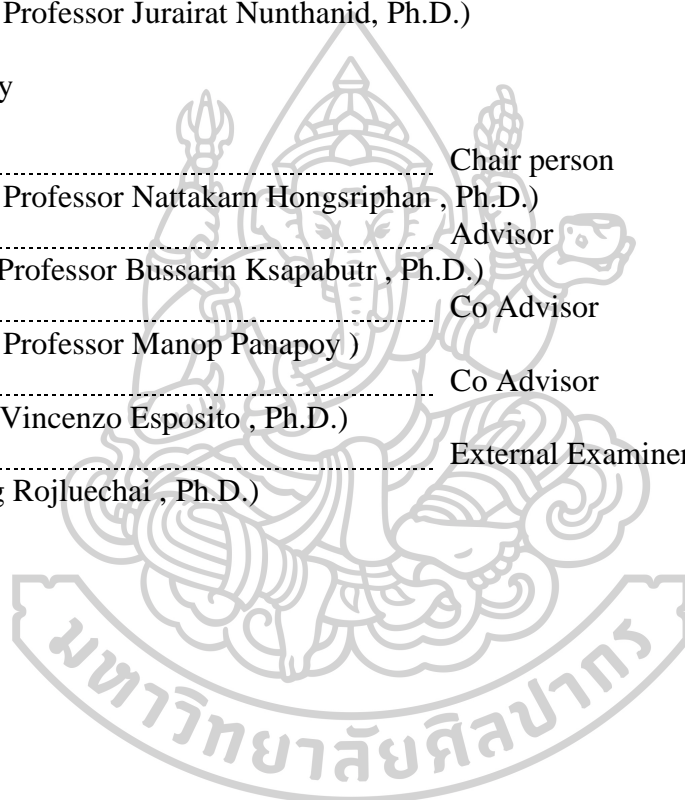
..... Chair person  
(Associate Professor Nattakarn Hongstriphan , Ph.D.)

..... Advisor  
(Assistant Professor Bussarin Ksapabutr , Ph.D.)

..... Co Advisor  
(Associate Professor Manop Panapoy )

..... Co Advisor  
(Professor Vincenzo Esposito , Ph.D.)

..... External Examiner  
( Siriphong Rojluechai , Ph.D.)



57402801 : Major (POLYMER SCIENCE AND ENGINEERING)

Keyword : Functional materials, Photocatalyst, Supercapacitor, Dielectric, Sol-gel, 3D-printing

MS. NUNTANID PHATHARAPEETRANUN : PREPARATION AND PERFORMANCE OF FUNCTIONAL MATERIALS FOR CATALYST AND ENERGY APPLICATIONS THESIS ADVISOR : ASSISTANT PROFESSOR BUSSARIN KSAPABUTR, Ph.D.

The main aim of this dissertation is to study the preparation and performance of functional materials, including coconut shell based activated carbon (ACCS), coconut shell based activated carbon-titania hybrid (ACCS/TiO<sub>2</sub>), and titania-based ceramics/polymer hybrid materials for energy storage and photocatalyst applications. Coconut shell was successfully utilized as a low cost alternative material for the electrode in supercapacitor device and the removal of textile dye. The highly porous activated carbon with high specific surface area was prepared from agricultural coconut shell waste as precursor with KOH activation at impregnation ratio of 3:1 and carbonization at 800 °C. For electrochemical test, the obtained ACCS electrode showed excellent electrochemical behavior with a maximum specific capacitance of 149.65 F/g at a current density of 0.5 A/g and the highest energy density of 4.64 Wh/kg at the power density of 239.66 W/kg. Furthermore, this resulting electrode also showed good rate capability and the specific capacitance decreased less than 35% (65% capacity retention) as the current density was raised from 0.5 to 4 A/g. For photocatalytic test, TiO<sub>2</sub>/activated carbon double-layered film photocatalysts were successfully fabricated using an electrophoretic deposition technique without additives. Pristine TiO<sub>2</sub> powder was synthesized by solvothermal process. The obtained hybrid catalyst film showed the maximum efficiency for removing methylene blue of about 97% at 60 min under UV light. The hybrid film system has an advantage for wastewater treatment in practical applications because it is easy to separate from the process and reusable with relatively high photocatalytic efficiency. Furthermore, the titania-based ceramics-polymer hybrid materials; bismuth titanate/polyvinylpyrrolidone (BiT/PVP) and barium titanate/poly-(vinylidene fluoride) (BTNFs/PVDF) nanohybrids, were prepared and their performances were tested. The nanohybrids were synthesized and fabricated using the sol-gel chemistry followed by extrusion based 3D-printing (FDM) technique. The BiT/PVP sample with 3.0 vol. % of PVP exhibited a good printing speed range enlarged over 50% of pure BiT gel. The obtained results are useful for optimizing and setting the 3D printing parameters. Moreover, the anisotropic 3D BTNFs/PVDF nanohybrids were successfully fabricated via FDM technique and BTNFs were synthesized via sol-gel followed by electrospinning method. The BTNFs/PVDF 3D-nanohybrids with 20 vol. % BTNFs, exhibited the highest dielectric constant in cross-direction around 200 at frequency of 1 kHz at room temperature, vs 13 of the neat PVDF materials. This FDM technique indicated great potential for future development in high-k ferroelectric ceramic/polymer composites with controllable anisotropic properties.

## ACKNOWLEDGEMENTS

Firstly, I would like to express my sincere gratitude to my advisor and co-advisor: Asst. Prof. Dr. Bussarin Ksapabutr, Assoc. Prof. Manop Panapoy and Prof. Dr. Vincenzo Esposito for the continuous support of my Ph.D study and related research, for their patience, motivation, and immense knowledge. Their guidance helps me in all the time of doing research and writing of this thesis.

My gratitude extends to my thesis committee members: Assoc. Prof. Dr. Nattakarn Hongsririphan (Chairman) and Dr. Siriphong Rojluetchai for their insightful comments and challenge questions, which incited me to widen my research from various perspectives.

My sincere thanks also go to Mr. Attapol Eiamsila who always supports all my testing and facility in Silpakorn University.

Besides, I would like to thank Dr. Debora Marani, who helps me to improve my academic writing skills and always takes care of me during my time in Denmark. Without her precious support, it would not be possible to conduct this work.

This dissertation would not have been possible without funding from the Royal Golden Jubilee PhD Program (RGJ-PhD Program) (grant no. PHD/0116/2557).

Last but not the least, I would like to thank my family: my mother, my husband, and my little girl “Ai-Aun” for supporting and inspiring me. Thank you for being beside me all along the way.

Nuntanid PHATHARAPEETRANUN

# TABLE OF CONTENTS

	<b>Page</b>
ABSTRACT.....	D
ACKNOWLEDGEMENTS.....	E
TABLE OF CONTENTS.....	F
LIST OF FIGURES .....	I
LIST OF TABLES .....	L
Chapter 1 Introduction .....	1
1.1 Statements and significance of the problem .....	1
1.1.1 Electrical energy conversion and storage technology .....	3
1.1.1.1 Rechargeable battery .....	3
1.1.1.2 Conventional capacitor .....	5
1.1.1.3 Supercapacitor .....	8
1.1.1.3.1 Supercapacitor construction.....	9
1.1.1.3.2 Type of supercapacitors .....	11
1.1.1.3.3 Electrode materials for supercapacitor .....	15
1.1.2 Environmental and pollution treatment technology .....	16
1.1.2.1 Mechanism of photocatalysis .....	17
1.1.2.2 Photocatalyst in wastewater application.....	18
1.2 Objectives of the work.....	20
Chapter 2 Literature Review .....	21
2.1 Functional materials in energy storage applications.....	21
2.1.1 Activated carbons from bio-based precursors .....	21
2.1.1.1 Carbonization process .....	22
2.1.1.2 Activation process .....	23
2.1.2 Activated carbons as electrode materials for supercapacitors.....	25
2.1.3 Activated carbon-metal oxide hybrid material as electrode for supercapacitors .....	29

2.1.4 Carbon nanotube as electrode for supercapacitors .....	30
2.1.5 Carbon nanotube-metal oxide hybrid materials as electrode for supercapacitors .....	32
2.1.6 Ceramic-polymer composites as dielectric material in energy application .....	34
2.2 Functional materials in photocatalyst applications.....	38
2.2.1 Activated carbon as catalyst supported for photocatalyst in wastewater application .....	39
Chapter 3 Coconut Shell Based Activated Carbon and Coconut Shell Based Activated Carbon-TiO <sub>2</sub> Composite Catalysts for Energy Storage and Photocatalyst Applications .....	42
3.1 Abstract.....	42
3.2 Introduction.....	43
3.3 Experimental.....	44
3.3.1 Preparation of coconut shell based activated carbon (ACCS) .....	44
3.3.2 Characterization and testing of coconut shell based activated carbon as electrode material for supercapacitor application .....	45
3.3.3 Preparation of TiO <sub>2</sub> /activated carbon hybrid catalysts for photocatalyst application .....	45
3.3.4 Characterization and testing of TiO <sub>2</sub> /activated carbon hybrid catalysts for photocatalyst application .....	46
3.4 Results and discussion .....	46
3.4.1 Characterization of coconut shell based activated carbon.....	46
3.4.2 Electrochemical behavior of coconut shell based activated carbon as electrode material for supercapacitor .....	49
3.4.3 Characterization of the synthesized TiO <sub>2</sub> and TiO <sub>2</sub> /coconut shell based activated carbon photocatalyst .....	55
3.5 Conclusions.....	65
3.6 References.....	66
Chapter 4 Assembly Three Dimensional Bismuth Titanate (3D-BIT) by Extrusion- Based Fuse Deposition Modeling Technique .....	71
4.1 Abstract.....	71

4.2 Introduction.....	71
4.3 Experimental.....	72
4.3.1 Materials and procedures.....	72
4.3.2 Preparation of bismuth titanate ( $\text{Bi}_4\text{Ti}_3\text{O}_{12}$ ) via sol-gel technique.....	72
4.3.3 Fabrication of three-dimensional bismuth titanate ( $\text{Bi}_4\text{Ti}_3\text{O}_{12}$ ) by FDM technique .....	74
4.4 Results and discussion .....	75
4.4.1 Phase composition of $\text{Bi}_4\text{Ti}_3\text{O}_{12}$ (BiT).....	75
4.4.2 Rheology of BiT compounds .....	77
4.5 Conclusions.....	80
4.6 References.....	81
Chapter 5 3D Printed Barium Titanate/poly(vinylidene fluoride) Nano-hybrid with Anisotropic Dielectric Properties.....	83
5.1 Abstract.....	83
5.2 Introduction.....	83
5.3 Experimental.....	85
5.3.1 Materials.....	85
5.3.2 Electrospun of $\text{BaTiO}_3$ nanofibers (BTNFs) .....	85
5.3.3 Preparation of anisotropic BTNFs/PVDF 3D-nanohybrid dielectric materials .....	86
5.3.4 Dielectric property measurement .....	88
5.3.5 Methods .....	88
5.4 Results and discussion .....	89
5.5 Conclusions.....	107
5.6 References.....	107
Chapter 6 Summary .....	113
REFERENCES .....	115
VITA.....	132

## LIST OF FIGURES

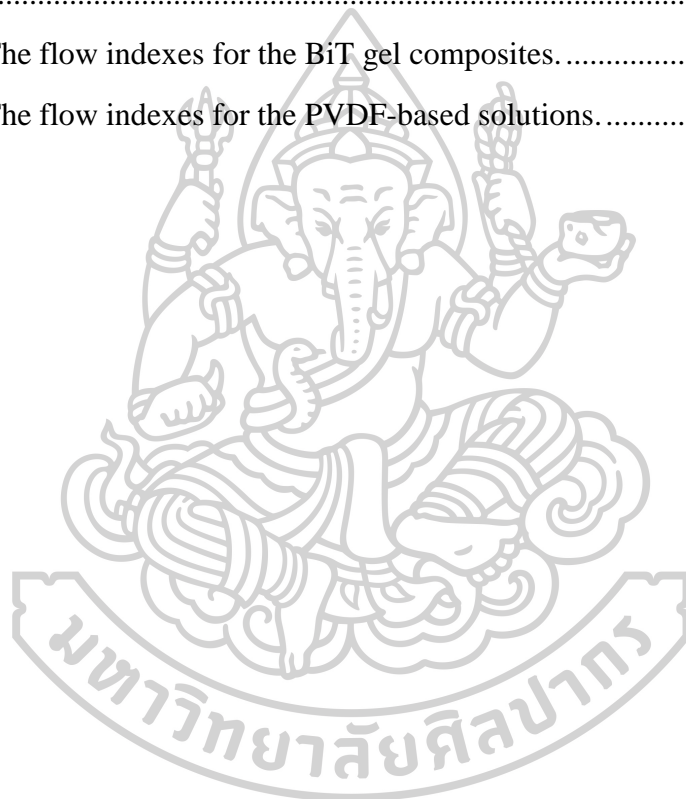
Figures	Page
Figure 1.1 World energy consumption by region, 2015-2050 .....	1
Figure 1.2 World energy consumption by energy source, 1990-2040 .....	2
Figure 1.3 Charge-discharge mechanism of rechargeable battery.....	4
Figure 1.4 Polar molecule in dielectric materials (a) without electric field and (b) under applied electric field (E). .....	7
Figure 1.5 Ragone plot showing energy density vs. power density for various devices. ....	9
Figure 1.6 Type of supercapacitors .....	11
Figure 1.7 Electrical double layer capacitors (EDLCs) structure .....	12
Figure 1.8 Mechanism of energy storage in electrical double layer capacitor .....	14
Figure 1.9 Advantages of photocatalyst.....	17
Figure 1.10 Mechanism of photocatalysis process .....	18
Figure 2.1 Lignocellulosic biomass structure; (a) cellulose, (b) hemicellulose and (c) lignin.....	22
Figure 3.1 SEM micrographs of (a) AC-C and (b) AC-S.....	47
Figure 3.2 N <sub>2</sub> adsorption-desorption isotherms of AC-C and AC-S.....	48
Figure 3.3 Raman spectra of AC-C and AC-S.....	49
Figure 3.4 Two-electrode system: the CV curves of AC-S and AC-C electrodes at a scan rate of 5 mV/s in H <sub>2</sub> SO <sub>4</sub> electrolyte solution.....	50
Figure 3.5 Two electrode system: the CV curves of (a) AC-C electrode and (b) AC-S electrode at various scan ranging from 5 to 100 mV/s. ....	51
Figure 3.6 Two electrode system: specific capacitances of AC-C and AC-S electrodes as a function at various scan ranging from 5 to 100 mV/s.....	52
Figure 3.7 Galvanostatic charge-discharge curves of symmetric supercapacitor of the AC-S electrode at different current densities. ....	53
Figure 3.8 Ragone plot of the AC-S electrode carbonized at 800 °C measured at various current densities in H <sub>2</sub> SO <sub>4</sub> electrolyte solution. The inset shows specific capacitance dependence on current density. ....	55

Figure 3.9 XRD patterns of the samples (a) P25 and (b) ST. ....	56
Figure 3.10 TEM micrographs of the samples (a) P25 and (b) ST. ....	57
Figure 3.11 SEM images of (a) P25 film, (b) ST film, (c) P25/AC-S film, and (d) ST/AC-S film. ....	58
Figure 3.12 Langmuir adsorption isotherm fitted to the experimental data for MB adsorption onto various films. ....	60
Figure 3.13 (a) The relation between absorbance and wavelength as a function of illumination time of the ST/AC-S film for the photocatalytic degradation of MB and (b) photocatalytic efficiency for MB degradation using various photocatalysts. ....	62
Figure 3.14 Degradation kinetics of MB dye over different film catalysts. ....	64
Figure 3.15 Reusability of the ST/AC-S film for five cycles. ....	65
Figure 4.1 Schematic diagram of the synthesis of bismuth titanate ( $\text{Bi}_4\text{Ti}_3\text{O}_{12}$ ) via sol-gel technique ....	73
Figure 4.2 XRD patterns of $\text{Bi}_4\text{Ti}_3\text{O}_{12}$ powders prepared from the sol-gel method after calcination at different temperatures. ....	76
Figure 4.3 Linear shrinkage curve of calcined BiT from room temperature to 850°C. ....	77
Figure 4.4 (a) Viscosity plot and (b) the corresponding double logarithmic power law plot for the complete series of BiT showing the flow index (slope). ....	78
Figure 4.5 (a) Processing window for BiT gel and its composite for 1.4 mm of extrusion nozzle and (b) Extrusion based FDM technique for BiT ....	80
Figure 5.1 TG/DTA profiles of the as synthesized fibers. ....	90
Figure 5.2 X-ray diffraction patterns of the as synthesized fibers and calcined BTNFs for 1 h at different temperatures. ....	91
Figure 5.3 FE-SEM In-lens SE1 images of (a), (b) as synthesized fibers and (c), (d) BTNFs calcined at 800 °C for 1 h. ....	92
Figure 5.4 X-ray diffraction patterns of the BTNFs/PVDF 3D-nanohybrid materials at different % vol. of BTNFs. ....	93
Figure 5.5 Extrusion based FDM technique for BTNFs-PVDF dielectric materials...	94
Figure 5.6 (a) Fibers alignment of BTNFs/PVDF materials printed by 2.5 mm of nozzle diameter 0.6% vol BTNFs; (b) 4.5% vol. BTNFs; (c) 20% vol. BTNFs and (d) 20% vol. BTNFs printed by 1.2 mm. of nozzle diameter. ....	95

Figure 5.7 (a) In-lens (b) SE2 detector raw image slices from the middle of the vertical axis in the volume in figure 5.8 (a) .....	96
Figure 5.8 (a) A discretised skeleton of BTNFs segmented from the PVDF. Individual fragments of the BTNFs have been assigned random colours for visualisation. (b) Orientation of individual BTNF fragments plotted on a unit sphere, b and c are approximately aligned.....	98
Figure 5.9 Stacked histograms of BTNF fragment angular (elevation) deviation from the extrusion direction as a function of fragment length. The histogram counts of elevation angle are weighted by fragment length. Note: the random distribution is on an arbitrary count scale. ....	99
Figure 5.10 (a) Viscosity plot and the corresponding of the pure PVDF and BTNFs/PVDF nanohybrids, (b) double logarithmic power law plot for the complete series of PVDF-based solutions showing the flow index (slope), and (c) double logarithmic power law plot for the PVDF solutions.....	101
Figure 5.11 Frequency dependence of dielectric constant of (a) BTNFs/PVDF 3D-nanohybrid dielectric materials in cross direction (CD, $k_{\perp}$ ), (b) in parallel direction (PD, $k_{\parallel}$ ), .....	103
Figure 5.12 Dielectric constant of anisotropic BTNFs/PVDF 3D-nanohybrid dielectric materials at 100 Hz, 1 kHz and 10 kHz at room temperature.....	104
Figure 5.13 (a) Dielectric constant comparison between the 3D printed BTNFs/PVDF composites and the reported PVDF/BaTiO <sub>3</sub> composites at 1 kHz, room temperature and (b) Dielectric constant at 1 kHz from experiment vs predicted value from model equations .....	106

## LIST OF TABLES

Tables	Page
Table 1.1 Advantages and disadvantages of conventional capacitors .....	8
Table 3.1 Phase content, crystallite size and $S_{BET}$ of the samples P25 and ST.....	56
Table 3.2 Langmuir parameter and specific surface area of various films. ....	61
Table 3.3 The photocatalytic parameters for MB removal using various photocatalyst films. ....	63
Table 4.1 The flow indexes for the BiT gel composites. ....	79
Table 5.1 The flow indexes for the PVDF-based solutions. ....	102



## Chapter 1

### Introduction

#### 1.1 Statements and significance of the problem

Energy is fundamental to the quality of human living. It is a key feature for driving modern societies and global economic development such as transportations, telecommunications, constructions, and industrials. From the U.S. Energy Information Administration's projection data, by the year 2050, world-wide energy demand is predicted to be at least 28% of today's level. The major reasons are the rapid growth of emerging economies and population expansion among developing countries or non-OECD nations (OECD: Organization for Economic Cooperation and Development). Meanwhile, energy consumption within OECD nations is forecasted to remain stable (Figure 1.1) [1].

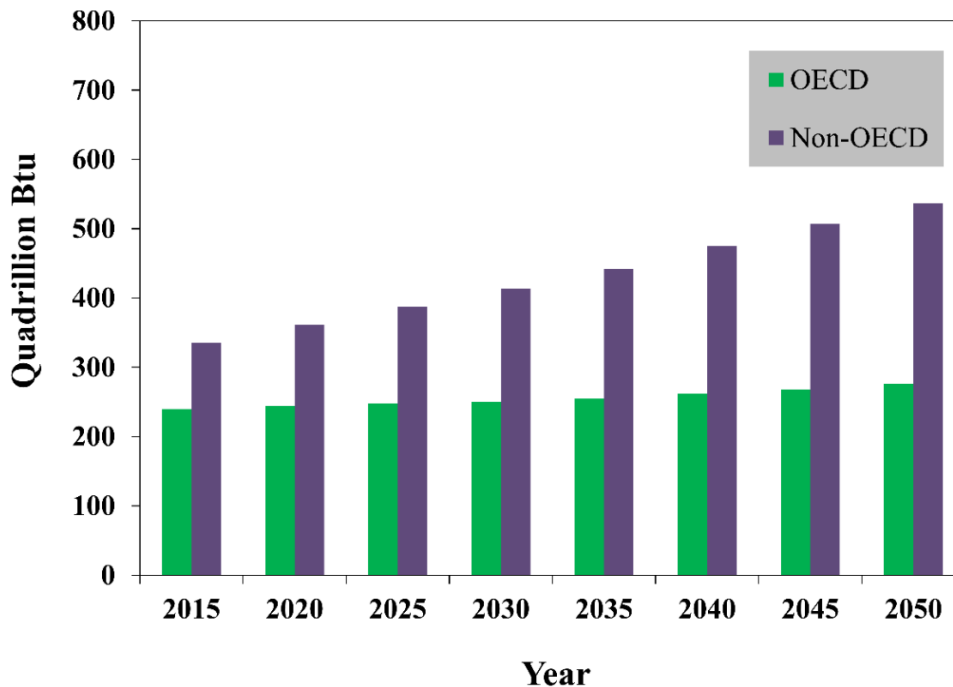


Figure 1.1 World energy consumption by region, 2015-2050 [1].

On the basis of energy sources (Figure 1.2), fossil fuels (e.g. liquid fuels, natural gas, and coal) continue to be the most consumable energy source which are expected to be 78% of total world energy consumption in 2040 [1]. In fact, the global fossil fuel sources especially oil and others liquid fuels will be depleted in the near future [2]. The fast expansion within the development countries not only affects the decrease in the fossil fuel-based energy but also generates the serious environmental problems such as global warming, acid rain, and air/water/soil pollutions. It is well-known that environmental conditions can influence the quality of life, both directly; through water, soil and air contamination, and indirectly; through the change of ecosystems and biodiversity [3].

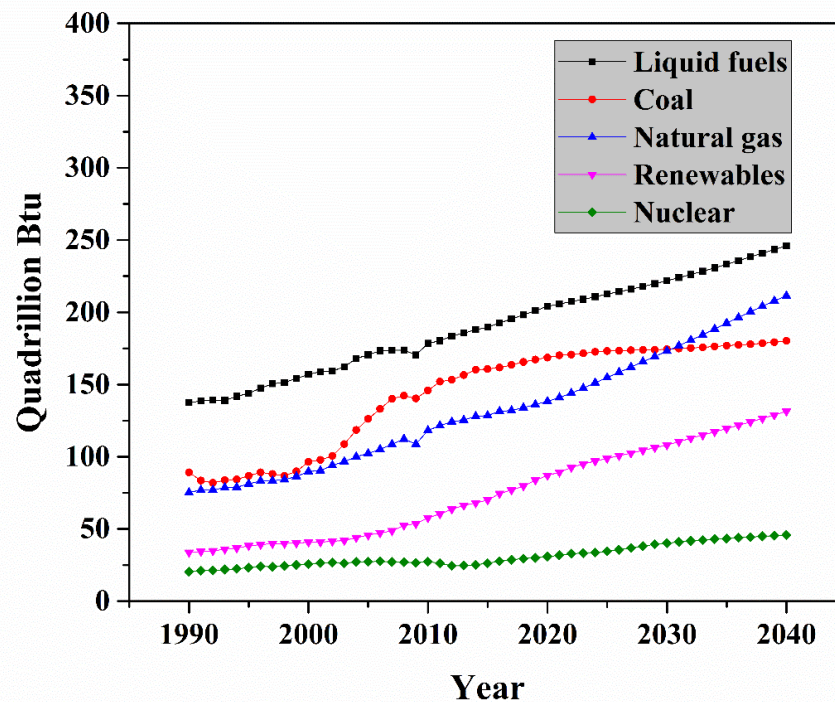


Figure 1.2 World energy consumption by energy source, 1990-2040 [1].

Regarding to these serious problems, many countries are recognized and implemented the relating strategies and policies in order to promote the use of alternatively renewable clean energy from non-fossil fuels source. To comply with this approach, several industries such as vehicles, mobile phones, and other electronic portable devices have been paying a great attention on energy conservation and

emission reduction technology. For example, car manufacturers have been working on the development of hybrid and electrical vehicles (EV car). Some of European countries announced to stop selling petrol cars and 100% replaced by EV car in these couple years [4]. Interestingly, Thailand Board of Investment (BOI) launched a great attractive promotion for investors to invest on EVs technology in Thailand, including three major parts; electric vehicles, EV parts (e.g. battery, traction motor, etc.), and battery charger stations. The incentive levels are varied by various technologies applied in EVs [5]. It has been recognized that the essential part in EVs is energy storage unit. In order to drive in longer distance with less charging time, it really needs the excellent energy storage devices.

Recently, many researchers have been studying the development of functional materials for energy storage devices and catalyst applications. In this work, we emphasized on the functional materials which have good performance, long-term availability, safe and environmentally friendly system as electrode materials for electrical energy storage and photocatalyst applications [6].

### **1.1.1 Electrical energy conversion and storage technology**

Energy storage system is a device which is used for storing energy. Currently, there are multiple energy storage technologies which can be classified by types of energy (e.g. mechanical energy, chemical energy, and electrical energy). Recently, functional electrode materials have been played a progressively key role in the development of electrode materials for electrical energy storage devices such as rechargeable battery, conventional capacitor and supercapacitors [7].

#### **1.1.1.1 Rechargeable battery**

Rechargeable battery is one of the energy conversion and storage device which produces energy via a series of electrochemical reactions (redox reaction). Each cell of a rechargeable battery consists of two electrodes: anode and cathode, separated by an electrolyte that transfers the ion of the chemical reaction inside the cell. In 1859, the first rechargeable battery was invented by French physicist, “Gaston Plante”. This rechargeable battery is the lead acid cell which consists of lead as anode, lead dioxide as cathode and sulfuric acid as electrolyte [8]. Rechargeable battery and non-rechargeable (primary) battery produce energy in the

same way through electrochemical reaction. However, reaction in rechargeable battery can be reversible.

By supplying outside electrical energy to the cell (charge mechanism) (Figure 1.3(a)), then it can be restored to its original composition. In a discharge cycle (Figure 1.3(b)), the reactions between the metal atoms and electrolytes at the anode create metal ions ( $M^+$ ) and electrons ( $e^-$ ) are called oxidation reaction. The electrons ( $e^-$ ) travel from anode to cathode via external circuit and the metal ions ( $M^+$ ) move from anode pass through the electrolyte and separator to cathode, where they recombine with their electrons ( $e^-$ ) and electrically neutralize, called reduction reaction, the net product is “electricity”. This process will continue to produce electricity until there is no essential substance to generate the redox reaction within battery structure [8, 9].

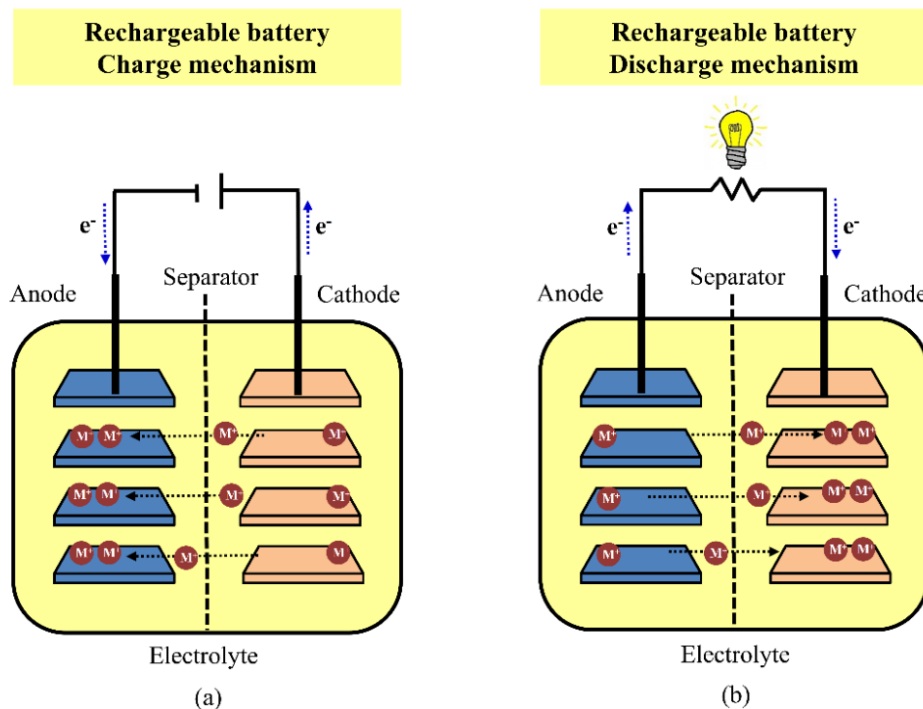


Figure 1.3 Charge-discharge mechanism of rechargeable battery [8].

Nowadays, battery system technology is the most wide-ranging energy storage devices for power system applications [10, 11]. There are different types of batteries which are used in energy storage applications for instant, lead acid battery, nickel cadmium (NiCd) battery, nickel-metal hydride (NiMH) battery, lithium-ion battery and etc.

Among all, owing to the high-power density, high gravimetric and volumetric energy, low self-discharge property, and long cycle life, the lithium-ion battery is most widely used as rechargeable battery. It is often applied in high-performance devices, such as electric cars [12], mobile phones and digital cameras [13]. This kind of rechargeable battery uses lithium metal or lithium compound as anode and lithium cobalt oxide as cathode [14]. However, all technologies have both benefits and drawbacks. Lithium ion technology is the same. There are some disadvantages of this rechargeable battery such as sensitive to high temperature, low conductive, and expensive.

#### **1.1.1.2 Conventional capacitor**

Capacitor is an energy storage device which is generally used in electronic circuits (e.g. television, radio). It works in completely different ways from rechargeable battery; within the battery, it produces electrons through the electrochemical reactions on anode (oxidation) and combines electrons on the cathode (reduction). For capacitor, it can't build up new electron; it only stores electrons from the circuit. When applying a voltage over the two conductors (plates), an electric field is created. Positive charge will accumulate on one plate and negative charge on the other. This kind of mechanism is used for storing energy electrostatically in an applied electric field [15].

Capacitors are widely used in various applications including:

- filtering audio tones
- tuning radio systems
- smoothing out current for a power supply devices
- storing electricity

Capacitor is made from two metallic electrodes separated by a dielectric material (e.g. ceramics, plastics, air) for accumulating an electrical charge under applied electric field. The basic equation relating to the capacitors is [16]:

$$C = \frac{\epsilon_r \epsilon_0 A}{t} \quad (1.1)$$

where  $C$  is the capacitance (F),  $\epsilon_r$  is the relative permittivity of the dielectric material,  $\epsilon_0$  is the permittivity of vacuum ( $8.854 * 10^{-12}$  F/m),  $A$  is the electrode surface area ( $m^2$ ) and  $t$  is the thickness of the dielectric material (m).

From equation (1.1), it's obvious that capacitance can be increased by increasing the electrode surface area and decreasing distance between two electrodes, so it can store more charge and increase the capacitance. All dielectric materials are insulators, but a good dielectric is the one which is easy to polarize. The appropriate dielectric materials are made of polar molecules (e.g. water, conjugated polymer, perovskite ceramic). When the voltage is applied, the polar molecules in dielectric material become polarized (Figure 1.4(b)). At this stage, they arrange their charges opposite to the applied electric field which slightly shift electrons toward the direction of the positive voltage. This effect is very important for capacitors system because the potential is reduced on the plates, resulting in the increase in their capacitance.

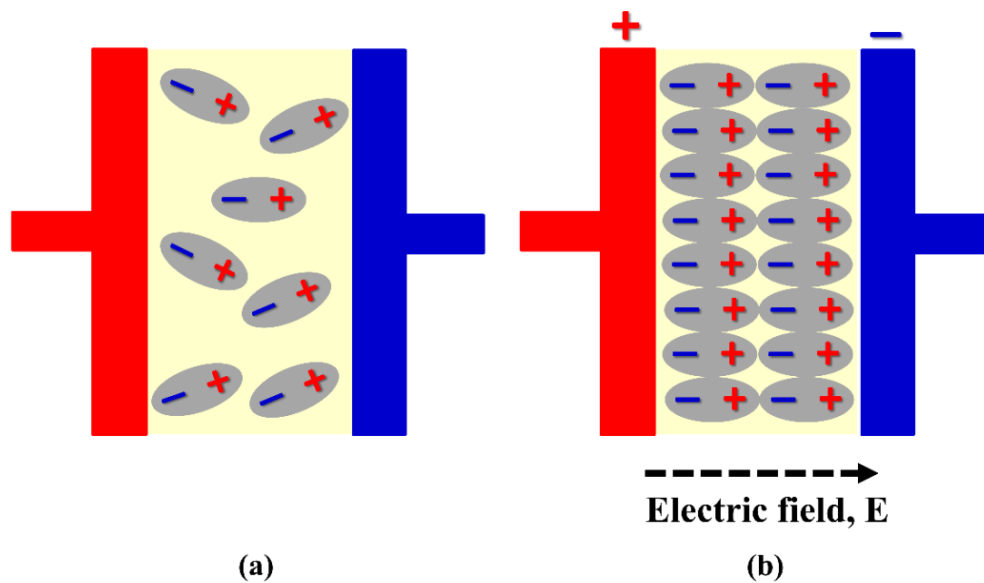


Figure 1.4 Polar molecule in dielectric materials (a) without electric field and (b) under applied electric field (E) [16].

The dielectric constant can dictate kind of capacitors and applications. Typically, conventional capacitors display capacitance level in the range of 0.1 to 1  $\mu\text{F}$  with an applied voltage range of 50 to 400 V. For example;

- mylar is used in timer circuits such as clocks, alarms and counters.
- air is applied in radio tuning circuits.
- glass is suitable for high voltage applications.
- ceramic is typically used for high frequency applications such as X-ray, antennas and MRI machines [15, 17, 18].

Comparison to rechargeable battery, conventional capacitor has excellent properties, as followed in Table 1.1.

Table 1.1 Advantages and disadvantages of conventional capacitors [17].

Advantages of capacitors	Disadvantages of capacitors
<ul style="list-style-type: none"> <li>• quickly charge and discharge</li> <li>• high power output</li> <li>• long life cycle</li> <li>• low maintenance</li> </ul>	<ul style="list-style-type: none"> <li>• low energy density</li> <li>• expensive (high cost per energy storage unit)</li> <li>• high internal losses</li> </ul>

However, conventional capacitor still needs to be improved in term of increasing energy density property, reducing cost per energy unit, and reducing internal loss within capacitor structure.

### 1.1.1.3 Supercapacitor

Apart from conventional capacitor, supercapacitor is one of the energy storage devices, which is accounted for high charge-discharge properties of energy storage device. Supercapacitor has been developed from capacitor in order to close the gap between traditional capacitor (high power density) and rechargeable battery (high energy density), and still keep its long life cycle and excellent charge-discharge behavior (Figure 1.5) [19, 20].

Supercapacitors store energy in the same way with conventional capacitors. They are widely used as uninterruptible power sources in electric vehicles and other digital communications system as energy storage devices [21, 22].

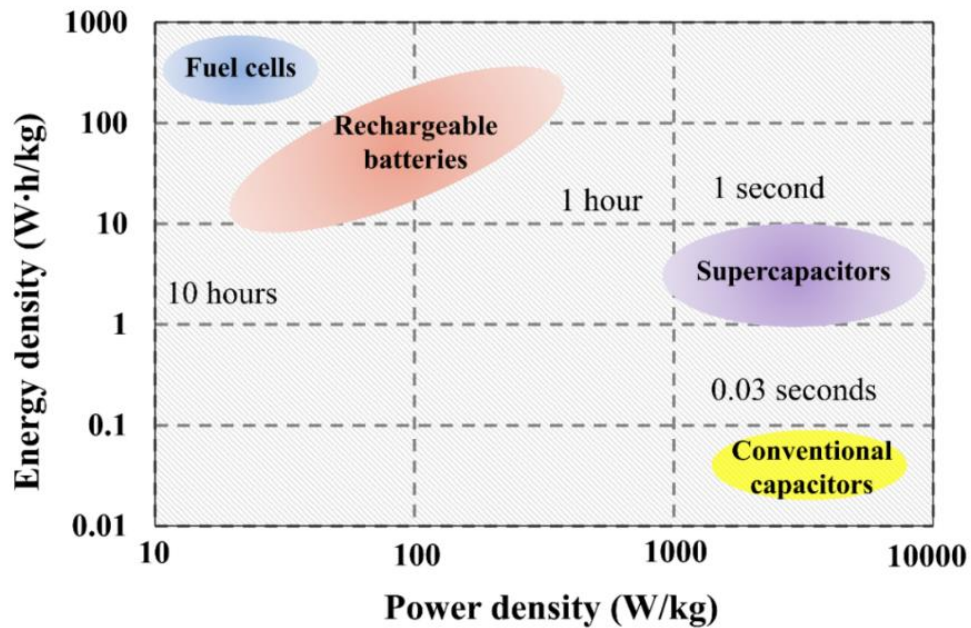


Figure 1.5 Ragone plot showing energy density vs. power density for various devices [23].

#### 1.1.1.3.1 Supercapacitor construction

Like a battery structure, supercapacitor is consisted of two electrode materials (anode and cathode) immersed in an electrolyte. Two electrodes are separated by ion permeable separator, which is located between the electrodes inside supercapacitor construction.

The energy ( $E$ ) and power ( $P_{\max}$ ) of supercapacitors are calculated by [24]:

$$E = \frac{1}{2}CV^2 \quad (1.2)$$

$$P_{\max} = \frac{V^2}{4R} \quad (1.3)$$

where  $C$  is the capacitance (F),  $V$  is the nominal voltage (V), and  $R$  is the equivalent series resistance, ESR ( $\Omega$ ).

Electrode material of supercapacitor can be fabricated from various materials such as porous carbons, conductive polymers, metal

oxides, and hybrid materials, which is depended on what kind of supercapacitor is (details shown in 1.1.1.3.3 Electrode materials for supercapacitor). Apart from electrode, electrolyte is also one of the most important of energy storage components. The requirements for an electrolyte in energy storage device are wide voltage window, high chemical stability, high ionic concentration, low solvated ionic radius, low volatility, low toxicity, high purity, and low cost [25]. Currently, the electrolytes used in an energy storage device can be categorized into three groups: aqueous electrolytes, organic electrolytes, and ionic liquids.

**Aqueous electrolyte:** owing to high ionic concentrations and low resistance properties, aqueous electrolytes such as  $\text{H}_2\text{SO}_4$ ,  $\text{KOH}$ ,  $\text{Na}_2\text{SO}_4$ , and  $\text{NH}_4\text{Cl}$  are widely used as electrolyte in supercapacitor devices. They have been reported that energy storage device containing aqueous electrolyte displays higher capacitance and higher power density than those with organic ones [26-27]. This is because of smaller ionic radius and higher ionic concentration. In addition, aqueous electrolytes are easy to prepare and use without difficult controlling processes and conditions, less safety concern compared to organic electrolytes. Unfortunately, a large weakness of this kind of electrolytes is small voltage window about 1.2 V, which is much lower than those of organic electrolytes. According to equation (1.2) and (1.3), aqueous electrolytes have a great limitation on the improvement of energy and power densities of supercapacitor due to their narrow voltage window (V).

**Organic electrolyte:** comparison to aqueous electrolytes, organic electrolytes can be operated on higher voltage window about 3.5 V. This is a great benefit of organic electrolytes over aqueous ones. They have been reported that acetonitrile and propylene carbonate based electrolytes (PC based) are most commonly used in supercapacitor devices [28, 29]. Acetonitrile has the ability to dissolve larger amounts of salt than other solvents, but it is toxic and non-environmentally friendly substance. However, PC-based electrolytes are non-harmful and eco-friendly compounds. They can offer a wide operating voltage window, a wide operating temperature and good conductivity. Nevertheless, the major problem on organic electrolytes is impurity. The water content in organic electrolytes has to keep

in very low level (less than 3-5 ppm). Otherwise the performance of energy storage devices will be significantly dropped.

**Ionic liquids:** the great benefits of ionic liquids over the others electrolyte systems are high chemical and thermal stability, non-flammability, slight vapor pressure, hydrophobic property, and wide voltage window (from 2 to 6 V) [30-32]. In addition, ionic liquids are solvent-free, so there is no solvation shell in ionic liquids. Consequently, ionic liquids can offer exactly ion size [19]. Their properties make them promising candidates for energy storage electrolytes. Like organic solvent, the chemical-physical properties of ionic liquids also strongly depend on the water content in their compounds [33]. A small amount of water can strongly affect the viscosity, electrochemical stability, and conductivity of this electrolyte. It is very essential to keep the water content in ionic liquids lower than 10-20 ppm, in order to make them efficient for energy storage device [34, 35].

#### 1.1.1.3.2 Type of supercapacitors

Supercapacitors can be classified into three types which are based primarily on their mechanism of energy storage, namely: electrical double layer capacitors (EDLCs), pseudocapacitors, and hybrid capacitors [25].

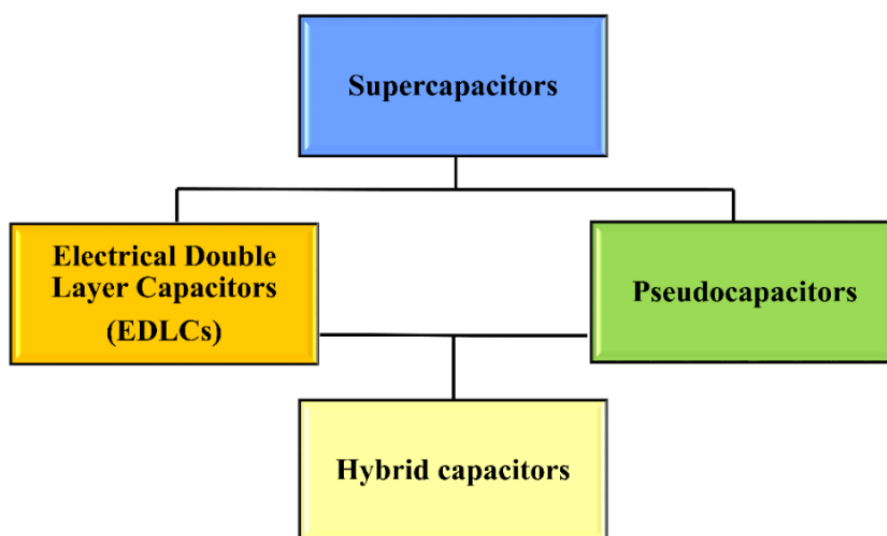


Figure 1.6 Type of supercapacitors [25].

### Electrical double layer capacitors (EDLCs):

basically in each EDLC structure (Figure 1.7), there is no conventional dielectric component instead of an electrolyte (liquid or solid) filled between two electrodes. An electrical condition under applied electric field between the electrodes and electrolyte namely “electrical double layer”, is worked as the dielectric component.

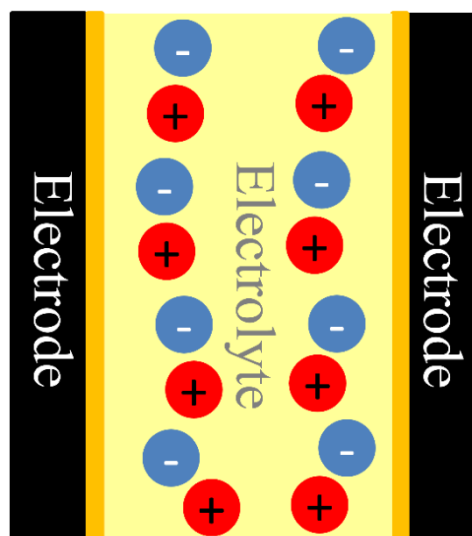


Figure 1.7 Electrical double layer capacitors (EDLCs) structure [21].

The mechanism of storage and release energy of EDLCs is on the basis of charge separation at the interface between an electrode and electrolyte which is not related to redox reactions. EDLCs can store significantly more energy than a conventional capacitor by great number of magnitude because charge separation between an electrode and the adjacent electrolyte in EDLCs has a very small distance (few angstroms) [21]. High charge-discharge behavior of EDLCs is due to essentially rapid movement of ions in and out of electrode surfaces. Hence, the way to increase energy storage of EDLC is the increase in surface area and suitable pore size/structure of electrode materials. Moreover, EDLCs exhibit an excellent life cycle which can be up to 500,000 cycles because storage mechanism of EDLC is not related to redox reaction (no material loss) [16, 36].

For a symmetrical capacitor (similar electrodes, figure 1.7), the cell capacitance ( $C_{\text{cell}}$ ), can be calculated from the following equation [25]:

$$\frac{1}{C_{\text{cell}}} = \frac{1}{C_1} + \frac{1}{C_2} \quad (1.4)$$

where  $C_1$  and  $C_2$  are the capacitance of the first and second electrodes, respectively

The double layer capacitance ( $C_{\text{dl}}$ ) at each electrode interface is calculated by the following relation [25]:

$$C_{\text{dl}} = \frac{\epsilon A}{4\pi t} \quad (1.5)$$

where  $C_{\text{dl}}$  is the double layer capacitance (F),  $\epsilon$  is the dielectric constant of the electrical double-layer region (F/cm),  $A$  is the electrode surface area ( $\text{cm}^2$ ) and  $t$  is the thickness of the electrical double layer (cm).

From equation (1.5), capacitance of supercapacitor electrode is proportional to the surface area of the electrical double layer. The surface area of electrode is enhanced by creating a large number of suitable pores size and structure within electrode material. In general, electrode for this type of supercapacitor is major based on porous carbon materials such as carbon aerogel [37, 38], activated carbon [39], carbon fibers [40, 41], and carbon nanotubes [42, 43].

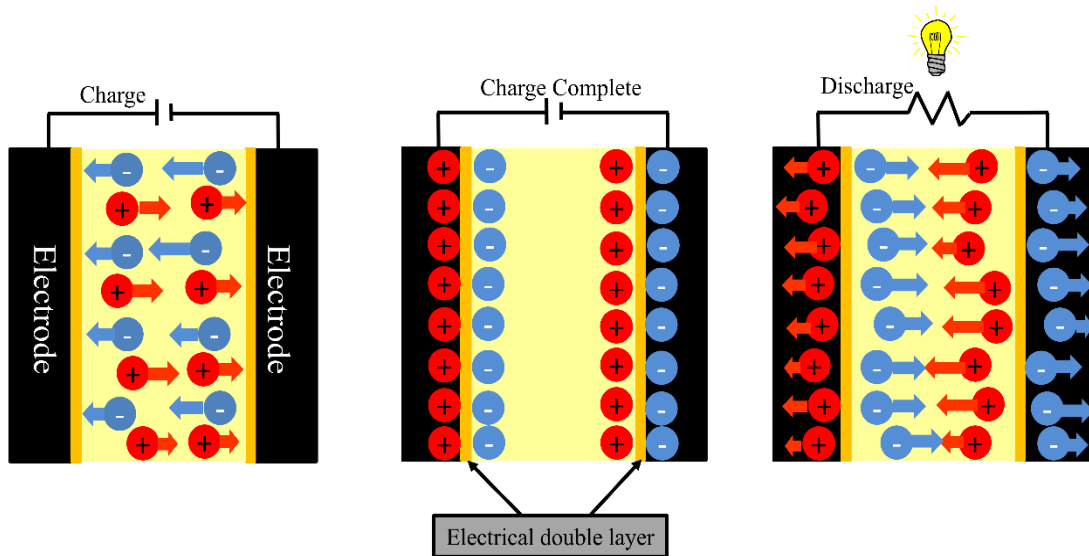


Figure 1.8 Mechanism of energy storage in electrical double layer capacitor [21].

**Pseudocapacitors:** in contrast to EDLCs, this type of supercapacitor can store energy based on faradic redox reactions like rechargeable battery. Consequently, pseudocapacitors usually display higher energy density, shorter cycle life, and lower charge/discharge behavior than EDLCs. Their storage mechanism is involving high energy electrode materials such as transition metal oxides, metal-doped carbons or conductive polymers such as polypyrrole [43], polyaniline [44], or derivatives of polythiophene [24]. In general, metal oxide based electrode has the ability to provide higher energy density than conventional carbon electrodes and better electrochemical stability than polymer materials. When applied with suitable potential voltage windows, electrochemical faradic reactions between electrode materials and ions electrolyte can occur [45]. There are some general requirements for metal oxides in energy storage devices as follows [46]:

- the oxide has a good conductivity behavior.
- the metal has at least two or more oxidation states
- there is no phase change during applied voltage condition.

- protons are able to intercalate into the oxide lattice on reduction state.

Hybrid supercapacitor is the combination of the storing mechanism for both EDLC and pseudocapacitor. It optimizes the power density of EDLC and energy density of pseudocapacitor [25].

#### 1.1.1.3.3 Electrode materials for supercapacitor

Porous carbon materials such as carbon aerogel [37, 38], activated carbon [39], carbon fibers [40, 41], and carbon nanotubes [42, 43] are considered as prospective electrode materials for EDLC. They have been incorporated into the electrodes of EDLC due to abundance, low cost, non-toxicity, easy processing, high chemical stability, high temperature stability, high specific surface area, and good conductivity [47]. The majority of carbon sources are carbon-rich organic precursors such as petroleum pitch, coal pitch, some polymers and biomass. To get porous carbon materials, these carbon precursors are “carbonized” and “activated” in specific conditions (e.g. activation temperature, activation time, and gaseous environment). The final properties of these porous carbons are depended on the properties of carbon precursors, processing conditions and the structural and textural features of the final products [48]. The resulting porous carbon with high specific surface area and suitable pore size structure called “**activated carbon**”.

Activated carbon derived from biomass such as agricultural crops and their residues has been greatly interested in the development of electrode for supercapacitor due to their advantages such as relatively low-cost, abundance and environmental friendliness [49]. Several researchers studied the use of biochar originated from different biomass precursors including paper cardboard and woody biomass as raw material for fabricating supercapacitor [50-53]. The results indicated that biochar is a potential candidate to be used as an electrode because of its low cost and satisfactory performance. For example, the supercapacitor electrodes which are made from biochar derived from woody biomass displayed a potential window of about 1.3 V and fast charge-discharge behavior with a gravimetric capacitance of about 14 F/g [54].

Conducting polymers have been extensively used as electrode materials for pseudocapacitors because of their capacitance behavior through the redox process. In oxidation state, ions move from electrolyte to the polymer backbone and when reduction state, the ions are released from this polymer backbone into the electrolyte. These redox reactions in the conducting polymer go through not only on the surface but also the entire bulk [55]. The charging and discharging reactions do not make any structural or phase change and the processes are highly reversible [56]. Conducting polymers have many advantages that make them suitable for energy storage devices, such as low cost, environmentally friendly system, high storage capacity/porosity/reversibility, high conductivity in a doped state, high voltage window, and adjustable redox activity through chemical modification [44]. The common conductive polymers used in supercapacitor applications are polyaniline (PANI) [44, 57], polypyrrole (PPy) [58], polythiophene (PTh) [59, 60], and etc.

Hybrid electrode materials have been widely used in hybrid supercapacitors due to their ability to enhance power and energy densities as well as superior cycling stability. For example, PTMA-LiFePO<sub>4</sub> [61], CNT-TiO<sub>2</sub> B-nanowire [62], graphene-Fe<sub>2</sub>O<sub>3</sub>/graphene [63], and MWNT- $\alpha$ -Fe<sub>2</sub>O<sub>3</sub>/MWNT [64].

### **1.1.2 Environmental and pollution treatment technology**

According to the rapid growth of economies and population expansion among developing countries, these are the major causes of the wide-range environmental problems (e.g. air, soil, and water pollutions) [65]. For example, mercury and cadmium have been reported as two of the most toxic metals for significant environmental destruction [66]. Moreover, synthetic dyes produced from organic molecules are widely used in textile, paper, and petroleum industrials that strongly affect color wastewater [67]. Concerning to strict regulation on the discharge of wastewater to environment, research and development needed to create sustainable removal in pollutants from wastewater. Various processes and technologies are extensively used for organic and metal removal processes from industrial wastewater such as biological treatments [67-69], membrane processes [70-72], adsorption techniques [73-77], and advanced oxidation processes (photocatalysis) [78-81].

Photocatalysis has gained much attention because it can be applied to various environmental treatment applications such as water purification, air purification, deodorization and etc. (see Figure 1.9).



Figure 1.9 Advantages of photocatalyst [82].

### 1.1.2.1 Mechanism of photocatalysis

This process is related with the acceleration of a reaction when a material (metal oxide and semiconductor) interacts with sufficient energy from light source to produce reactive oxidizing species (e.g. superoxide anions, hydroxyl radical). These reactive species have the ability to transform the organic pollutant into non-toxic substances [82]. Photocatalysis mechanism starts with the absorption of energy from sunlight or any light sources onto the surface of photocatalyst molecule; the excitation of valence electron of photocatalyst. Then the excess energy of this excited electron promotes the electron from the valence band to the conduction band. Consequently, the negative-electron ( $e^-$ ) and positive-hole ( $h^+$ ) pair is created. The energy difference between the valence band and the conduction band is called “band gap energy” (Figure 1.10). The positive-hole of photocatalyst reacts with the water

molecule ( $\text{H}_2\text{O}$ ) to form hydrogen gas ( $\text{H}_2$ ) and hydroxyl radical ( $\text{OH}\cdot$ ) while the negative-electron interacts with oxygen molecule ( $\text{O}_2$ ) to form superoxide anion ( $\cdot\text{O}_2^-$ ). These reactive species have an excellent ability to transform the toxic organic substance into small non-toxic molecules such as carbon dioxide ( $\text{CO}_2$ ) and water ( $\text{H}_2\text{O}$ ), then release to environment [83].

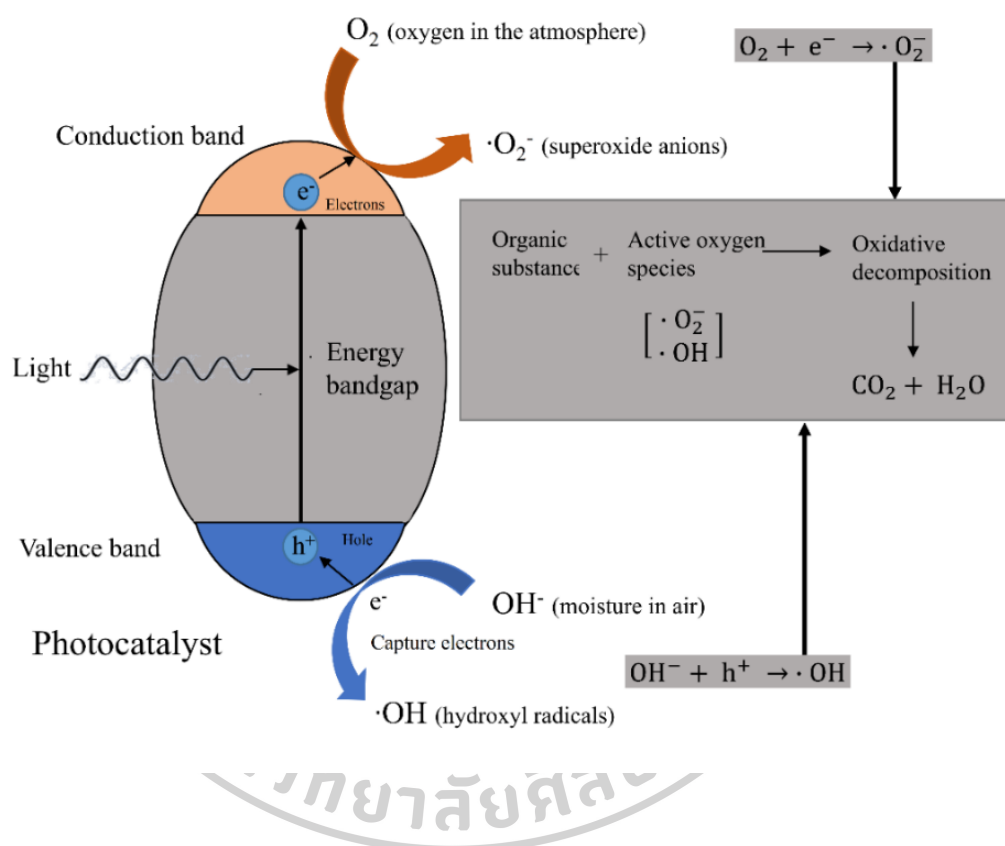


Figure 1.10 Mechanism of photocatalysis process [83].

### 1.1.2.2 Photocatalyst in wastewater application

Since the discovery of photo-electrochemical splitting of water on titanium dioxide ( $\text{TiO}_2$ ) electrodes by Fujishima, A, photocatalytic oxidation (photocatalysis) processes has gained a great attention in the field of wastewater treatment [84].

Titanium dioxide ( $\text{TiO}_2$ ) has been most extensively studied in wastewater treatment application due to its high photocatalytic activity, reasonable

price, photostability, and chemical/biological stability [85-87]. However, TiO<sub>2</sub> also has some disadvantages. Many investigations of TiO<sub>2</sub> have been carried out under UV radiation, since TiO<sub>2</sub> photocatalyst shows relatively high activity and chemical stability under UV light but absorbs only small portion of solar spectrum in UV region because of its large energy band gap around 3.2 eV. Therefore, the photocatalytic properties of TiO<sub>2</sub> under visible light are relatively low.

Zinc oxide (ZnO) has been studied as another efficient photocatalyst for wastewater treatment due to its unique characteristics, such as good photocatalytic property, strong oxidation ability, absorbability in solar wavelength [88-91]. Yeber et al. [92] reported that semiconductors such as nanoparticle TiO<sub>2</sub> and ZnO are the most promising photocatalysts for the degradation of organic dyes in aqueous media in the presence of solar/ultraviolet (UV) illumination. ZnO with different particle sizes and morphologies have been obtained by several preparation approaches including thermal decomposition, vapor chemical deposition, sol-gel method, wet chemical synthesis, mechano-chemical, electro-deposition, gas-phase reaction, and hydrothermal synthesis [93]. Concerning about environmental protection and safety, ZnO has a great attention in photocatalysis because it is an environmentally friendly substance compatible with organisms [94]. These properties make ZnO suitable for the treatment of both water and wastewater.

Hybrid functional materials: regarding to the great developments in nanotechnology, nanoparticle catalysts are playing significant role in photocatalyst. There are many ways to improve the photocatalytic performance of metal oxide nanoparticles. ZnO nanoparticles display the ability to adsorb a wider solar spectra range and more light than several semiconducting metal oxides [95]. However, it is difficult to regenerate metal oxide particles from the treated wastewater, especially when they are suspended in wastewater. One of the most potential approach to address this problem is the development of the bi-functional materials using highly porous carbon materials as catalyst support for embedding metal oxide nanoparticle photocatalyst [96].

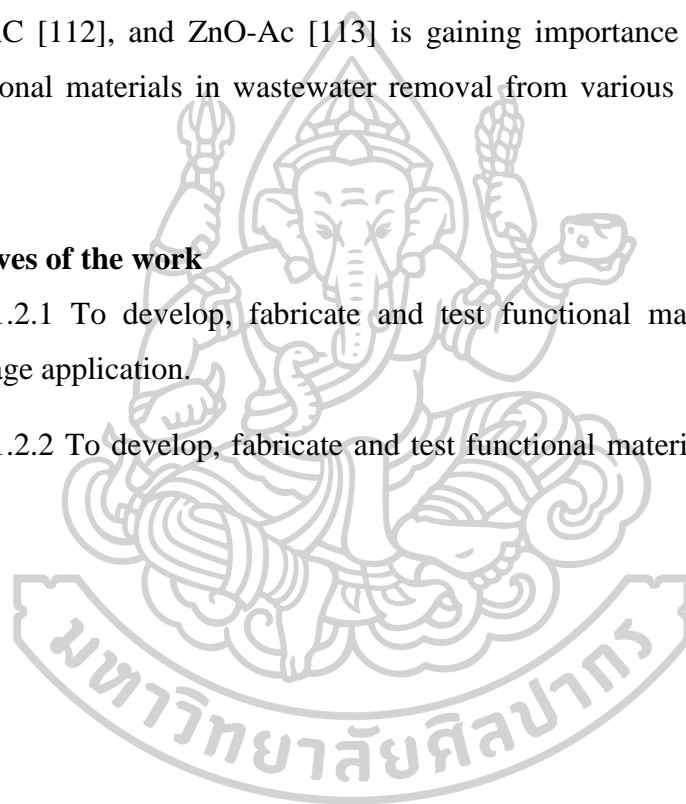
In particular, the use of carbonaceous materials [97-104] (e.g. carbon nanotubes, fullerenes, activated carbon) as catalyst support to enhance the

photocatalytic activity has attracted considerable attention because of their unique and controllable structural and electrical properties [105]. They have been reported that among all the carbon materials, activated carbon and carbon nanotubes have been proven to be an effective adsorbent for the wastewater treatment. They are widely used as adsorbent due to its high surface area ( $\sim 500$  to  $1500 \text{ m}^2/\text{g}$ ), well-controlled and designed pore size/structure as well as the presence of a designed surface functional group [106]. Several researches on development of hybrid metal oxide-activated carbon such as  $\text{TiO}_2\text{-AC}$  [107-109],  $\text{Ag/AgCl-AC}$  [110],  $\text{Co-Ac}$  [111],  $\text{Ba}_2\text{Fe}_2\text{O}_5\text{-AC}$  [112], and  $\text{ZnO-Ac}$  [113] is gaining importance due to the need for these functional materials in wastewater removal from various industry fields [114, 115].

## **1.2 Objectives of the work**

1.2.1 To develop, fabricate and test functional materials for electrical energy storage application.

1.2.2 To develop, fabricate and test functional materials for photocatalyst application.



## Chapter 2

### Literature Review

#### 2.1 Functional materials in energy storage applications

Supercapacitors, which work on the basis of electrostatic double layer capacitance and/or electrochemical reactions (redox reactions), are excellent energy storage systems owing to their high power density, rapid charge/discharge properties, and long life cycle stability [116]. Porous carbon materials such as activated carbons, carbon aerogels, carbon nanotubes, and graphenes are ideal electrode materials for supercapacitors due to their large specific surface area, suitable pore size and structure which allow the electrolyte to access their structure. Typically, commercial activated carbons have the specific surface area ( $S_{\text{BET}}$ ) around 1,500-1,700  $\text{m}^2/\text{g}$ . In addition, high electrical conductive property of carbon electrodes promotes them to be an excellent candidate for supercapacitor electrode [27, 117]. In this work, we focused on activated carbon as electrode materials for supercapacitor application.

##### 2.1.1 Activated carbons from bio-based precursors

Activated carbon electrodes can be fabricated from various lignocellulosic biomass (lignocellulose) precursors (e.g. wood, fruit shells, and bunches) and fossil-fuel based precursors (e.g. petroleum, pitch, and coal). Lignocellulose precursors have been extensively used as electrode materials for supercapacitor applications because they are cheap, abundant, environmentally friendly, and structurally porous comparing to electrode materials from fossil-fuel bases [47]. Theoretically, lignocellulose is composed of three major components; cellulose, hemicellulose, and lignin [118, 119]. Cellulose is a crystalline polysaccharide which contains linear chains of D-glucose monomers  $((\text{C}_6\text{H}_{10}\text{O}_5)_n)$ . Hemicellulose is an amorphous branched polymer which consists of a large number of sugar monomers for example; glucose, xylose, mannose, arabinose, galactose, and rhamnose. Meanwhile, lignin is a highly stable cross-linked polyphenolic aromatic biopolymer, which is made from highly cross-linked phenylpropane units.

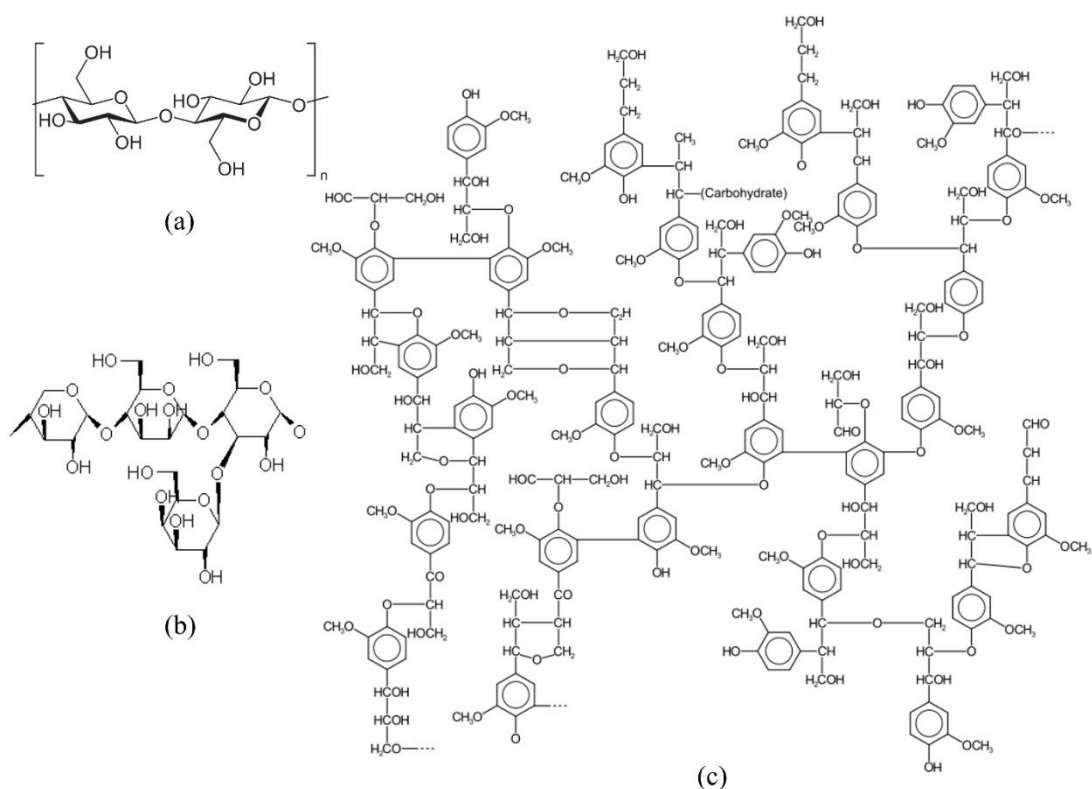


Figure 2.1 Lignocellulosic biomass structure; (a) cellulose, (b) hemicellulose and (c) lignin [119].

These three primary components in lignocellulose form chemical bonding and complex structures related to the ultimate properties of the prepared activated carbon. Agricultural by-product precursors have been used for preparing high-performance electrode for supercapacitor devices. To get porous carbon materials, these carbon precursors are “carbonized” and “activated” in specific conditions (e.g. activation temperature, activation time, and gaseous environment).

### 2.1.1.1 Carbonization process

Carbonization, sometimes called pyrolysis, is a process to produce carbonaceous product (char). During the carbonization, the lignocellulose precursors undergo a thermal treatment; at this stage, moisture and low molecular weight volatiles are first released, followed by light aromatics and finally, hydrogen gas ( $H_2$ ) [120]. During this process, small amount of an initial porosity is produced. The obtained pores, which is produced during carbonization, are blocked by pyrolysis

residues. They really require consequent activation in order to develop the specific characteristics of the porous carbon structure. The carbonization parameters strongly affect the final product (e.g. carbonization temperature, heating rate, residence time, and gas atmosphere). Basically, carbonization temperatures are higher than 600 °C [121]. Higher carbonization temperatures will also increase pore volume and surface area but decrease in yield.

### 2.1.1.2 Activation process

In order to increase pore volume and develop high surface area of porous carbon material; called “activated carbon”. Activated carbon is categorized into three groups depending on its pore size; microporous (< 2 nm), mesoporous (2-50 nm) and macroporous (> 50 nm). Due to their merits of high surface areas (~1 to > 2000 m<sup>2</sup>g<sup>-1</sup>), high conductivity and high chemical and temperature stability along with controlled pore size distributions [54, 122-124], activated carbons have received special recognition for electrode materials of EDLC compared to other carbon forms. The controlled and designed pore size/structure can be achieved by suitable activation conditions of carbon precursors (e.g. activation temperature, activation time and gaseous environment). There are two well-known methods to activate these carbonaceous materials; sometimes called char, commonly known as chemical and physical activation [55, 125, 126].

Physical activation is sometimes referred as thermal activation [127]. This process is related to the heat treatment of the char with steam (H<sub>2</sub>O (g)), carbon dioxide (CO<sub>2</sub> (g)), air, and/or a mixture of these gases, at temperatures between 700 °C and 1100 °C. During the process, the oxidizing atmosphere significantly increases the pore volume and surface area of the carbon material. When increasing burn-off level, a higher degree of activation is achieved, resulting in wider pore structure, lower density, lower yield, and decreased strength of porous carbon structure.

Chemical activation is performed at slightly lower temperatures (~400-700 °C) than physical activation and involves the use of chemical agents such as phosphoric acid (H<sub>3</sub>PO<sub>4</sub>), potassium hydroxide (KOH), and zinc chloride (ZnCl<sub>2</sub>) [127]. The properties of prepared activated carbons depended on the impregnation

ratio (weight of activating reagent/weight of carbon precursor), time of pre-drying and heat treatment conditions (e.g. temperature, soaking time and atmosphere). All these process variables vary with the type of carbon precursors and the activating agents. Generally, chemical activation requires the post-activation process for removal in residual chemical reactants and any impurities from the carbon precursor and/or during activation process.

Daud et al. [128] studied the effects of carbonization temperature on pore development in palm shell based activated carbon. Activated carbon was prepared from palm shell precursor at different carbonization temperatures: 500, 800, and 900 °C followed by physical activation process using the mixture of steam and nitrogen gas at 820 °C. The pore development in palm shell based activated carbon depended strongly on the carbonization temperature. The results showed that activated carbon from high carbonization temperature had a significant amount of micropore volume. The mesopore structure was slightly developed at the initial stage of activation, when increasing of burn-off level, a rapid development in mesopore was observed. The degree of carbon burn-off,  $\theta$  (wt.%), can be calculated as the following relation:

$$\theta = \frac{W_i - W_t}{W_i} \times 100 \quad (2.1)$$

where  $W_i$  is the mass of the sample at the initial of activation and  $W_t$  is the mass of the sample at the end of activation.

Daud and Ali [129] compared the pore development in palm shell and coconut shell based activated carbons. The carbonization and activation processes were conducted at 850 °C using carbon dioxide as activating agent in a fluidized bed reactor. It was reported that the activation rate of coconut shell based activated carbon was almost 5 times higher than the palm based shell activated carbon. This remarkable difference related to lignin contents in palm shell which is higher than coconut one. In addition, the lignin content had affected the number of micropore and mesopore volumes. Consequently, palm shell based activated carbon displayed higher level of micropore and mesopore at every burn-off level. Both activated carbons had

low volume of mesopore because of using carbon dioxide as activating agent, whereas the larger mesopore volume could be achieved when steam was used as the activating agent. The specific surface area of palm shell based activated carbon and coconut shell based activated carbon were  $260 \text{ m}^2/\text{g}$  and  $183 \text{ m}^2/\text{g}$ , respectively.

Adinata et al. [130] also investigated the effect of carbonization temperature and impregnation ratio on palm shell based activated carbon properties using potassium carbonate ( $\text{K}_2\text{CO}_3$ ) as activating agent. The specific surface areas increased with the increase in carbonization temperature from 600 to 800 °C and then slightly decreased when carbonization temperature above 800 °C. The maximum specific surface area of  $1170 \text{ m}^2/\text{g}$  was achieved at carbonization temperature of 800 °C, activation time of 2 h and impregnation ratio of 1.0. The results showed that at low carbonization temperature and impregnation ratio, the pore structure of the activated carbon was mainly consisted of micropores. By increasing the impregnation ratio and carbonization temperature, the increase in mesopore volume relating to the development of micropore to mesopore structures was obtained.

### **2.1.2 Activated carbons as electrode materials for supercapacitors**

Liu et al. [50] studied the effect of nitric acid ( $\text{HNO}_3$ ) on the enhancement of the performance of supercapacitor electrode using poplar wood as precursor and  $\text{HNO}_3$  as activating agent. The obtained electrode displayed maximum specific capacitance of 234 F/g in 2 M KOH solution, at the current density of 5 mA/cm comparing to untreated electrode at 14 F/g. The increase in specific capacitance after surface modification ( $\text{HNO}_3$  treated) is most likely due to the increase in surface functional groups, especially the formation of carboxyl groups and hydroxyl groups on the treated surface. The surface oxygen groups increase the pseudo-capacitance through redox reactions of surface oxygen groups (e.g. C-OH, COOH, C=O, C-NO<sub>2</sub>). The stability tests of both biochar supercapacitor, with and without  $\text{HNO}_3$  treatment, exhibited excellent cyclic stability with a decrease of only 3% performance decays observed after 2000 cycles.

Jiang et al. [131] synthesized a high performance supercapacitor electrode from biochar using red cedar wood as precursor. The biochar was made from one-pot pyrolysis and carbonization of precursor at 750 °C, then biochar was surface modified

by  $\text{HNO}_3$ . The obtained biochar displayed the hierarchically porous structure with high BET specific surface area of 433 and  $317 \text{ m}^2\text{g}^{-1}$  for treated and untreated biochar, respectively. Interestingly, after surface treatment, the specific surface area and pore size of biochar were decreased. This is because the introduction of oxygen groups onto pore surfaces and oxidation-induced pore structure collapse, resulting in the decrease in the specific surface area and pore size, especially the percentage of micropores. Moreover, the presence of oxygen group in treated biochar increased pseudo-capacitance behavior, which was in agreement with Liu's studies [50]. The specific capacitance was increased from 14 F/g (untreated) to 115 F/g (treated) in 0.5 M  $\text{H}_2\text{SO}_4$  solution, at the current density of 0.5 A/g with excellent cyclic stability over 5000 cycles without performance decays.

Jin et al. [132] prepared high performance supercapacitor from activated carbon using corn stover as precursor through microwave and slow pyrolysis process. The results indicated that activated carbon using KOH as activating agent has the highest specific surface area. Meanwhile, the pore structures of the electrode from slow pyrolysis process were not broke down. Besides, the micropores were created during the chemical activation, therefore, tunneling macropore structures could provide the suitable channel for the fast ion transportation during the charge/discharge process, resulting in the high specific capacitance approximately 250 F/g at current density of 0.1 A/g.

Li et al. [133] prepared electrode material from activated carbon for supercapacitor using cationic starch, cassava starch, corn starch, and graft copolymer starch as carbon precursors. The starch precursors were carbonized and activated with KOH at  $850 \text{ }^\circ\text{C}$  for 1.5 h. The obtained activated carbons had specific surface area between  $1,330\text{-}1,510 \text{ m}^2\text{/g}$  and pore size distribution around 1-3 and 5-6 nm. The electrode materials showed the high specific capacitance between 170-200 F/g in 30 wt. % KOH aqueous electrolyte. When the specific current was increased from 370 mA/g to 7.4 A/g, all activated carbons still retained a high initial specific capacitance above 75%. This is related to abundant mesopores allowing electrolyte to transport easily in electrode structure.

Balathanigaimani et al. [134] produced activated carbon from corn grain used as electrode for supercapacitor. The prepared activated carbons had high specific surface area between 2,900-3,500 m<sup>2</sup>/g and pore volume fraction of 55-65% (micropore) and 35-45% (mesopore) with average pore width around 1.1 nm. The highest capacitance of the activated carbon from corn grain precursors was 257 F/g in a 6 M KOH aqueous electrolyte. A non-linear relationship between the specific surface area and the specific capacitance indicated the effect of various pore structural properties and surface functional groups of prepared activated carbon.

Olivares-Marín et al. [29] investigated the performance of activated carbons from recycling cherry stones wastes as electrode material in EDLC. The results showed that KOH-treated activated carbon at 800-900 °C, activation time of 2 h and impregnation ratio of 3.0 had large specific surface areas around 1,100-1,300 m<sup>2</sup>/g, average pore sizes around 0.9-1.3 nm. The highest specific capacitance of prepared electrode was 230 F/g in 2 M H<sub>2</sub>SO<sub>4</sub> electrolyte and 120 F/g in the 1 M (C<sub>2</sub>H<sub>5</sub>)<sub>4</sub>NBF<sub>4</sub> in acetonitrile organic electrolyte, at current density 1 mA/cm.

Li et al. [135] prepared activated carbon as electrode material for EDLC using from sunflower seed shell (SSS) via two different preparation approaches: impregnation-activation and carbonization-activation processes using KOH as chemical activating agent. The results indicated that pore structure and specific surface area of all activated carbons from impregnation-activation depended strongly on activation temperature and dosage of KOH. When increasing activation temperature and dosage of KOH, pore volumes and specific surface areas were increased. Moreover, the development of the mesopores was also depended on the KOH concentration. A high current density of 10 A/g activated carbon was obtained from impregnation-activation process showing better capacitance behavior and higher capacitance retention ratio. This is due to rich mesopores and less interior micropore structure of the activated carbon.

Farma et al. [52] studied the performance of activated carbon from oil palm fibers as electrode materials for EDLC. The oil palm fibers precursors with both untreated and KOH-treated were carbonized at 800 °C and then activated by CO<sub>2</sub> at different activation times from 1-5 h. The results indicated that all the electrodes were

porous carbon materials containing both micropore and mesopore structures with high internal surface area. It clearly showed that using KOH treatment enhanced the specific surface area of the electrodes. The optimum activation time at 3 h resulted in the highest specific surface area of 1704 m<sup>2</sup>/g, specific capacitance of 150 F/g, specific energy of 4.297 Wh/kg and specific power of 173 W/kg.

Mison et al. [136] evaluated electrochemical properties of oil palm kernel shell based activated as electrode material for EDLC. The activated carbons were prepared via physical and chemical activation processes, using KOH as chemical activating agent and steam as physical activating agent. The chemically activated carbon gave a wider pore distribution between 1.4-9.3 nm whereas the physically activated one had uniform pore size at 1.5 nm. The results showed high specific capacitance of 210 F/g in 1 M KOH electrolyte, at current density 0.5 A/g for chemically activated carbon, whereas the specific capacitance of the physically activated carbon was 123 F/g (50% lower). Chemically activated carbon exhibited both micropores and mesopores which assisted the ions movement from mesopores to micropores on the electrode surface and enhanced its electrochemical performance. Meanwhile, physically activated carbon contained only micropores which limited the accessibility of electrolyte to its structure, consequently in lower specific capacitance. Galvanostatic charge-discharge test results revealed the electrodes maintained more than 95% of initial specific capacitance after 1000 cycles, indicating high stability performance of electrode material.

Leng, C. and Sun, K. [28] prepared high performance bio-based activated carbon using coconut shells as a carbon precursor. The activated carbon was produced via chemical-physical combination activation processes using ZnCl<sub>2</sub>, KOH, and steam as activating agents. The activated carbon exhibited a three-dimensional (3D) network pore structure, high specific surface area of 3,242 m<sup>2</sup>/g, unobstructed and interconnected pores and large pore volume. The obtained activated carbon had a high specific capacitance of 337 F/g and retained a specific capacitance of 331 F/g after 10,000 cycles, at current density 0.5 A/g in a 6 M KOH aqueous electrolyte. Moreover, in 1 M (C<sub>2</sub>H<sub>5</sub>)<sub>4</sub>NBF<sub>4</sub> in acetonitrile organic electrolyte, the activated carbon also showed excellent performance with a specific capacitance of 240 F/g.

### 2.1.3 Activated carbon-metal oxide hybrid material as electrode for supercapacitors

Malak-Polaczyk et al. [137] synthesized composites of mesoporous activated carbon with  $\lambda$ -MnO<sub>2</sub>. Two different porous carbons from physical activation and chemical activation were used as supported materials for  $\lambda$ -MnO<sub>2</sub> particles. The results exhibited that porous structure of carbon in the composites played a significant role in electrochemical performance. The through-connected porous structure served as a continuous pathway for electrolyte transport. The electrochemical behavior in 1 M Na<sub>2</sub>SO<sub>4</sub> aqueous solution indicated that electrochemical performance mainly depended on the morphology and the distribution of the MnO<sub>2</sub> particles on mesoporous activated carbon surface.

Wang et al. [138] improved the capacitance of activated carbon (AC) for supercapacitor by incorporating bismuth oxide particle (Bi<sub>2</sub>O<sub>3</sub>) on activated carbon surface to form AC-Bi<sub>2</sub>O<sub>3</sub> composite. The composite material was prepared via mild vacuum impregnation and roasting process. The obtained AC-Bi<sub>2</sub>O<sub>3</sub> electrode material showed a low resistance and a good stability. The specific capacitance of AC-Bi<sub>2</sub>O<sub>3</sub> composite was reported at 332.6 F/g in 6 M KOH electrolyte, at current density of 1 A/g which was higher than that of pure activated carbon of 106.5 F/g (around 3 times larger) at the same testing condition.

Zhao et al. [139] evaluated the electrochemical properties of ordered mesoporous carbon supported cobalt oxide nanoparticles (CoO). The CoC-mesoporous carbon composites were prepared by impregnation process followed by post ammonia treatment. The maximum specific capacitance of 524.8 F/g was achieved from composites loaded with 12.7 wt.% CoO loading, at calcination temperature of 400 °C, in a 6 M KOH electrolyte. The CoC nanoparticles were playing an important role in faradic charge transfer reactions between the cobalt oxides particles and the electrolyte. The clear two redox peaks in CV curve of this composite were observed within the potential range of -0.4 to 0.4 V, suggesting strong pseudo-capacitance behavior from this composite electrode material.

Mondal et al. [140] reported two-step synthesis of macroporous carbon/TiO<sub>2</sub>/MnO<sub>2</sub> nanocomposites thin films via spin coating technique followed by carbonization process. The maximum specific capacitance of 297 F/g was achieved in 1 M Na<sub>2</sub>SO<sub>4</sub> aqueous electrolyte, at 5 mV/s, which was almost 7 times higher than that of pure porous carbon. This result indicated that the incorporation of nanoparticle enhanced the specific capacitance via pseudo-capacitance behavior of the prepared composite.

Zhang, X. et al. [141] established a novel method for preparation of binder-free carbon-metal oxide composite electrode. Firstly, 2D-layered Ni-Co mixed metal-organic frameworks (MOFs) were deposited directly on nickel foam by anodic electro-deposition followed by pyrolysis and activation process. The electrochemical performance of the prepared electrode was evaluated in 4 M KOH aqueous electrolyte, at room temperature condition. The results exhibited a superior rate performance of 93% in the current density range from 1 to 20 mA/cm and high specific capacitance of 2,098 mF/cm, at current density 1 mA/cm. The supercapacitor also exhibited a specific energy density of 36.4 Wh/kg and a specific power density of 90 W/kg. After 10,000 cycles, there was no obvious capacitance fading, indicating excellent charge-discharge cycling stability.

#### **2.1.4 Carbon nanotube as electrode for supercapacitors**

Carbon nanotube is one of the most carbon based material which has been extensively studied for electrode materials for supercapacitors, with specific capacitances ranging from 4 to 180 F/g in H<sub>2</sub>SO<sub>4</sub> or KOH aqueous solution [142-146]. The specific surface area and the pore size of the carbon nanotubes remarkably affect the specific capacitance of capacitor [147].

Niu et al. [144] prepared carbon nanotube sheet electrodes from catalytically grown carbon nanotubes. This process can be divided into 3 steps: first, disassembling of such nanotube aggregates and introduction of chemical functional groups on the surface of the nanotubes; second, dispersion of the functionalized hydrophilic nanotubes in water; and third, reassembling of the individualized carbon nanotubes into an interconnected, entangled, and free-standing structure followed by

HNO<sub>3</sub> acid treatment. The carbon nanotube sheet electrodes with specific surface area of 430 m<sup>2</sup>/g showed a specific capacitance on a single cell device at 113 F/g in 38 wt.% H<sub>2</sub>SO<sub>4</sub> aqueous electrolyte.

Zhang et al. [148] studied the performance of porous tablets of carbon nanotubes electrodes in EDLC. Carbon nanotubes were synthesized by a process catalytic pyrolysis using the mixture of acetylene (C<sub>2</sub>H<sub>2</sub>) and Hydrogen (H<sub>2</sub>) as precursors and nickel particles (Ni) as catalyst followed by HNO<sub>3</sub> acid treatment for removal of the excess Ni particles. As-synthesized carbon nanotube electrode had specific surface area of 100 m<sup>2</sup>/g and specific pore volume of 0.21 cm<sup>3</sup>/g which mainly consisted of mesopore and macropore structures. The electrochemical performance of electrode showed the specific capacitance of 16.6 F/cm<sup>3</sup> using LiClO<sub>4</sub> in a mixture of ethylene carbonate and propylene carbonate (1:1) as the organic electrolyte. Moreover, the energy density of this electrode was reported at 20 Wh/kg on a single cell device with a 10 mA discharge current.

Yoon et al. [149] prepared integrated carbon nanotube electrodes for EDLC. Carbon nanotube was directly synthesized on the bulk Ni substrates by the plasma enhanced chemical vapor deposition of CH<sub>4</sub> and H<sub>2</sub>. The synthesis process was performed without additional catalyst. By applying ammonia plasma treatment, the specific surface area was increased from 9.63 m<sup>2</sup>/g to 86.52 m<sup>2</sup>/g and the specific capacitance also was increased from 38.7 F/g to 207.3 F/g. This remarkable enhancement was due to the increase in total surface area and surface functional groups of the prepared electrode.

Li et al. [150] fabricated carbon nanotubes (CNT) from the mixture of C<sub>3</sub>H<sub>6</sub> : H<sub>2</sub> (2:1), at 750 °C using Ni as catalyst followed by acid treatment process. The results of the electrochemical experiment showed the increase in the capacitance of activated carbon nanotubes electrode. The CNT which was activated by acid mixture (H<sub>2</sub>SO<sub>4</sub> and HNO<sub>3</sub> of 3:1) had the higher BET specific surface area and pore volume comparing to CNT activated by pure acid. The specific surface area, pore volume and specific capacitance of CNT activated by acid mixture were 1.6, 1.4, and 2.5 higher than those of the initial CNT, respectively. The results indicated that the acid mixture had the best effect for CNT activation.

Xu et al. [151] evaluated the electrochemical performances of carbon nanotubes (CNT) as the electrodes in EDLC using novel binary room temperature molten salt (RTMS), lithium bis(trifluoromethane sulfone)imide ( $\text{LiN}(\text{SO}_2\text{CF}_3)_2$ , LiTFSI) and acetamide as electrolyte. This electrolyte exhibited excellent thermal stability, high ionic conductivity, and wide electrochemical stability window on carbon nanotubes electrode. The results indicated that EDLC with RTMS electrolyte could be charged up to 2.5 V with good rate performance and high capacitance retention. The specific capacitance based on carbon nanotubes reached 22 F/g and 30 F/g at 20 °C and 60 °C, respectively.

### **2.1.5 Carbon nanotube-metal oxide hybrid materials as electrode for supercapacitors**

Ye et al. [152] prepared ruthenium oxide ( $\text{RuO}_2$ ) modified multi-walled carbon nanotube (MWNT) nanocomposite electrode ( $\text{RuO}_2/\text{MWNT}$ ) for electrochemical supercapacitors. MWCT/ $\text{RuO}_2$  nanocomposite was prepared by chemical vapor deposition (CVD) method followed by magnetic-sputtering technique for deposition ruthenium particle (Ru) on MWNT surface. The results showed that the specific capacitance of the MWNT electrode in 1 M  $\text{H}_2\text{SO}_4$  aqueous electrolyte was significantly increased from 0.35 to 16.94  $\text{mF}/\text{cm}^2$ . This is due to the incorporation of  $\text{RuO}_2$  particles resulting in the enhancement of the pseudocapacitance behavior of composite electrode. It has been reported that this process could be implemented for the large scale fabrication of high-volume supercapacitor with modified MWNT on large-flat metal electrode materials.

Reddy and Ramaprabhu [153] synthesized the  $\text{RuO}_2/\text{MWNT}$ ,  $\text{TiO}_2/\text{MWNT}$ , and  $\text{SnO}_2/\text{MWNT}$  nanocrystalline composites electrodes. Firstly, MWNT was prepared by thermal CVD facilitated by catalytic decomposition of acetylene ( $\text{C}_2\text{H}_2$ ). After purification process of MWNT, each nanocrystalline metal oxide particles;  $\text{RuO}_2$ ,  $\text{TiO}_2$ , and  $\text{SnO}_2$  was deposited on the MWNT surface by chemical reduction method. The functionalized MWNT electrodes had a specific capacitance around 67 F/g. The nanocrystalline  $\text{RuO}_2/\text{MWNT}$ ,  $\text{TiO}_2/\text{MWNT}$ , and  $\text{SnO}_2/\text{MWNT}$  composite electrodes had a specific capacitance of 138, 160, and 93 F/g, respectively. The enhancement of the specific capacitance of metal oxide

dispersed MWNT from pure MWNT was due to the progressive redox reaction of the modification of surface morphology of MWNT by the RuO<sub>2</sub>, TiO<sub>2</sub>, and SnO<sub>2</sub> nanoparticles, respectively.

Zhang et al. [154] prepared electrode composite of vertically manganese oxide nanoparticles on carbon nanotube array (CNTA) surface for electrochemical supercapacitors. The nanocomposite was prepared by combination technique between electro-deposition and a vertically aligned CNTA framework. The obtained composite had hierarchical porous structure, large surface area, and superior conductivity with controllable structure and properties. The electrochemical performance of this electrode indicated the excellent rate capability with 50.8% capacity retention at 77 A/g, high specific capacitance of 199 F/g, and high stability with only 3% capacity loss after 20,000 charge/discharge cycles.

Sellers et al. [155] synthesized 3D manganese dioxide-functionalized multi-walled carbon nanotube electrodes composite (MnO<sub>2</sub>-MWNT) by thermal decomposition process. The electrodes were prepared by treating planar MWNT sheets with manganese nitrate (Mn(NO<sub>3</sub>)<sub>2</sub>) solution and annealing at low temperature between 200-300 °C, at ambient pressure. The specific capacitance of composite electrode was 14 times higher than that of pure MWNT electrode. The specific capacitance varied linearly with Mn(NO<sub>3</sub>)<sub>2</sub> thermal decomposition temperature from 100, 80, and 61 F/g at current density 0.2 A/g, at the 200, 250, and 300 °C, respectively. The supercapacitor which was fabricated at 300 °C thermal decomposition temperature exhibited the best retention characteristics, with capacity decaying around 30% after 1,000 charge/discharge cycles at 1 mA.

Su and Zhitomirsky [156] prepared the electrode material for hybrid supercapacitor using vanadium nitride nanoparticles (VN) and multi-walled carbon nanotube (MWNT) by a chemical method. The results showed good capacitive behavior in 0.5 M Na<sub>2</sub>SO<sub>4</sub> electrolyte and the specific capacitance of VN-MWNT composite electrode were significantly higher than those of pure VN and MWNT materials due to synergy effect. The VN-MWNT electrodes with high mass loading in the range of 10-30 mg/cm<sup>2</sup> showed high specific capacitance, good capacitance retention, and good cycling stability. The highest capacitance of 160 F/g was achieved

at 2 mV/s. Good electrochemical performances of the VN-MWNT composite electrodes in the negative potential range in the 0.5 M Na<sub>2</sub>SO<sub>4</sub> electrolyte allowed the fabrication of new type of hybrid cells, containing VN-MWNT as negative electrode and MnO<sub>2</sub>-MWNT as positive electrode. The hybrid cells showed promising electrochemical performance in a voltage window of 1.8 V in aqueous 0.5 M Na<sub>2</sub>SO<sub>4</sub> electrolyte with energy density of 38.7 Wh/kg and a power density of 7.3 W/kg.

Zhang et al. [157] reported a one-pot synthesis method of Mn(MnO)/Mn<sub>5</sub>C<sub>2</sub>/CNT composite electrode for electrochemical supercapacitors. The capacitive properties of the prepared electrodes were investigated by a cyclic voltammetry (CV) test in a 0.5 M Na<sub>2</sub>SO<sub>4</sub> aqueous solution. The electrode which was prepared at 600 °C for 1 h displayed a maximum specific capacitance of 378.9 F/g, at 2 mV/s. There was a slightly decrease in the specific capacitance even after 1000 cycles, indicating an excellent cycling stability of the prepared composite electrode.

Kao et al. [158] prepared composite electrode of titanium nitride (TiN) coated on carbon nanotube (CNT) for electrochemical supercapacitors by means of atomic layer deposition (ALD) technique. The resulting electrode showed a great performance and its specific capacitance was 400 times higher than that of a flat-shape electrode. The electrochemical capacitance of TiN/CNT composite electrodes was 81 mF/cm<sup>2</sup> which was higher than that of electrode without TiN at 14 mF/cm<sup>2</sup>. This was due to the increase in oxygen vacancies on the TiN surfaces.

### **2.1.6 Ceramic-polymer composites as dielectric material in energy application**

Ceramic ferroelectric oxides, which exhibit a spontaneous electric polarization that can be reoriented with an external field, have received considerable attention because of their utilization in nonvolatile memory devices [159-163]. These oxides also exhibit other related properties, including piezoelectricity, pyroelectricity and large dielectric constants which have been applied in fabricating microactuator, sensor and capacitor applications [159-161].

Recently, there have great efforts to develop complex shape dielectric materials that have high dielectric constant, low dielectric loss and good processing

properties [164-165]. One of the most promising approach is to develop ceramic-polymer nanocomposites, by adding small amount of nanostructure ferroelectric ceramic into polymers matrix can be greatly improved electrical and dielectric properties of the host polymers because of its high surface to volume ratio [164]. Ceramic-polymer nanocomposites with excellent dielectric property have attracted great attentions in energy and electrical devices due to their various potential applications, such as capacitors, actuators and printed circuit boards [165-167].

Poly(vinylidene fluoride) (PVDF) has been studied extensively for its outstanding pyroelectric and piezoelectric properties [165-168]. It is well-known for its manifold characters with four different crystalline forms:  $\alpha$ ,  $\beta$ ,  $\gamma$  and  $\delta$ . These crystalline phases could be transformed into each other under specific conditions. Among these phases, the  $\beta$ -PVDF reveals good pyroelectric, piezoelectric and dielectric properties. Generally,  $\beta$ -phase PVDF is obtained by high electric field polarization, high pressure crystallization and uniaxial stretching. Over the past decade, the electroactive poly(vinylidene fluoride) (PVDF) has been studied in dielectric materials field. It has several advantages over traditional ceramic ferroelectric materials in term of high mechanical strength, good flexibility, excellent chemical stability, non-toxic material and easy process as complex shape at low temperature [164-168]. Barium titanate ( $\text{BaTiO}_3$ : BT) is lead-free ferroelectric ceramic materials with a perovskite structure which is utilized in large areas of application due to its attractive piezoelectric and dielectric properties [169-171]. It has been used in large areas of applications such as in tunable capacitors, pyroelectric sensors, nonvolatile memories and surface acoustic wave devices [169, 170].

Mathews et al. [162] reported the dielectric and functional properties of three-phase composite poly(vinylidene fluoride)/zinc oxide/barium titanate (PVDF/ZnO/BT). The results showed that dielectric constant and dielectric loss of this composite increased with increasing ceramic content and dropped rapidly with increasing frequency.

Park et al. [163] studied dielectric properties of PVDF/BT particles composite. BT particles were prepared by molten salt method with different particle sizes. The results revealed that BT particle size had great effect on dielectric

properties of composite. The composite with 600 nm particle size of BT exhibited the strong polarization. The result showed that dielectric constant of the composites with 40% vol of BT loading was 65 at 25 °C, 1 kHz.

Hajeesaeh and Muensit [170] fabricated PVDF/BT sheet composite by tape casting method. It was found to be that the density and heat capacity of the composites were 3.21 kg/m<sup>3</sup> and 3021.7 J/kg °C, respectively. The prepared composite was poled before dielectric test. The results of dielectric properties exhibited that dielectric constant and dielectric loss were 11.5 and 0.21 at a frequency of 1 kHz and room temperature condition, respectively.

Upadhyay and Deshmukh [171] prepared PMMA/BT composite via solution casting method. The results indicated that dielectric constant of nanocomposites was strongly depended on frequency, temperature and content of ceramic filler. Dielectric loss was also influenced by the frequency and the temperature but was not much influenced by the content of ceramic filler. The nanocomposite with 10 wt. % of BT loading exhibited the lowest dielectric constant of 3.58 and dielectric loss of 0.024 at 1 MHz and 25 °C, suggesting that PMMA/BT composite was suitable in microelectronics devices.

Li et al. [172] studied dielectric properties of binary PVDF/BT nanocomposites and ternary nanographite (GN) doped PVDF/BT hybrids materials. The nanocomposites were fabricated using a simple solution casting process followed by compression molding. The dielectric constant at 1 kHz of the PVDF/BT/GN 80/20/2.5 hybrid was 50 which was four times higher than that of the PVDF/BT 80/20 nanocomposite. The results indicated that incorporating low content of graphite nanosheets to the binary composite system had significantly affected dielectric constant, especially at the percolation threshold. They found that both dielectric constant and electrical conductivity of hybrids materials were strongly depended on frequency and temperature.

Upadhyay and Deshmukh [164] investigated dielectric properties of  $\beta$ -PVDF/BT nanocomposite films. Nanocomposite film was prepared by solution casting method. The dielectric constant and dielectric loss were evaluated in the

frequency range of 100 Hz to 10 MHz at biasing voltage of 1 V and temperature from 25 °C to 120 °C. The results showed exponential increase in the dielectric constant with increasing temperature. This was due to the greater movement freedom for the dipole molecular chain of polymer at high temperature. The highest dielectric constant of 8.70 was achieved from composite with 1 wt. % of BT filler at 1 kHz and 25 °C which was higher than that of neat PVDF around 33% at the same testing condition.

Yang et al. [173] studied dielectric properties of PVDF/BT-PANI composite. The composite was prepared by blending PVDF with polyaniline (PANI) coated nano-sized barium titanate (BT) to form PVDF/BT-PANI composite. The results showed that incorporation of conductive PANI to the ceramic-polymer systems had significantly influenced the dielectric properties of PVDF/BT-PANI composite. The prepared composite had higher dielectric constant than PVDF/BT composite in the frequency range from 40 Hz to 1 MHz.

Wang et al. [174] improved the dielectric properties of PVDF/Ag film composite. PVDF/Ag film composites were prepared by solvent casting method. They found that with increasing nano Ag content, the dielectric constants of the composites were first increased and then decreased, whereas the dielectric losses were first decreased first and then increased. The highest dielectric constant of composite film of 14.5 at 100 Hz was achieved from 17% vol. Ag composite with lower dielectric loss and the energy storage density was relatively high at  $0.340 \text{ J cm}^{-3}$ .

Luo et al. [175] fabricated calcium barium zirconate titanate (BCZT)/PVDF composite flexible films via a solution casting method. The results showed that dielectric constant increased with the increase in BCZT contents, while the dielectric loss remained constant in the frequency range of 10 kHz to 0.1 MHz.

Bunnak et al. [176] studied an increase in dielectric constant of binary composite based on PVDF/clay system. The composite film with 10 wt. % of barium doped porous clay in PVDF matrix was fabricated by mechanical mixing (Brabender) and hot pressing methods. The dielectric properties of the composite film strongly depended on frequency and temperature. They found that dielectric constant was suddenly decreased with the decrease in temperature until below the glass transition

temperature of PVDF. The relaxation behaviors indicated that the dielectric behaviors in these composite films were highly dominated by polarization process.

Cho et al. [177] enhanced the energy harvesting performance and dielectric constants of PVDF by incorporating surface-treated BT in PVDF matrix. The surface-treated BT influenced the crystallinity of the PVDF. The dielectric constants of nanocomposites increased after addition of the surface-treated BT up to 16 wt.% and the dielectric loss also decreased with increasing amounts of surface-treated BT. This indicated that the surface-treated BT particles disrupted the movements of the molecular chains of PVDF, which resulted in the decrease in the dipole loss. The results showed that the highest dielectric constant of composite was 110 compared to pristine PVDF having dielectric constant around 12 at 1 kHz, 25 °C.

Zhang et al. [178] improved dielectric and electrical properties in PVDF/SiC/BT three-phase composite through microstructure tailoring. The results showed that the three-phase composite exhibited low dielectric loss and high dielectric constant. It was also found that the nano-size BT was more favorable in achieving high dielectric constant than the micro-size BT, while their dielectric loss and electrical conductivity were similar.

Recently, Castles et al. [179] prepared BT powder/ABS dielectric composites by 3D printing technique. They reported on the fabrication of a series of composites composed of various loadings of BT microparticles in the ABS matrix. The dielectric properties of printed parts at 15 GHz had dielectric constant in the range of 2.6-8.7 and dielectric loss in the range of 0.005-0.027. Dielectric properties were reproducible over the entire process, and matched those of bulk unprinted materials, to within ~1%, suggesting that this technique could be used for industrial process of dielectric composites.

## **2.2 Functional materials in photocatalyst applications**

Photocatalysis has been recognized as a potential technique for degradation process, which is being widely used as one of the most effective method for wastewater treatment. Recently, the development of photocatalyst with high

efficiency and recovery is still a challenging task in the field of wastewater treatment [180].

### **2.2.1 Activated carbon as catalyst supported for photocatalyst in wastewater application**

Zhang et al. [181] prepared photocatalyst of anatase TiO<sub>2</sub> particles coated on activated carbon by atmospheric pressure metal organic chemical vapor deposition (AP-MOCVD). The optimum TiO<sub>2</sub> loading was 12 wt.% and the photocatalytic activity of the TiO<sub>2</sub>/activated carbon was close to that of commercial TiO<sub>2</sub> nanoparticle (Degussa P25). The result exhibited the ability to separate the TiO<sub>2</sub>/activated carbon catalyst from the treated water. The cycle testing showed that the catalytic performance was able to maintain even after 10 cycles, indicating the stability of TiO<sub>2</sub> coating on activated carbon surface.

Ao et al. [182, 183] studied the photocatalytic activity of anatase TiO<sub>2</sub>-activated carbon composite film; AC-TiO<sub>2</sub>. They prepared anatase TiO<sub>2</sub> by sol-gel technique followed by the mixing of activated carbon and the synthesized TiO<sub>2</sub> sol to form slurry. The composite film was prepared by dipping-withdrawing method using glass slide as substrate. The photocatalytic activity of the composite film was determined by degradation of 4-chlorophenol (4-CP) under UV irradiation. The AC-TiO<sub>2</sub> composites showed the enhancement in photocatalytic activity over TiO<sub>2</sub> alone due to the porosity of the AC providing high adsorption capacity and high concentration of 4-CP around TiO<sub>2</sub> particles. The recycle ability of the composite film was also investigated. The degradation ratio was still higher than 85 % after 5 cycles, which the photocatalytic activity decreased only 3% compared to the first cycle, suggesting the good stability of AC-TiO<sub>2</sub> composites on wastewater treatment application.

Byrappa et al. [184] evaluated the photocatalytic performance of zinc oxide-activated carbon (ZnO-AC) composite for degradation of acid violet dye. The results exhibited that the composite had higher photocatalytic activity comparing to the commercial ZnO and untreated activated carbon. The ZnO-AC composite had a very effective in the degradation of acid violet dye because the synergism effect between the ZnO photocatalyst and activated carbon was clearly verified.

Sobana et al. [185] evaluated photocatalytic activity of activated carbon-zinc oxide; AC-ZnO catalyst. The photocatalytic activity was determined by the degradation of 4-acetylphenol. The optimum loading content of ZnO on AC surface was found to be at 9 wt.%, while ZnO particles displayed homogeneous distribution at this optimum loading level. Under UV-irradiation, ZnO showed a 100% removal of 4-acetylphenol in 240 min, whereas ZnO composite at 9 wt.% degraded completely in 150 min. This composite was found to be more efficient in solar light than in UV light. The enhancement of this photocatalytic efficiency was due to the synergistic effect between ZnO and activated carbon with synergy factor at 2.0.

Gondal et al. [180] synthesized magnetic separable AC/TiO<sub>2</sub>/Ni composites by a facile pyrolysis reaction and studied their photocatalytic performance for removal of a methyl orange (MO) dye from water under UV light irradiation. The results proved that the synthesized photocatalyst (AC/TiO<sub>2</sub>/Ni) exhibited significant enhancement in the photocatalytic activity for removal of MO dye from wastewater comparing to the commercial TiO<sub>2</sub> (P25). The results of electrochemical impedance measurements confirmed the synergetic effect on the interface of TiO<sub>2</sub> and AC. It could promote the photo-induced electron mobility in the surface of TiO<sub>2</sub> and the absorption of AC particles leading to the high concentration of MO around TiO<sub>2</sub> particles.

Sobana et al. [186] studied the synergism effect of AC/ZnO photocatalyst on degradation of azo dye (DY4). The photocatalytic activity showed that AC/ZnO displayed more efficient than commercial ZnO for degradation of DY4. The higher efficiency of AC/ZnO was due to its synergetic effect with the synergistic factor at 2.0. The optimum pH and the catalyst concentration for dye removal were found to be at 9 and 5 g L<sup>-1</sup>, respectively. It was reported that the degradation rate was decreased as initial dye concentration was increased.

Andriantsiferana et al. [187] investigated photocatalytic degradation of tartrazine in aqueous solution using AC/TiO<sub>2</sub> as catalyst. TiO<sub>2</sub> particles were deposited on AC surface by MOCVD technique in a fluidized bed under atmospheric pressure. The photocatalyst TiO<sub>2</sub>/AC revealed photocatalytic activity for the degradation of tartrazine. The results of cyclic use indicated that the degradation of

tartrazine was up to 80% from the first three cycle and it was downed to less than 50% in the fourth cycle. The best performances of AC/TiO<sub>2</sub> were explained by a rapid transfer of the organic compounds from adsorption sites to photocatalytic sites.

Nasrollahpour and Moradi [188] studied photochemical degradation of methylene blue (MB) using iron oxide-modified activated carbon (Fe<sub>2</sub>O<sub>3</sub>/AC) as catalyst. Microporous activated carbon was prepared from microwave assisted technique using grapevine rhytidome (agricultural waste) as precursor and H<sub>3</sub>PO<sub>4</sub> as chemical activating agent. Then, Fe<sub>2</sub>O<sub>3</sub> particle was deposited on activated carbon surface by microwave assisted technique. The results of photocatalytic activities indicated that the degradation of MB followed first-order kinetics equation, with the optimal conditions for the degradation of MB dye at 75 min, 100 ppm dye concentration, neutral pH and 0.13 mg/L of catalyst concentration.

Thi and Lee [189] synthesized photocatalyst using activated carbon fiber as supported material for ZnO rod via facile microwave method. The photocatalytic activity was evaluated by degradation of tetracycline. At pH 8, ZnO rod-ACF photocatalyst displayed excellent removal capacity (over 99%) and mineralization (90.7%) of tetracycline in aqueous solution within 1 h under UV irradiation. The stability and the mineralization of tetracycline of ZnO rod-ACF composite were maintained above 80% after multiple usage cycles. These results were attributed to the enhancement adsorption ability of ZnO in combination with ACF and formation of hydroxyl ( $\bullet$ OH) and superoxide radicals ( $\bullet$ O<sub>2</sub>) which could break the tetracycline molecule by oxidative decomposition reaction.

### Chapter 3

## Coconut Shell Based Activated Carbon and Coconut Shell Based Activated Carbon-TiO<sub>2</sub> Composite Catalysts for Energy Storage and Photocatalyst Applications

### 3.1 Abstract

Coconut shell, a food solid waste, was successfully utilized as a low cost alternative adsorbent for the electrode in supercapacitor device and the removal of textile dye (methylene blue). Coconut shell based activated carbon (ACCS) and coconut shell based activated carbon-metal oxide hybrid (ACCS/TiO<sub>2</sub>) catalysts were prepared and their performance was tested for supercapacitor and photocatalyst applications. The ACCS powders were prepared by a chemical activation method and the TiO<sub>2</sub> powders were synthesized by a solvothermal process. The prepared products were characterized by scanning electron microscopy (SEM), transmission electron microscopy (TEM), N<sub>2</sub> adsorption-desorption measurement, Raman spectroscopy, and X-ray diffraction (XRD) techniques. The result clarified that activated carbon material with high specific surface area and high porosity was synthesized by KOH activation process from coconut shells at 800 °C and impregnation ratio of 3:1. The electrochemical behaviors of the samples were tested using cyclic voltammetry (CV) and galvanostatic charge-discharge in a symmetrical two-electrode cell. The ACCS sample provided the highest specific capacitance value of 149.65 F/g at the current density of 0.5 A/g and the highest energy density of 4.64 Wh/kg at the power density of 239.66 W/kg. Moreover, activated carbon modified TiO<sub>2</sub> hybrid photocatalysts have drawn increasing attention because of their high performance. TiO<sub>2</sub>/activated carbon hybrid films were fabricated on aluminum substrates by electrophoretic deposition. Pristine TiO<sub>2</sub> powder was synthesized by solvothermal process. Methylene blue was used as model organic compound for evaluation of the photocatalytic efficiency and reusability of the as-prepared photocatalysts under ultraviolet light irradiation. The color removal efficiency of TiO<sub>2</sub>/activated carbon hybrid film obtained using the synthesized TiO<sub>2</sub> was found to be 97%. The hybrid film system has an advantage for wastewater treatment in practical applications

because it is easy to separate from the process, cost-effective, eco-friendly, and reusable with relatively high photocatalytic efficiency.

### 3.2 Introduction

Highly porous activated carbon can be prepared from agricultural by-product precursors such as palm shell [1-3], coconut shell [2, 4, 5], almond shell [6], and peanut shell [7]. To get highly porous activated carbon materials, these carbon precursors are “carbonized” and “activated” in specific conditions (e.g. impregnation ratio, activation temperature, activation time, and gaseous environment). Activated carbon can be prepared either by physical or chemical activation methods. The activation process results in an increase in pore of activated carbon [8-10]. Highly porous activated carbon has been used in a wide variety of applications, such as adsorbent materials in separation or purification of liquid and gases [11, 12], electrode materials for energy storage devices [13-15], and catalyst supports [16-19].

Supercapacitor is an energy storage device that can store and discharge electricity. The supercapacitors are mainly divided into two types based on their electrochemical behaviors: electrochemical double layer capacitors (EDLCs) and pseudo-capacitor or redox supercapacitor. EDLCs have attracted great interest due to their short response time, outstanding power density, long cyclic stability, and increased energy storage owing to the effect of double capacitor layer [20]. The carbon materials, including carbon nanotubes [21], graphene [22], carbon nanofibers, [23] and activated carbons [13-15, 24], are the most widely used materials as electrodes for EDLC devices owing to their high surface area, excellent chemical and corrosion resistance, high thermal stability, and superior electrical conductivity. Among the carbon materials, activated carbons (ACs) are considered a promising candidate for EDLC electrode materials because of their high mechanical strength for bending, high electrical conductivity, and higher electrochemical stability [25].

Moreover, activated carbon are very interesting supports for the semiconductor metal oxide, such as  $\text{TiO}_2$  [16-19] and  $\text{ZnO}$  [26, 27] photocatalysts due to its adsorptive properties and high specific surface area. Subramani et al. [28] found that using activated carbon could increase the surface area of catalyst, which led to an

improvement of the performance in photocatalytic activity. In addition, using activated carbon as a support also improved adsorption in visible light region and decreased the band gap energy of catalyst materials because Ti-O-C bond was formed. Therefore, the AC/TiO<sub>2</sub> composite materials could provide high photocatalytic activity under visible light [29].

This research studied the preparation of coconut shell based activated carbon (ACCS) and coconut shell based activated carbon-metal oxide hybrid (ACCS/TiO<sub>2</sub>) catalysts for supercapacitor and photocatalyst applications, respectively. Coconut shell is cost effective and is abundantly available in Thailand [30]. The ACCS powders were prepared by a chemical activation method and the TiO<sub>2</sub> powders were synthesized by a solvothermal process. The resulting products were characterized by scanning electron microscopy (SEM), transmission electron microscopy (TEM), N<sub>2</sub> adsorption-desorption measurement, Raman spectroscopy, and X-ray diffraction (XRD) techniques. The electrochemical properties of the prepared samples were investigated by cyclic voltammetry (CV) and galvanostatic charge-discharge in a symmetrical two-electrode cell. Furthermore, ACCS/TiO<sub>2</sub> hybrid catalysts were fabricated on aluminum substrates by electrophoretic deposition. The photocatalytic activity of the prepared catalysts, using methylene blue as model organic compound was evaluated by studying the photocatalytic efficiency and reusability under ultraviolet light irradiation.

### 3.3 Experimental

#### 3.3.1 Preparation of coconut shell based activated carbon (ACCS)

The coconut shells were carbonized at 600 °C under purified N<sub>2</sub> gas flow for 2 h in a box furnace. In the next step, the carbonized coconut shells were immersed in potassium hydroxide (KOH) solution at a impregnation ratio of 3:1 (KOH:carbonized coconut shells by weight) for 3 h. The samples were heated at 150 °C to remove the humidity. Then the dried samples were activated at 800 °C under N<sub>2</sub> gas flow for 60 min. After cooling, the obtained ACCS was washed with distilled water until it reached pH 7. Commercially available activated carbon (Karbokarn Co., Ltd.) was characterized for comparison. Hereafter, the activated carbon prepared

using coconut shells was called AC-S and the commercial activated carbon was called AC-C.

The surface morphologies of the samples were analyzed through scanning electron microscopy (SEM) (CamScan MX 2000 Scanning electron microscope). The specific surface area and average pore diameter of the samples were measured by nitrogen adsorption, using BET technique (Autosorb-1, Quantachrome). Raman spectra of the samples were obtained using a Raman spectrometer (NTEGRA Spectra, NTMDT).

### **3.3.2 Characterization and testing of coconut shell based activated carbon as electrode material for supercapacitor application**

The electrochemical behaviors of the activated carbon were examined using cyclic voltammetry (CV) and galvanostatic charge-discharge measurements on a potentiostat in a symmetrical two-electrode cell using a liquid electrolyte of 1 M sulfuric acid ( $\text{H}_2\text{SO}_4$ ) solution. The activated carbon powder was mixed with 10 wt % poly(vinylidene fluoride) (PVDF) in dimethylformamide (DMF) solvent to form a viscous slurry. The slurry was coated on stainless steel wire mesh (SUS 304) and dried. The active area was a square of 1 cm x 1 cm.

### **3.3.3 Preparation of $\text{TiO}_2$ /activated carbon hybrid catalysts for photocatalyst application**

Titanium (IV) isopropoxide (TTIP; Acros Organics Crop, >98%), isopropyl alcohol (Carlo erba reagents, >99.7%), distilled water, and AC-S were used as starting materials. Firstly,  $\text{TiO}_2$  powder was synthesized by solvothermal process at 200 °C using a starting solution of TTIP, isopropyl alcohol, and distilled water at a volume ratio of 1: 33: 2. Then, the calcination at 700 °C was carried out. This  $\text{TiO}_2$  sample was designated as ST. The ST/AC-S and P25/AC-S hybrid films were fabricated by firstly depositing activated carbon prepared using coconut shells (AC-S) on the aluminum foil substrate followed by  $\text{TiO}_2$  coating using electrophoretic deposition (EPD) process. For comparison, single-layered films of AC-S, ST and commercially available standard  $\text{TiO}_2$  (P25) were fabricated directly on the aluminum foil substrate. The electrophoretic cell was consisted of two electrodes; anode and

cathode made of stainless steel plate. An aluminum foil substrate was located at the cathode. The applied voltage, deposition time of each layer and distance between two electrodes were controlled at 50 V, 15 min and 2 cm, respectively.

### 3.3.4 Characterization and testing of TiO<sub>2</sub>/activated carbon hybrid catalysts for photocatalyst application

The crystal structures of the synthesized TiO<sub>2</sub> and commercial P25 were characterized by X-ray diffraction (XRD; Bruker D8) using CuK $\alpha$  radiation at a wavelength of 0.1514 nm. The morphology of the samples was evaluated by transmission electron microscopy (TEM; JEOL 2100). Brunauer–Emmett–Teller (BET) method (Quantachrome, Autosorb–1) was used to obtain the specific surface area of the synthesized TiO<sub>2</sub> and commercial P25 powders.

After the films were successfully deposited, the morphology of the resulting films was characterized using a scanning electron microscope (SEM; Hitachi S3400N) and transmission electron microscopy (TEM; JEOL 2100). Additionally, the methylene blue (MB, Carlo Erba Reagents) adsorption method was used to determine the specific surface area of the deposited films. The photocatalytic efficiency of the prepared films for the degradation of MB was evaluated under UV light irradiation (Philips, Hg-Lamp 400W) at light intensity of 5.1 mW/cm<sup>2</sup>. The efficiency of MB removal was calculated by the following equation [31]:

$$\text{Decolorization efficiency (\%)} = \frac{100(C_0 - C)}{C_0} \quad (3.1)$$

where  $C_0$  is the initial concentration of MB before irradiation and  $C$  is the concentration of MB after irradiation for a given time.

## 3.4 Results and discussion

### 3.4.1 Characterization of coconut shell based activated carbon

Figure 3.1 (a) and (b) show the typical SEM images of activated carbon prepared using coconut shells (AC-S) and commercial activated carbon (AC-C). During carbonization process, the breaking of biomass structure to degrade hemicellulose, cellulose, and lignin in coconut shells would be taken place; the

structural ordering of the residual carbon and finally polymerization reaction also occurred. It can be seen clearly that AC-S sample revealed the high pore structure on the surface of carbon particles due to the carbon matrix during the activation, resulting in the expansion of the carbon lattices.

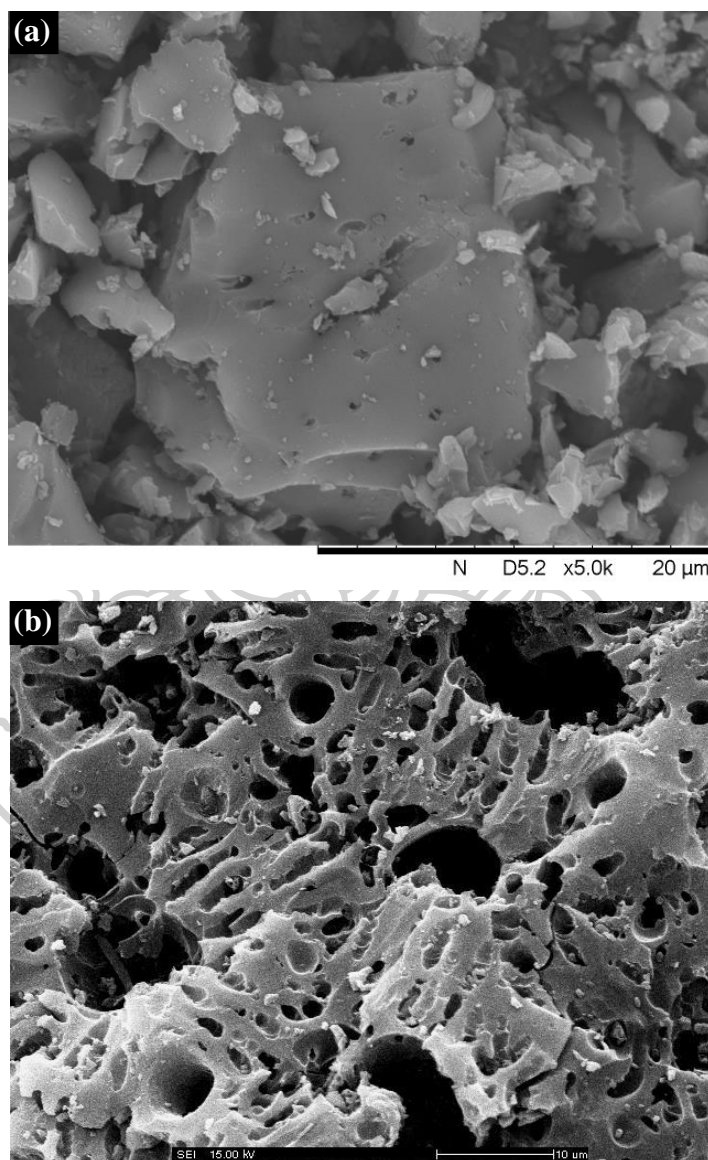


Figure 3.1 SEM micrographs of (a) AC-C and (b) AC-S.

The adsorption profiles of the samples AC-C and AC-S are shown in Figure 3.2. Both the samples indicated rapid uptake of nitrogen gas at low pressure with Type I adsorption characteristic according to the IUPAC classification. This type isotherm shows a high affinity of the adsorbate and adsorbent for each other, and also suggests that the adsorbent is comprised mainly of micropores. The specific surface area calculated by BET method was 817 m<sup>2</sup>/g for the sample AC-C. Meanwhile, the activated carbon sample synthesized in the presence of KOH (AC-S) possessed a high surface area of 1641 m<sup>2</sup>/g. This could be because the KOH activation resulted in the generation of micropores primarily, leading to a higher micropore volume and hence a porous carbon with a higher surface area.

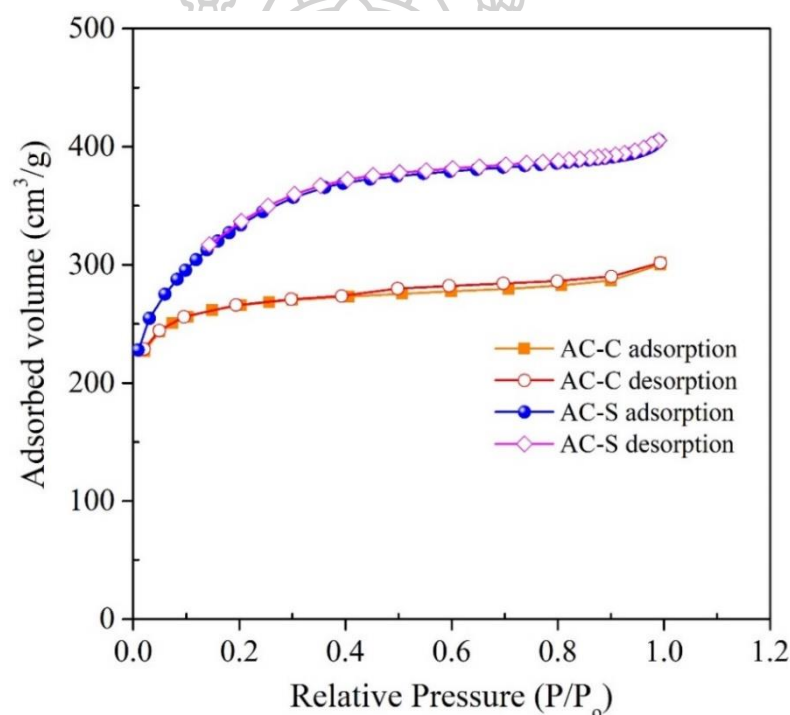


Figure 3.2 N<sub>2</sub> adsorption–desorption isotherms of AC-C and AC-S.

Raman spectroscopy was used to investigate the graphitization of the samples AC-S and AC-C. Figure 3.3 reveals the Raman spectra of the sample AC-S prepared at carbonization temperatures of 800 °C. Two strongest bands at approximately 1350 and 1585 cm<sup>-1</sup> corresponded to D band and G band, respectively [32]. The D peaks are ascribed to the structural defect sites in the hexagonal framework of the wall of AC-S and AC-C and disorder-induced peak (disordered

peak). The G peaks are attributed to an  $E_{2g}$  mode of graphite, which resulted from the  $sp^2$ -bonded carbon atoms in a two-dimensional hexagonal graphitic layer (graphitic peak). The intensity ratio of the D line to the G line ( $R = I_D/I_G$ ) represented the degree of disorder in graphitic layer. The  $I_D/I_G$  ratio of the sample AC-S was 0.76 as calculated from these spectra, suggesting good crystallinity of the graphitic sheets. However, the  $I_D/I_G$  ratio of the sample AC-C was 1.05, indicating higher disorder level in crystal structure [32].

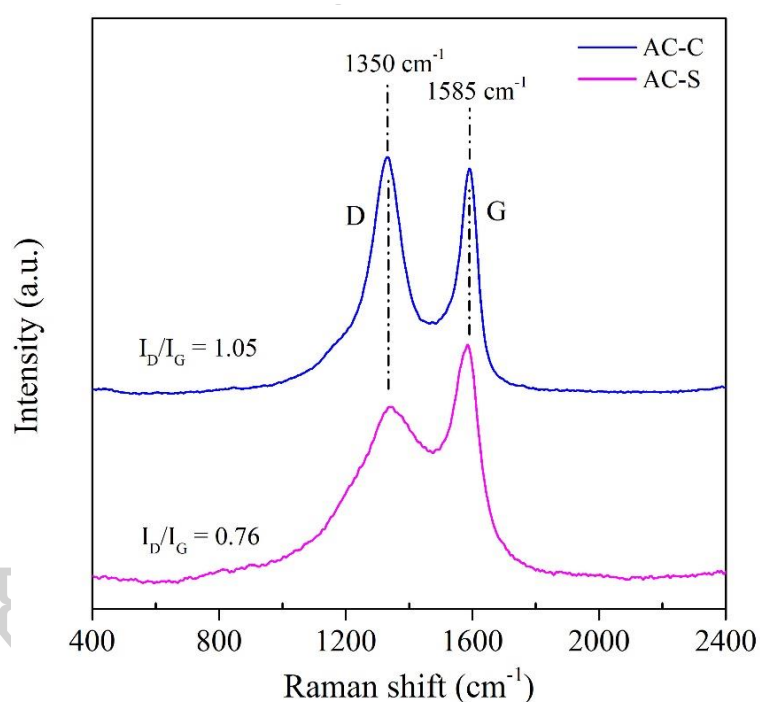


Figure 3.3 Raman spectra of AC-C and AC-S.

### 3.4.2 Electrochemical behavior of coconut shell based activated carbon as electrode material for supercapacitor

To investigate the electrochemical behavior of the samples AC-S and AC-C as electrodes for supercapacitor, CV and galvanostatic charge-discharge measurements were performed in  $H_2SO_4$  solution. The CV measurement was carried out within the potential range of 0.0 - 1.0 V at a scan rate of 5 mV/s. Figure 3.4 shows the CV curves of the samples AC-S and AC-C. The voltammograms are nearly square and no evidence for any redox currents on both the anodic and cathodic sweeps was

shown. These results indicated that each of the samples displayed behavior typical of EDLCs [33]. Considering at the same scan rate, the larger area of CV curve of the sample AC-S indicated higher specific capacitance than the AC-C sample. Wang et al. [34] also reported that amphiphilic carbon material-based activated carbons with higher specific capacitance showed larger area of CV curves because of their high specific surface area. The sample AC-S gave the higher specific capacitance value (171.13 F/g) than the sample AC-C (126.33 F/g). This resulted from the EDLC energy storage mainly based on the charge accumulation in the electric double layers formed at the electrode/electrolyte interface region. Therefore, the specific capacity of EDLCs was dependent greatly on the specific surface area of electrode material, which was consistent with the earlier studies [33-35].

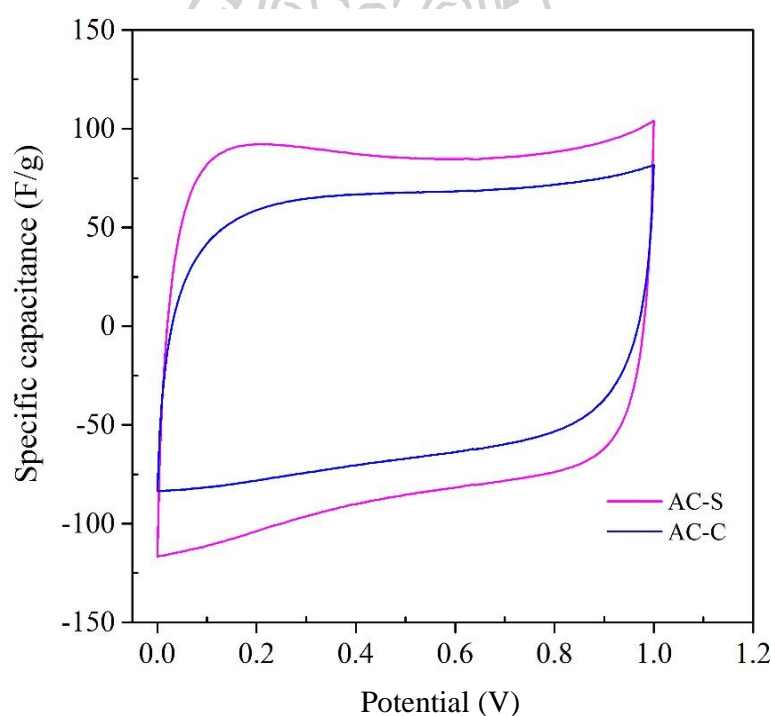


Figure 3.4 Two-electrode system: the CV curves of AC-S and AC-C electrodes at a scan rate of 5 mV/s in  $\text{H}_2\text{SO}_4$  electrolyte solution.

Figure 3.5 (a) and (b) present the CV curves of the samples AC-S and AC-C at scan rates from 5 to 100 mV/s. All the curves demonstrated a quasi-rectangular shape, implying that the specific capacitance is mainly contributed by the double-layer capacitance based on fast charge–discharge. However, small and high distorted

CV curves for the samples AC-S and AC-C at scan rate of 100 mV/s were found. The CV curves of the sample AC-S retained good rectangular-like shapes and reversible electrochemical behavior, even when raised to 100 mV/s, indicating its good rate capability of the device. It was suggested that the rectangular-like degree of the CV curve is closely related to the charge transfer and ion diffusion rate in the porous of the AC-S electrode.

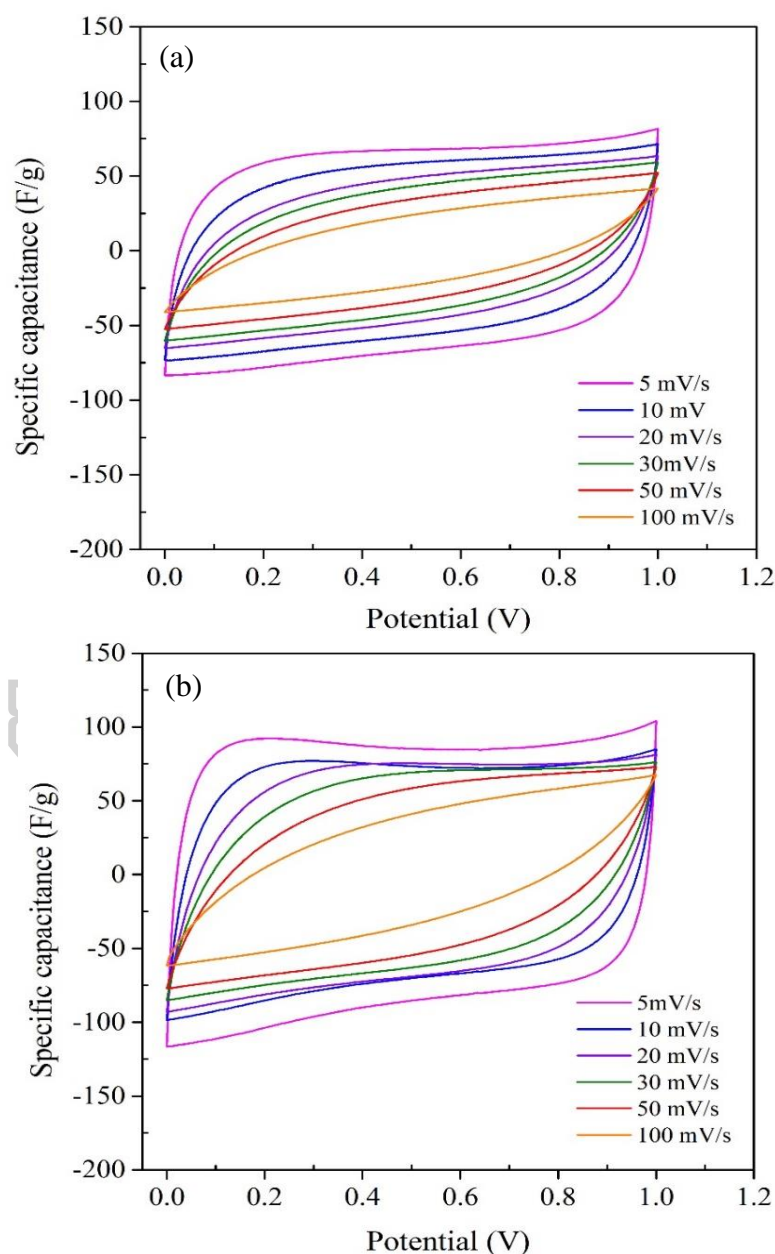


Figure 3.5 Two electrode system: the CV curves of (a) AC-C electrode and (b) AC-S electrode at various scan ranging from 5 to 100 mV/s.

The specific capacitances ( $C_s$ ) calculated from the CV curves as a function of scan rate is shown in the Figure. 3.6. The specific capacitance of the samples AC-S and AC-C was calculated from cyclic voltammetry curves, using the following equation [36]:

$$C_s = \frac{2 \times \int IdV}{s \times m \times \Delta V} \quad (3.2)$$

where  $C_s$  is the gravimetric specific capacitance (F/g),  $I$  is the response current (A),  $\Delta V$  is the applied potential (V),  $m$  is the total mass of the active material (g) in the two electrodes,  $v$  is the voltage scan rate (V/s) and  $\Delta V$  is the operating voltage window (V).

The specific capacitance of the samples AC-S and AC-C decreased from 171.13 F/g to 74.58 F/g and 126.33 F/g to 47.97 F/g as the scan rate increased from 5 mV/s to 100 mV/s. It was obviously seen in Figure 3.6 that the gravimetric capacitance of the AC-S capacitor was always greater than that of the AC-C capacitor at any scan rate, and these results apparently indicated the better supercapacitive behavior and rate capability of the sample AC-S.

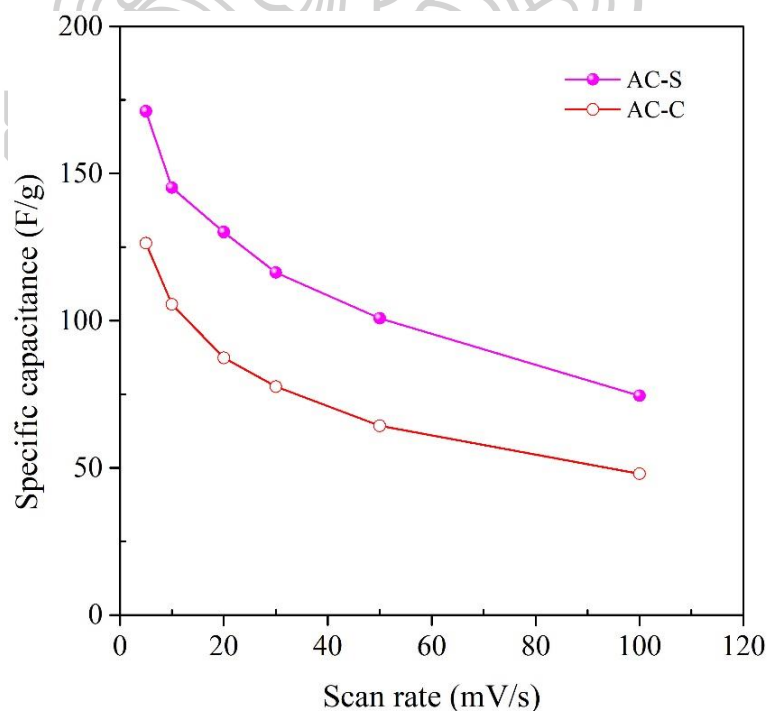


Figure 3.6 Two electrode system: specific capacitances of AC-C and AC-S electrodes as a function at various scan ranging from 5 to 100 mV/s.

The galvanostatic charge-discharge test was carried out to confirm the results obtained from the CV analysis. Figure 3.7 exhibits the galvanostatic charge-discharge curves of the AC-S sample at a constant current density of 0.5 to 6 A/g in the potential range from 0 to 1.0 V. Moreover, the quasi-linear galvanostatic charge-discharge curve at various current densities confirmed its good EDLC feature. The specific capacitance ( $C_m$ ) can be calculated according to the corresponding galvanostatic discharge curves using the following equation [37]:

$$C_s = \frac{4I \cdot \Delta t}{\Delta V \cdot m} \quad (3.3)$$

where  $C_s$  is the specific capacitance (F/g),  $I$  is the discharge current (A),  $\Delta t$  is the discharge time (s),  $\Delta V$  is the voltage difference (V), and  $m$  is the total mass of the active material (g) in the two electrodes.

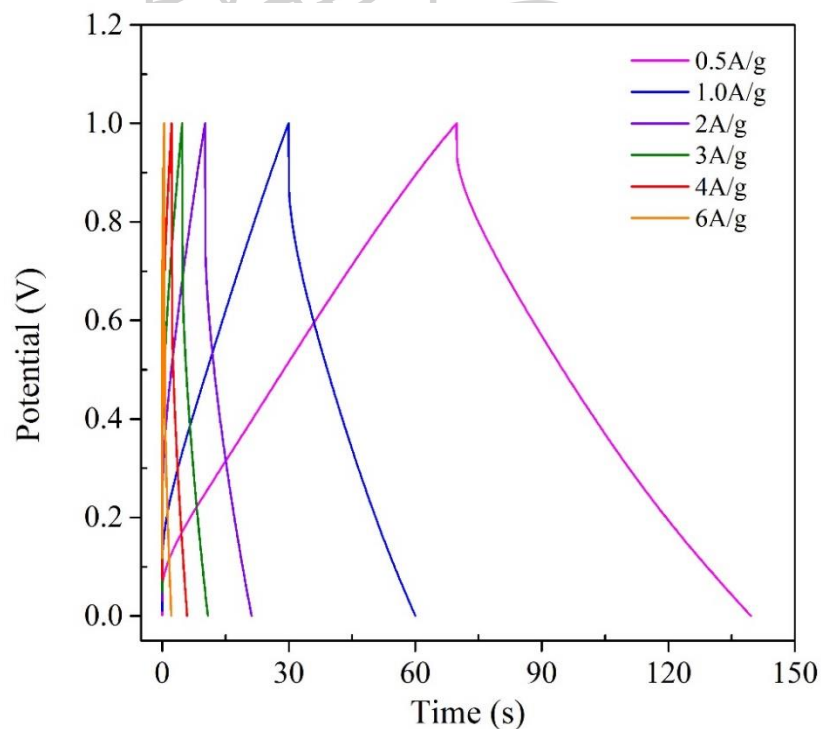


Figure 3.7 Galvanostatic charge-discharge curves of symmetric supercapacitor of the AC-S electrode at different current densities.

The effect of current density on the specific capacitance of the sample AC-S is shown in the inset of Figure 3.8. Generally, the specific capacitance decreased gradually with increasing current density due to ohmic drop at high current density [38]. The maximum capacitance of 149.65 F/g was achieved at a current density of 0.5 A/g. Moreover, the capacity retention was approximately 65% when the current density was increased from 0.5 A/g to 4 A/g. The specific capacitance was still as high as 83.15 F/g (about 56%) even when the current density was raised up to 6 A/g. Power density and energy density of supercapacitor electrodes are important parameters for evaluation of the electrochemical performances. The power density ( $P$ , W/kg) and energy density ( $E$ , Wh/kg) of supercapacitors can be calculated using the data of galvanostatic charge-discharge at various current densities from the following relations [39]:

$$E = \frac{C_s (\Delta V)^2}{8 \times 3600} \quad (3.4)$$

$$P = \frac{E}{t} \quad (3.5)$$

where  $C_s$  is the specific capacitance (F/g),  $t$  is the discharge time (s), and  $\Delta V$  is the voltage difference (V).

The Ragone plot is also presented in Figure 3.8 (power density *vs.* energy density). The energy density of the sample AC-S reached 4.64 Wh/kg at a power density of 239.66 W/kg and decreased steadily as the power density increased. Furthermore, the sample maintained an energy density of 0.61 Wh/kg even at a high power density of 1397.46 W/kg. These observations suggested that the sample AC-S electrode can be considered as good candidate electrode material for supercapacitor application.

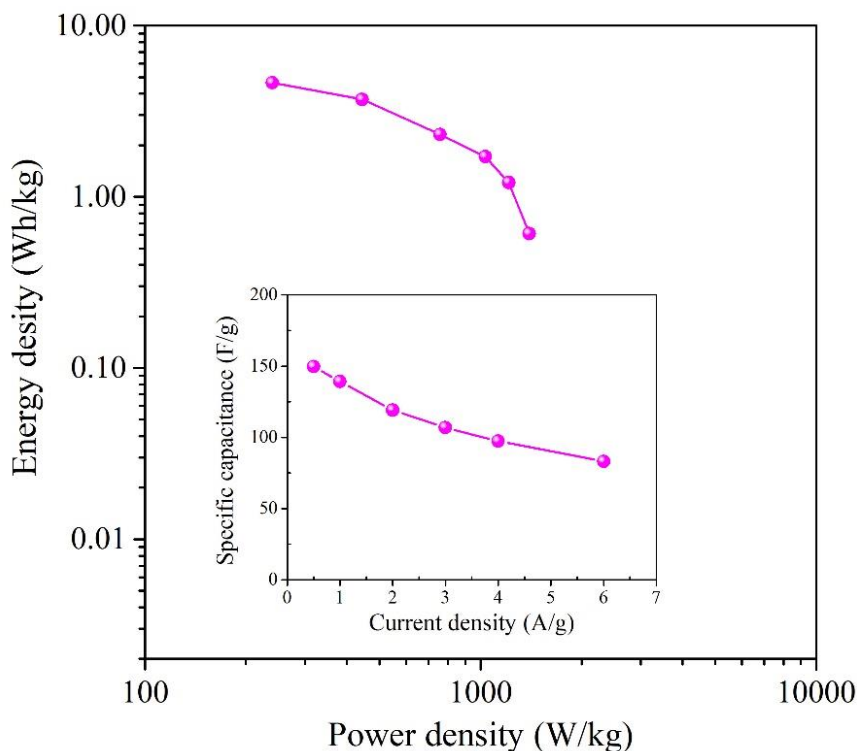


Figure 3.8 Ragone plot of the AC-S electrode carbonized at 800 °C measured at various current densities in H<sub>2</sub>SO<sub>4</sub> electrolyte solution. The inset shows specific capacitance dependence on current density.

### 3.4.3 Characterization of the synthesized TiO<sub>2</sub> and TiO<sub>2</sub>/coconut shell based activated carbon photocatalyst

The XRD patterns of commercial TiO<sub>2</sub> (P25) and synthesized TiO<sub>2</sub> (ST) powders are revealed in Figure. 3.9. The commercial P25 powder contained a mixture of anatase and rutile phases, whereas the ST powder is composed of only anatase phase. The phase composition of the samples P25 and ST is reported in Table 3.1. All the diffraction peaks of P25 can be clearly indexed as anatase and rutile consistent with JCPDS File no. 00–021–1272 and 00–021–1276, respectively. All the diffraction peaks of ST can be clearly identified as anatase phase, in consistent with JCPDS File no. 00–021–1272. The average crystallite sizes of the samples P25 and ST calculated using Scherrer's formula are reported in Table 3.1 from the diffraction peak at 25.28 and 27.45° for anatase and rutile phases, respectively.

Table 3.1 Phase content, crystallite size and SBET of the samples P25 and ST.

Sample	Phase content (%)	Crystallite size (nm)	$S_{\text{BET}}$ ( $\text{m}^2/\text{g}$ )
P25	Anatase	75	48.47
	Rutile	25	23.87
ST	Anatase	100	29.53

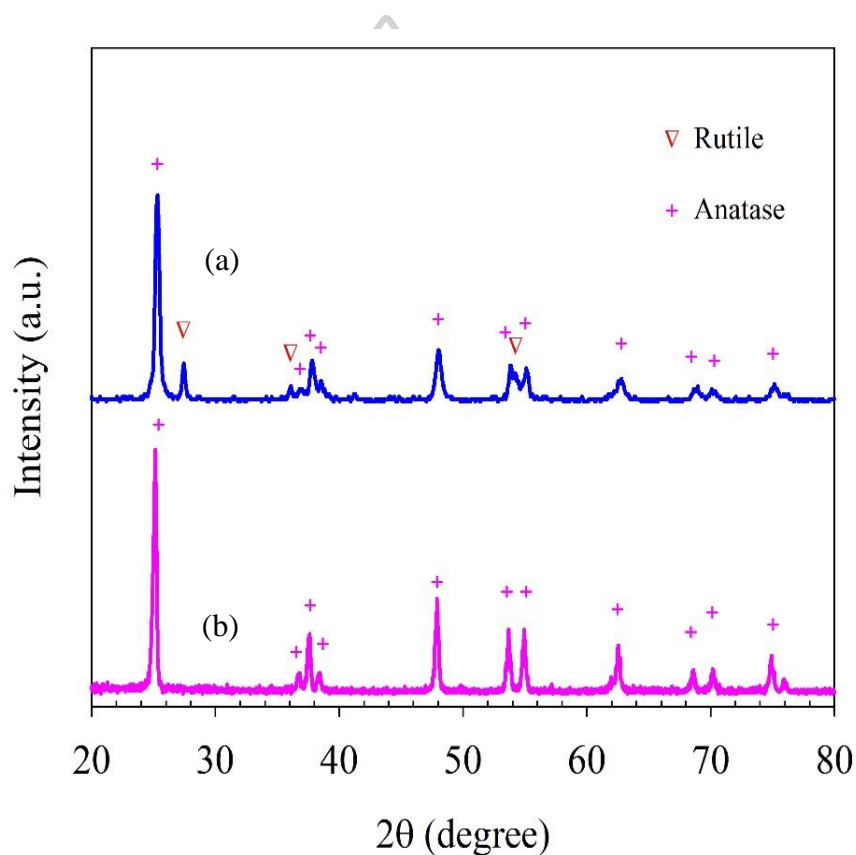


Figure 3.9 XRD patterns of the samples (a) P25 and (b) ST.

The TEM images of P25 and ST powders are shown in Figure. 3.10. It was found that the particle size of ST was larger than that of P25, which was in good agreement with the XRD observations. The specific surface area ( $S_{\text{BET}}$ ) of P25 and ST powders was measured by BET method shown in Table 3.1. The specific surface area of the sample ST was slightly lower than that of the sample P25. These results were

consistent with those reported earlier [40]. This might be because the particles with smaller sizes had larger surface areas.

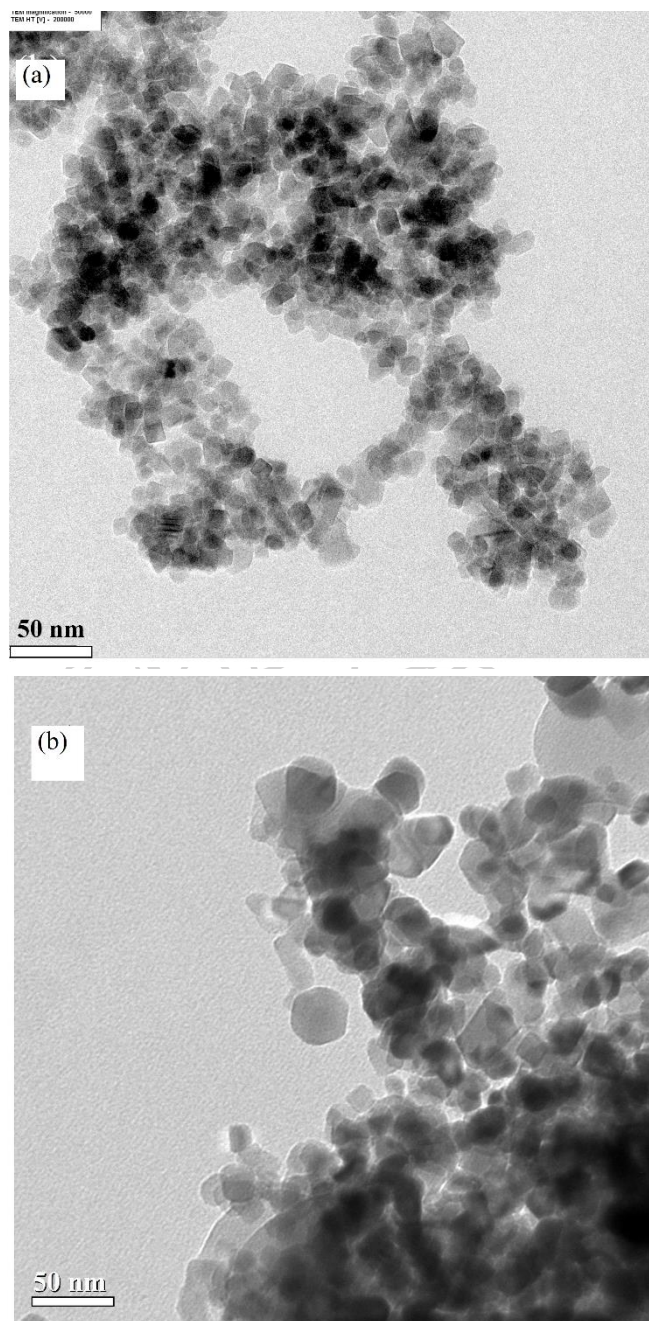


Figure 3.10 TEM micrographs of the samples (a) P25 and (b) ST.

Figure 3.11 (a)–(b) presents the surface morphology of single-layered films of P25 and ST after deposition on aluminum substrate. The ST film had porous morphology and loosely textured structure with numerous holes. Meanwhile, the P25 film had lower porous morphology with a better packing of particles resulting in a denser coating with crack formation because smaller particles move much more quickly and easily than larger ones at the same electric field [41]. Figure 3.11 (c)–(d) displays the SEM micrographs of the double-layered films for different TiO<sub>2</sub> particles on AC-S layer deposited on the aluminum substrate. The SEM images indicated that the AC-S layer could be completely coated by P25 particles, whereas ST particles did not completely cover on the AC-S layer. Santillan et al. [42] reported that the deposition efficiency for EPD technique depended on the suspension stability. For the ST film, TiO<sub>2</sub> particles with larger particle size tended to have more unstable, leading to a rough surface.

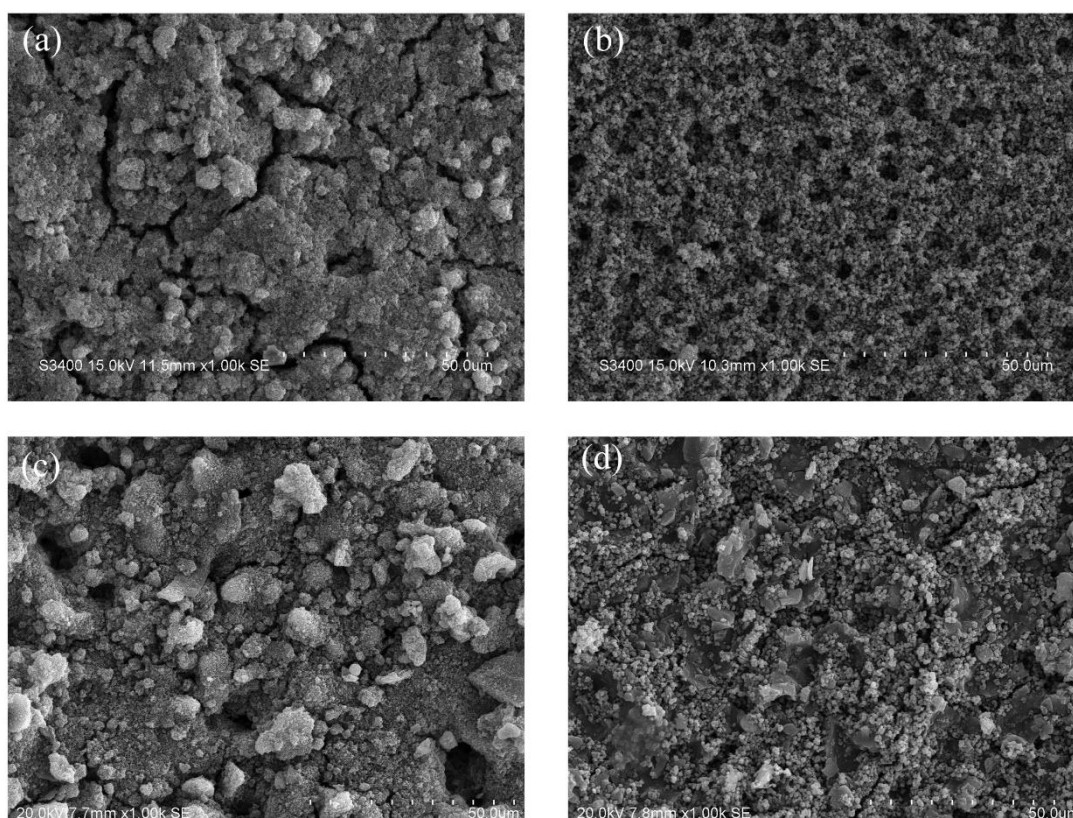


Figure 3.11 SEM images of (a) P25 film, (b) ST film, (c) P25/AC-S film, and (d) ST/AC-S film.

The adsorption of MB in the equilibrium for single-layered and double-layered films is demonstrated in Figure 3.12. The amount of solute adsorbed per unit weight of adsorbent at equilibrium ( $Q_e$  (mg/g)) is a function of concentration in the liquid phase at equilibrium ( $C_e$  (mg/L)). The specific surface area can be determined using the following equation [43]:

$$S_{MB} = (q_m \times A_{MB} \times N_A) / (M \times 1000) \quad (3.6)$$

where  $S_{MB}$  is the specific surface area ( $\text{m}^2/\text{g}$ ),  $A_{MB}$  is the occupied surface area of one molecule of MB ( $197.2 \text{ \AA}^2$ ),  $N_A$  is Avogadro's number ( $6.02 \times 10^{23} \text{ mol}^{-1}$ ),  $M$  is the molecular weight of MB (319.89 g/mol) and  $q_m$  is the number of molecules of MB adsorbed at the monolayer (mg/g), which is calculated from the Langmuir model. An empirical model was shown as follows [44]:

$$\frac{C_e}{Q_e} = \frac{C_e}{Q_m} + \frac{1}{KQ_m} \quad (3.7)$$

where  $C_e$  (mg/L) is the concentration in the liquid phase at equilibrium,  $Q_e$  (mg/g) is the amount of solute adsorbed per unit weight of adsorbent at equilibrium,  $K$  (L/mg) is the Langmuir adsorption constant and  $Q_m$  (mg/g) is the theoretical maximum adsorption capacity.

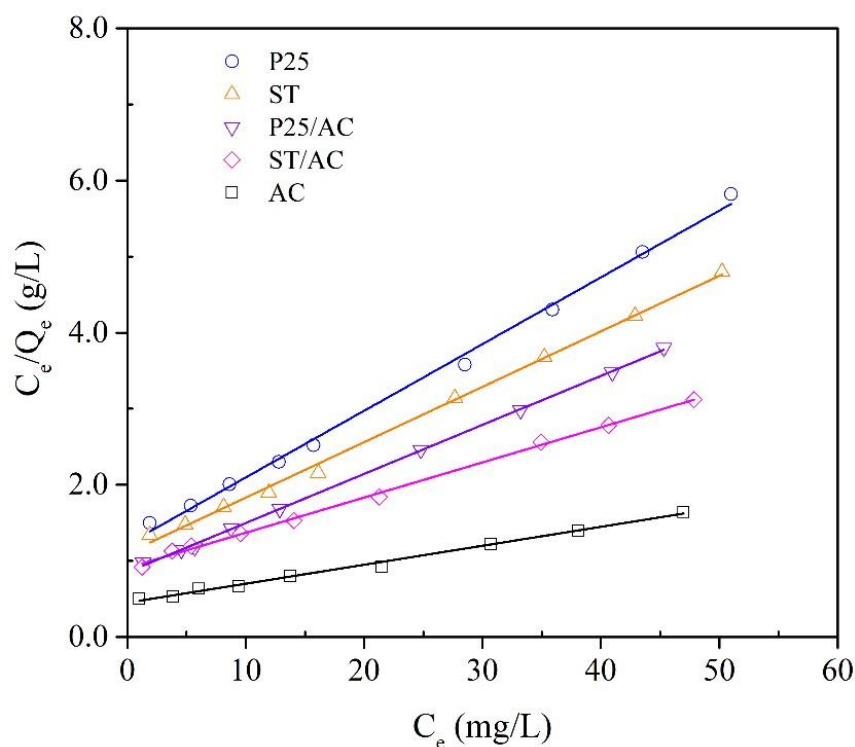


Figure 3.12 Langmuir adsorption isotherm fitted to the experimental data for MB adsorption onto various films.

The adsorption method of MB demonstrated that the AC-S film gave the highest specific surface area. The result of this experiment corresponded with the result of BET surface area for the AC-S powders. The specific surface area obtained from the measurement of MB adsorption for the ST film was higher than that for the P25 film, which was opposite to the results obtained from BET measurement due to more loosely packed particles and numerous holes of the ST film. The coating of TiO<sub>2</sub> powders on AC-S layer resulted in the enhancement of the specific surface area of double-layered films, as presented in Table 3.2. The ST/AC-S film had higher specific surface area than the P25/AC-S film. This is probably due to incomplete coverage of the ST powders on the AC-S layer.

Table 3.2 Langmuir parameter and specific surface area of various films.

Sample	Langmuir parameter			$S_{MB}$ ( $m^2/g$ )
	$q_m$ (mg/g)	K (L/mg)	$R^2$	
P25	11.41	0.029	0.997	28.84
ST	13.72	0.026	0.998	34.70
P25/AC-S	15.50	0.030	0.999	39.21
ST/AC-S	21.65	0.020	0.998	54.75
AC-S	40.16	0.022	0.995	101.58

The photodegradation of MB was followed by measuring the UV–vis spectra of the reaction mixture. Figure 3.13(a) presents the change in absorption spectra of MB in presence of the ST/AC-S film under UV irradiation at different time intervals. The strong absorption band located at  $\lambda = 663$  nm for MB dye rapidly decreased with increasing irradiation time and almost disappeared after 60 min. To study the photocatalytic efficiency of the resulting films, the degradation of MB used as a model dye pollutant was tested under UV irradiation, as shown in Figure 3.13(b). The ST/AC-S double-layered film showed the maximum efficiency for MB removal of 96.6% at 60 min. This is because the ST/AC-S double-layered film with high specific surface area can adsorb MB dye by providing more available adsorption sites for binding MB and thereby enhancing sorption–degradation [45].

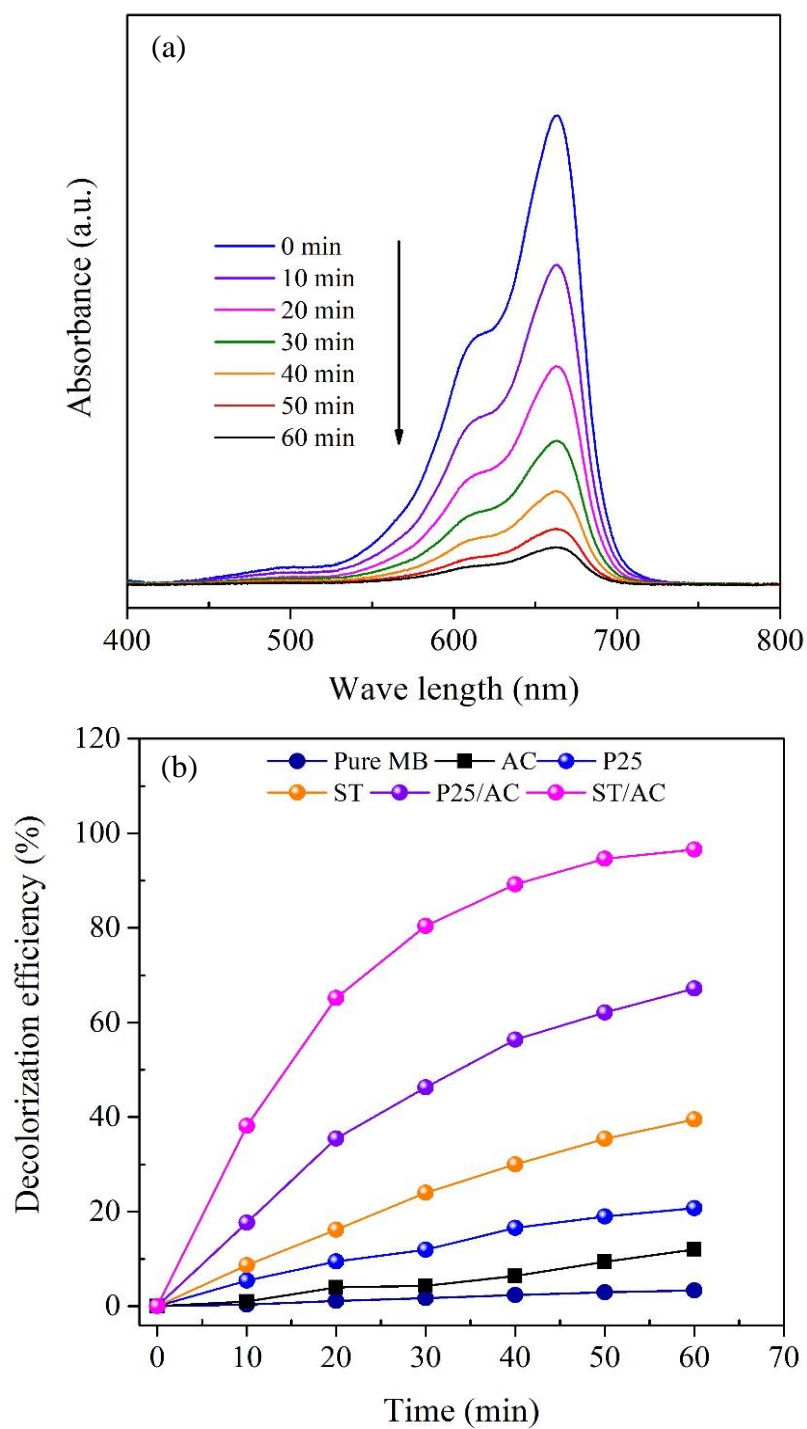


Figure 3.13 (a) The relation between absorbance and wavelength as a function of illumination time of the ST/AC-S film for the photocatalytic degradation of MB and (b) photocatalytic efficiency for MB degradation using various photocatalysts.

The kinetics of MB degradation profiles are illustrated in Figure 3.14. The photocatalytic degradation of MB fitted pseudo-first-order kinetics expressed as:

$$-dC/dt = k_{app} C \quad (3.8)$$

Integrating this equation (with the restriction  $C = C_0$  at  $t = 0$ , with  $C_0$  being the initial concentration and  $t$  is the reaction time) gives the following equation [46]:

$$\ln(C_0 / C) = k_{app} t \quad (3.9)$$

where  $C$  is the reactant concentration at a given time. The apparent rate constant ( $k_{app}$ ) of the photocatalytic reaction and decolorization efficiency are reported in Table 3.3. The ST/AC-S double-layered film gave the highest value of  $k_{app}$  and decolorization efficiency because of its high specific surface area.

Table 3.3 The photocatalytic parameters for MB removal using various photocatalyst films.

Sample	$R^2$	$k_{app}$ ( $\text{min}^{-1}$ )	Decolorization efficiency at 60 min (%)
AC-S	0.956	0.002	12.00
P25	0.977	0.004	20.74
ST	0.997	0.009	39.51
P25/AC-S	0.991	0.020	67.20
ST/AC-S	0.997	0.056	96.60

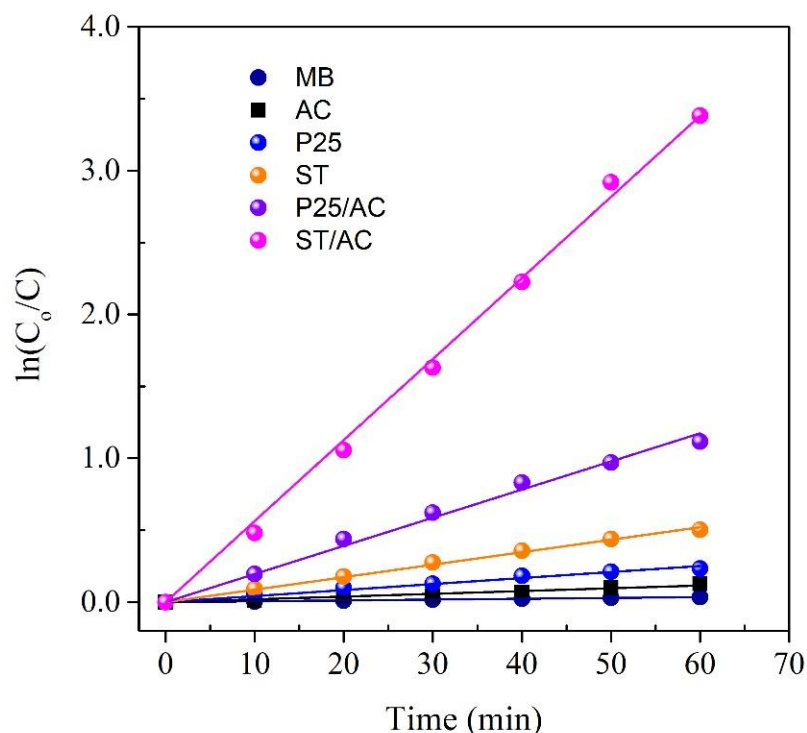


Figure 3.14 Degradation kinetics of MB dye over different film catalysts.

The reusability of the photocatalysts is one of the most important properties for their practical application to reduce waste and operating cost. Therefore, the photocatalyst reusability was investigated. The main advantage of the ST/AC-S double-layered film was easily recovered from the reaction mixture without filtration. The recovered catalyst was then reused for the MB photodegradation under the same reaction condition as explained above. The reusability of ST/AC-S double-layered film tested for five cycles is shown in Figure 3.15. The ST/AC-S catalyst film still preserved its photocatalytic efficiency of 87.8% for MB degradation after being reused for five times. This reusability of the ST/AC-S film is due to the stability and resistance to photocorrosion. Therefore, the ST/AC-S film can be used as an efficient photocatalyst for the degradation of MB dye.

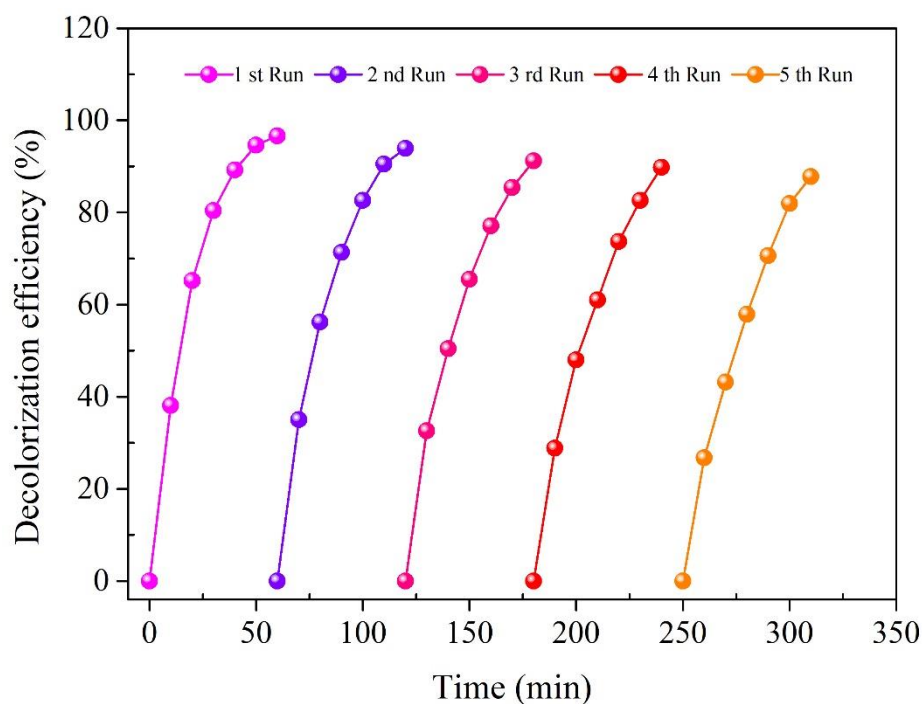


Figure 3.15 Reusability of the ST/AC-S film for five cycles.

### 3.5 Conclusions

The highly porous activated carbon was successfully prepared from agricultural coconut shell waste as precursor with KOH activation at impregnation ratio of 3:1 and carbonization at 800 °C. In electrochemical investigations, both the commercial and synthesized activated carbon electrodes presented EDLC behavior, and a general trend of specific capacitance increased along with the increase in specific surface area. Between the commercial and synthesized activated carbons, the synthesized activated carbons offered high power and energy density and greater specific capacitance. The maximum specific capacitance of 149.65 F/g was obtained at a current density of 0.5 A/g. Furthermore, this resulting electrode also showed good rate capability and the specific capacitance decreased less than 35% (65% capacity retention) as the current density was raised from 0.5 to 4 A/g. This obtained material is a promising and useful electrode for electrochemical supercapacitors. The TiO<sub>2</sub>/activated carbon double-layered film photocatalysts were successfully fabricated using an electrophoretic deposition technique without additives. The photocatalytic efficiency of methylene blue degradation for TiO<sub>2</sub>/activated carbon films was

investigated using methylene blue as a model pollutant. The synthesized TiO<sub>2</sub>/activated carbon films showed higher photocatalytic efficiency than the commercial TiO<sub>2</sub>/activated carbon film and their single-layered films due to more available sites for binding MB molecules. In addition, a reusability study also demonstrated that the double-layered film of the synthesized TiO<sub>2</sub>/activated carbon with high photocatalytic efficiency and stability could be a promising candidate for its practical applications.

### 3.6 References

1. Daud, W.M.A.W., Ali, W.S.W. and Sulaiman, M.Z., The effects of carbonization temperature on pore development in palm-shell-based activated carbon. *Carbon*, 2000. **38**(14): p. 1925-1932.
2. Daud, W.M.A.W. and Ali, W.S.W., Comparison on pore development of activated carbon produced from palm shell and coconut shell. *Bioresource Technology*, 2004. **93**(1): p. 63-69.
3. Adinata, D., Daud, W.M.A.W. and Aroua, M.K., Preparation and characterization of activated carbon from palm shell by chemical activation with K<sub>2</sub>CO<sub>3</sub>. *Bioresource Technology*, 2007. **98**(1): p. 145-149.
4. Kirubakaran, C.J., Krishnaiah, K. and Seshadri, S.K., Experimental study of the production of activated carbon from coconut shells in a fluidized bed reactor. *Industrial & engineering chemistry research*, 1991. **30**(11):p. 2411-2416.
5. Mi, J., et al., Coconut-shell-based porous carbons with a tunable micro/mesopore ratio for high-performance supercapacitors. *Energy & Fuels*, 2012. **26**(8): p. 5321-5329.
6. Hayashi, J.I., et al., Preparing activated carbon from various nutshells by chemical activation with K<sub>2</sub>CO<sub>3</sub>. *Carbon*, 2012. **40**(3): p. 2381-2386.
7. He, X., et al., Efficient preparation of biomass-based mesoporous carbons for supercapacitors with both high energy density and high power density. *Journal of Power Sources*, 2013. **240**: p.109-113.

8. Wang, G., Zhang, L. and Zhang, J., A review of electrode materials for electrochemical supercapacitors. *Chemical Society Reviews*, 2012. **41**(2): p. 797-828.
9. Ahmadpour, A. and Do, D.D., The preparation of active carbons from coal by chemical and physical activation. *Carbon*, 1996. **34**(4): p. 471-479.
10. Lozano-Castelló, D., et al., Influence of pore structure and surface chemistry on electric double layer capacitance in non-aqueous electrolyte. *Carbon*, 2003. **41**(9): p. 1765-1775.
11. Dantas, T.L., et al., Carbon dioxide-nitrogen separation through adsorption on activated carbon in a fixed bed. *Chemical Engineering Journal*, 2011. **169**(1-3): p. 11-19.
12. Hameed, B.H., Tan, I.A.W. and Ahmad, A.L., Preparation of oil palm empty fruit bunch-based activated carbon for removal of 2,4,6-trichlorophenol: Optimization using response surface methodology. *Journal of Hazardous Materials*, 2009. **164**(2-3): p. 1316-1324.
13. Liu, M.C., et al., Porous wood carbon monolith for high-performance supercapacitors. *Electrochimica Acta*, 2012. **60**: p. 443-448.
14. Jiang, J., et al., Highly ordered macroporous woody biochar with ultra-high carbon content as supercapacitor electrodes. *Electrochimica Acta*, 2013. **113**: p. 481-489.
15. Jin, H., et al., A high-performance carbon derived from corn stover via microwave and slow pyrolysis for supercapacitors. *Journal of Analytical and Applied Pyrolysis*, 2014. **110**: p. 18-23.
16. Zhang, X., Zhou, M. and Lei, L., Preparation of photocatalytic TiO<sub>2</sub> coatings of nanosized particles on activated carbon by AP-MOCVD. *Carbon*, 2005. **43**(8): p. 1700-1708.
17. Ao, Y., et al., Low temperature preparation of anatase TiO<sub>2</sub>-activated carbon composite film. *Applied Surface Science*, 2008. **254**(13): p. 4001-4006.
18. Ao, Y., et al., Low temperature preparation of anatase TiO<sub>2</sub>-coated activated carbon. *Colloids and Surfaces A: Physicochemical and Engineering Aspects*, 2008. **312**(2-3): p. 125-130.

19. Andriantsiferana, C., Mohamed, E.F. and Delmas, H., Photocatalytic degradation of an azo-dye on TiO<sub>2</sub>/activated carbon composite material. *Environmental Technology*, 2014. **35**(3): p. 355-363.
20. Li, L., et al., A renewable bamboo carbon/polyaniline composite for a high-performance supercapacitor electrode material. *Journal of Solid State Electrochemistry*, 2012. **16**(3): p. 877-882.
21. Portet, C., et al., Influence of carbon nanotubes addition on carbon-carbon supercapacitor performances in organic electrolyte. *Journal of power sources*, 2005. **139**(1-2): p. 371-378.
22. Alvi, F., et al., Graphene-polyethylenedioxythiophene conducting polymer nanocomposite based supercapacitor. *Electrochimica Acta*, 2011. **56**(25): p. 9406-9412.
23. Kim, B.H., et al., Solvent-induced porosity control of carbon nanofiber webs for supercapacitor. *Journal of Power Sources*, 2011. **196**(23): p. 10496-10501.
24. Nandhini, R., et al., Supercapacitor electrodes using nanoscale activated carbon from graphite by ball milling. *Materials Letters*, 2012. **87**: p. 165-168.
25. Kaempgen, M., et al., Printable thin film supercapacitors using single-walled carbon nanotubes. *Nano letters*, 2009. **9**(5): p. 1872-1876.
26. Byrappa, K., et al., Impregnation of ZnO onto activated carbon under hydrothermal conditions and its photocatalytic properties. *Journal of Materials Science*, 2006. **41**(5): p. 1355-1362.
27. Sobana, N., Muruganandam, M. and Swaminathan, M., Characterization of AC-ZnO catalyst and its photocatalytic activity on 4-acetylphenol degradation. *Catalysis Communications*, 2008. **9**(2): p. 262-268.
28. Subramani, A., et al., Hydrothermal preparation and characterization of TiO<sub>2</sub>:AC composites. *Materials Letters*, 2007. **61**(26): p. 4828-4831.
29. Lin, X., et al., Carbon-doped mesoporous TiO<sub>2</sub> film and its photocatalytic activity. *Microporous and Mesoporous Materials*, 2011. **142**(1): p. 276-281.
30. Papong, S., et al. (2004). "**Overview of biomass utilization in Thailand.**" In *ASEAN Biomass Meeting*, p. 1-10.

31. Pongchan, G., Ksapabutr, B. and Panapoy, M., One-step synthesis of flower-like carbon-doped ZrO<sub>2</sub> for visible-light-responsive photocatalyst, *Materials and Design* 89 (2016) 137-145.
32. Lee, C.J., Park, J. and Jeong, A.Y., Catalyst effect on carbon nanotubes synthesized by thermal chemical vapor deposition. *Chemical Physics Letters*, 2002. **360**(3-4): p. 250-255.
33. Ko, J.M. and Kim, K.M., Electrochemical properties of MnO<sub>2</sub>/activated carbon nanotube composite as an electrode material for supercapacitor. *Materials Chemistry and Physics*, 2009. **114**(2-3): p. 837-841.
34. Wang, J., et al., Preparation of mesoporous carbons from amphiphilic carbonaceous material for high-performance electric double-layer capacitors. *Journal of Power Sources*, 2011. **196**(1): p. 550-558.
35. Yang, M., et al., Preparation and electrochemical performance of polyaniline-based carbon nanotubes as electrode material for supercapacitor. *Electrochimica Acta*, 2010. **55**(23): p. 7021-7027.
36. Chen C, et al., Three-dimensional scaffolding framework of porous carbon nanosheets derived from plant wastes for high-performance supercapacitors. *Nano Energy*. 2016. **27**: p.377-389.
37. Deng, L., et al., Graphene-MnO<sub>2</sub> and graphene asymmetrical electrochemical capacitor with a high energy density in aqueous electrolyte. *Journal of power sources*, 2011. **196**(24): p. 10782-10787.
38. Kang, E., Jeon, G. and Kim, J.K., Free-standing, well-aligned ordered mesoporous carbon nanofibers on current collectors for high-power micro-supercapacitors. *Chemical Communications*, 2013. **49**(57): p. 6406-6408.
39. Yang, M., et al., Preparation and electrochemical performance of polyaniline-based carbon nanotubes as electrode material for supercapacitor. *Electrochimica Acta*, 2010. **55**(23): p. 7021-7027.
40. Li, Z.Y., et al., Effect of TiO<sub>2</sub> Particle Size on the Performance of Flexible Dye Sensitized Solar Cells. *Journal for Nanoscience and Nanotechnology*, 2015. **15**(9): p: 6675.
41. Kollath, V.O., et al., AC vs. DC Electrophoretic Deposition of Hydroxyapatite

- on Titanium. *Journal of the European Ceramic Society*, 2013. **33**(13-14): p.2715-2721.
42. Santillán, M.J., et al., Characterization of TiO<sub>2</sub> nanoparticle suspensions for electrophoretic deposition, *Journal of Nanoparticle Research*, 2008. **10**(5): pp.787-793.
43. Itodo, A.U., Itodo, H.U. and Gafar, M.K., Estimation of Specific Surface Area Using Langmuir Isotherm Method, *Journal of Applied Sciences and Environmental Management*, 2010. **14**(4): p: 141 - 145
44. Meng, L., et al., Hierarchically porous silicon–carbon–nitrogen hybrid materials towards highly efficient and selective adsorption of organic dyes, *Scientific reports*, 2015. **5**: p.7910.
45. Aljeboree, A.M., Alshirifi, A.N. and Alkaim, A.F., Kinetics and equilibrium study for the adsorption of textile dyes on coconut shell activated carbon, *Arabian Journal of Chemistry*, 2017. **10**: p.S3381-S3393.
46. Ullah, K., et al., Microwave assisted synthesis of a noble metal-graphene hybrid photocatalyst for high efficient decomposition of organic dyes under visible light, *Materials Science and Engineering: B*, 2014. **180**: p.20-26.



## Chapter 4

### Assembly Three Dimensional Bismuth Titanate (3D-BiT) by Extrusion-Based Fuse Deposition Modeling Technique

#### 4.1 Abstract

Bismuth titanate ( $\text{Bi}_4\text{Ti}_3\text{O}_{12}$ , BiT) was synthesized via sol-gel technique and combined with polyvinylpyrrolidone (PVP) to obtain a thick paste composite for three dimensional shaping by extrusion-based fuse deposition modeling (FDM) technique. The phase compositions were investigated by X-ray diffractometry (XRD). Dilatometry measurement was performed to find out the suitable sintering temperature. Single phase with orthorhombic structure of BiT was obtained after calcination at  $850^\circ\text{C}$  for 1 h. The thick paste with different volume percentage of PVP (1.0, 3.0, 7.5, 20 vol.%) before printing was evaluated by rheology to optimize the extrusion condition. At 3.0 vol. % of PVP, the printing speed of thick paste material was enlarged over 50% of BiT gel.

#### 4.2 Introduction

Three-dimensional printing, also well-known as the extrusion-based fuse deposition modeling (FDM) is one of the most attractive fabrication techniques for fabrication of three dimensional objects [1]. There are several advantages over traditional ceramic fabrication process due to its ability to provide objects with complex geometries in short time processing, relatively low operating cost, user-friendly method and a wide variety of various types of printing materials [2]. Sun et al. [3] prepared lithium ion micro-battery by FDM technique. The obtained micro-battery exhibited high energy and power density, suggesting that it could be applied in autonomously powered micro devices. Recently, Castles et al. [4] fabricated 3D dielectric material using barium titanate ( $\text{BaTiO}_3$ ) powder as filler and ABS polymer as matrix using FDM technique. The dielectric constant of composite with 20 vol. % of  $\text{BaTiO}_3$  was 6.24, which matched those of bulk unprinted materials, indicating that the FDM technique can be applied for manufacturing ferroelectric and dielectric composites materials.

Bismuth titanate ( $\text{Bi}_4\text{Ti}_3\text{O}_{12}$ , BiT) is one of bismuth based ferroelectric compounds and belongs to the Aurivillius compounds family that can be represented by the general formula:  $(\text{Bi}_2\text{O}_2)^{2-}(\text{A}_{m-1}\text{B}_m\text{O}_{3m+1})^{2+}$ . Its crystalline structure consists of  $(\text{Bi}_2\text{Ti}_3\text{O}_{10})^{2+}$  layers alternating with  $(\text{Bi}_2\text{O}_2)^{2-}$  layers perpendicular to the c-axis [5]. It has high Curie temperature ( $675^\circ\text{C}$ ), a good mechanical properties, environmental friendly lead-free composition, low dielectric dissipation and a relatively high dielectric constant  $\epsilon \approx 200$  [6]. Recently, lead-free piezoelectric ceramics have attracted considerable attention due to environmental concerns, and BiT is considerable to be a good material for high temperature piezoelectric applications, memory storages and optical display devices [7-10].

In this work, we fabricated 3D-shaped BiT by a two-step assembly method, using hybrid-sol-gel chemistry and FDM technique, with the aim of developing 3D-BiT object with complex shape.

### 4.3 Experimental

#### 4.3.1 Materials and procedures

The starting precursors used in this work included titanium isopropoxide (Sigma-Aldrich,  $\text{Ti}(\text{OCH}(\text{CH}_3)_2)_4$ ), N-methyl-diethanolamine (Sigma-Aldrich,  $\text{CH}_3\text{N}(\text{C}_2\text{H}_4\text{OH})_2$ ), ethanol (Sigma-Aldrich,  $\text{C}_2\text{H}_5\text{OH}$ ), distilled water ( $\text{H}_2\text{O}$ ), bismuth (III) oxide powders (Sigma-Aldrich,  $\text{Bi}_2\text{O}_3$ ) and polyvinylpyrrolidone (Sigma-Aldrich, PVP,  $M_w \approx 1,300,000$ ). All chemicals were analytical reagent grade and used without further purification

#### 4.3.2 Preparation of bismuth titanate ( $\text{Bi}_4\text{Ti}_3\text{O}_{12}$ ) via sol-gel technique

For BiT synthesis (Figure 4.1), 7.66 mL of  $\text{Ti}(\text{OCH}(\text{CH}_3)_2)_4$  was stabilized by 5.93 mL of  $\text{CH}_3\text{N}(\text{C}_2\text{H}_4\text{OH})_2$  under argon flow. The mixture was stirred for 10 min, then 0.51 mL of  $\text{C}_2\text{H}_5\text{OH}$  and 0.91 mL of distilled water were added drop-wise to the solution under magnetic stirring, respectively. The prepared solution was stirred vigorously for 10 min to achieve complete dissolution. Then, 8.86 g of  $\text{Bi}_2\text{O}_3$  (~10 wt. % excess  $\text{Bi}_2\text{O}_3$ ) was added to mixture solution and stirred continuously for 30 min at room temperature until a BiT yellow gel was obtained.

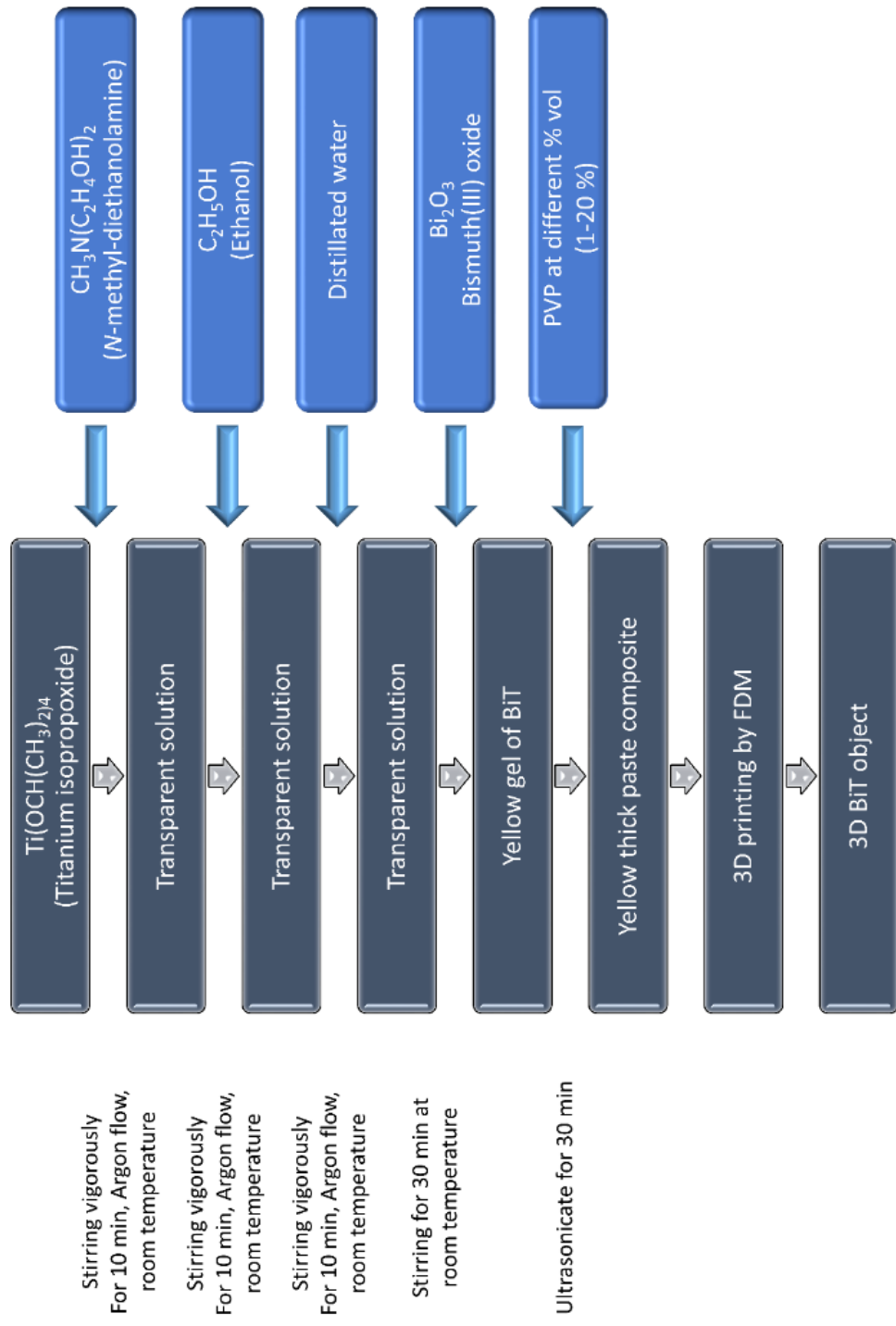


Figure 4.1 Schematic diagram of the synthesis of bismuth titanate ( $\text{Bi}_4\text{Ti}_3\text{O}_{12}$ ) via sol-gel technique

The phase identification was performed at room temperature using a monochromatic Cu-K $\alpha$  radiation X-ray diffractometer (XRD: Bruker D8 Robot Tools X-ray diffraction, Bruker, Germany). The XRD analysis was carried out ex-situ with a scan speed of 0.6° 2 $\theta$ /min at a 2 $\theta$  range of 20° to 60° of several calcined samples at 500, 600, 800, 850 °C for 1 h. The calcined powders (Bi<sub>4</sub>Ti<sub>3</sub>O<sub>12</sub>) at 500 °C were used for pellet fabrication by uniaxial hydraulic press. A horizontal assembly dilatometer (NETZSCH DIL 402C) was applied to determine the shrinkage behavior. The BiT pellet was heated in chamber furnace in static air environment with temperature program; ramp up heating rate of 1°C/min from 25°C to 850°C and holding at 850°C for 2 h and ramp down with cooling rate of 5°C/min from 850°C to 25°C.

#### **4.3.3 Fabrication of three-dimensional bismuth titanate (Bi<sub>4</sub>Ti<sub>3</sub>O<sub>12</sub>) by FDM technique**

3D-bismuth titanate (3D-BiT) was fabricated by a FDM technique (Figure 4.1). First, 20 mL of BiT gel was mixed with various volume percentage of PVP from 1.0 to 20 vol. %. The mixture was then stirred at room temperature with constant stirring for 30 min until homogeneous thick paste was obtained. The resulting thick paste was subjected to ultrasonic agitation at a frequency of about 24 kHz for 30 min. The whole mass was transferred to an extrusion syringe with a fixed nozzle diameter of 1.4 mm and then was printed by 3D printer (Zmorph 2.0S, ZMorph Sp. z o.o., Poland).

The rheology characteristics of bismuth titanate (Bi<sub>4</sub>Ti<sub>3</sub>O<sub>12</sub>) thick paste with different volume percentage of PVP were evaluated before printing by a rotational rheometer (MCR viscometer 302, Anton Paar, Austria) in order to find the suitable printing condition.

The thick paste materials were characterized in rotational mode with controlled temperature of 21 °C. All the experiments were performed using a cone-parallel spindle of 25 mm in diameter and 4° angle (CP25-4).

For non-Newtonian fluids, the relation between wall shear rate ( $\dot{\gamma}_w$ ) and extrusion printing speed ( $v$ ) can be obtained by the Rabinowitsch relation [11]:

$$\dot{\gamma}_w = \frac{(3n+1)}{4n} \left( \frac{4Q}{\pi R^3} \right) \quad (4.1)$$

where  $R$  is the capillary radius of nozzle (mm),  $Q$  is the volumetric flow rate through the capillary nozzle ( $\text{mm}^3/\text{s}$ ), and  $n$  is a constant equal to the power-law index.

The extrusion printing speed ( $v$ ) could be obtained by substituting  $Q = \pi R^2 v$  in equation (4.1):

$$\dot{\gamma}_w = \frac{(3n+1)}{4n} \left( \frac{8v}{D} \right) \quad (4.2)$$

where  $v$  is the extrusion printing speed (mm/s) and  $D$  is diameter of capillary nozzle (mm).

## 4.4 Results and discussion

### 4.4.1 Phase composition of $\text{Bi}_4\text{Ti}_3\text{O}_{12}$ (BiT)

To understand the crystallization behavior of  $\text{Bi}_4\text{Ti}_3\text{O}_{12}$ , the milled gel powders were calcined in air at temperature ranging from 500-900°C for 1 h. Figure 4.2 shows the XRD patterns of the calcined powders at different temperatures. The calcined powders at 500°C appear yellow in color and exhibit the presence of  $\text{Bi}_2\text{O}_3$  phase in XRD pattern. The powders calcined at 600°C become white in color, whereas XRD pattern shows the onset crystalline nature of BiT in agreement with earlier literatures [12, 13]. It is known that BiT has a ferroelectric Curie temperature of 675°C; below this temperature, the crystal belongs to a pseudo-tetragonal phase, and above this temperature, it is transformed into a pseudo-orthorhombic phase. This could be confirmed by the splitting profile peaks around  $2\theta$  of 33° of the powders calcined at 800°C and 850°C, suggesting that at this calcination temperature, these crystals have a pseudo-orthorhombic phase [12, 13]. The XRD pattern of the calcined sample at 850°C shows well-defined BiT crystalline structure and there is no signal of  $\text{Bi}_2\text{O}_3$  crystalline phase. The line width was decreased and intensity of diffraction line was increased, indicating the particles were agglomerated, fused together and some grain growth occurred. The structural parameters of the BiT

calcined sample at 850 °C were  $a = 5.41 \text{ \AA}$ ,  $b = 5.45 \text{ \AA}$ , and  $c = 32.84 \text{ \AA}$  which these parameters are comparable with the values given in JCPDS File no. 72-1019 [14].

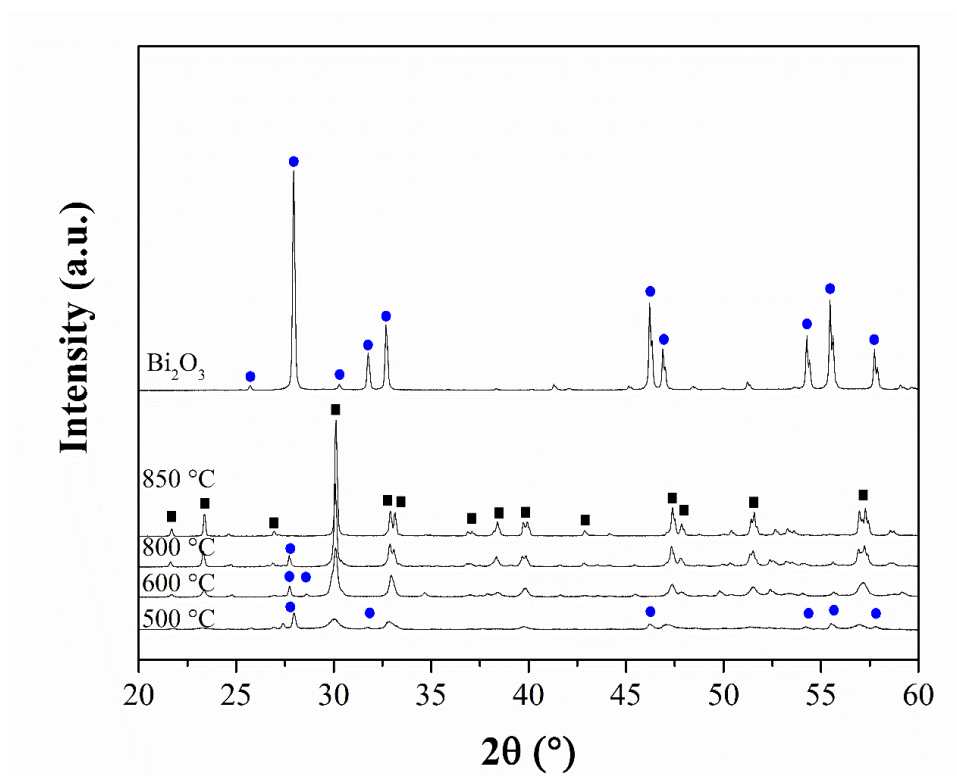


Figure 4.2 XRD patterns of  $\text{Bi}_4\text{Ti}_3\text{O}_{12}$  powders prepared from the sol-gel method after calcination at different temperatures.

Figure 4.3 presents the dilatometry plot of the calcination of BiT pellet at 500°C. The curve predicts that there is no shrinkage on heating up to a temperature of 600°C. However, between 25°C and 600°C, there is some small expansion of 0.1 % in the BiT pellet, probably due to the reaction of some intermediate chemical and/or the arrangement within the crystal lattice. The shrinkage started from 600°C while a great shrinkage can be observed after heating between 700°C and 800°C. The overall dimension change was around 14% reduction from the original length. These results were in good agreement with previous work [15]. Based on dilatometry results, the suitable sintering temperature of BiT was selected at 850°C.

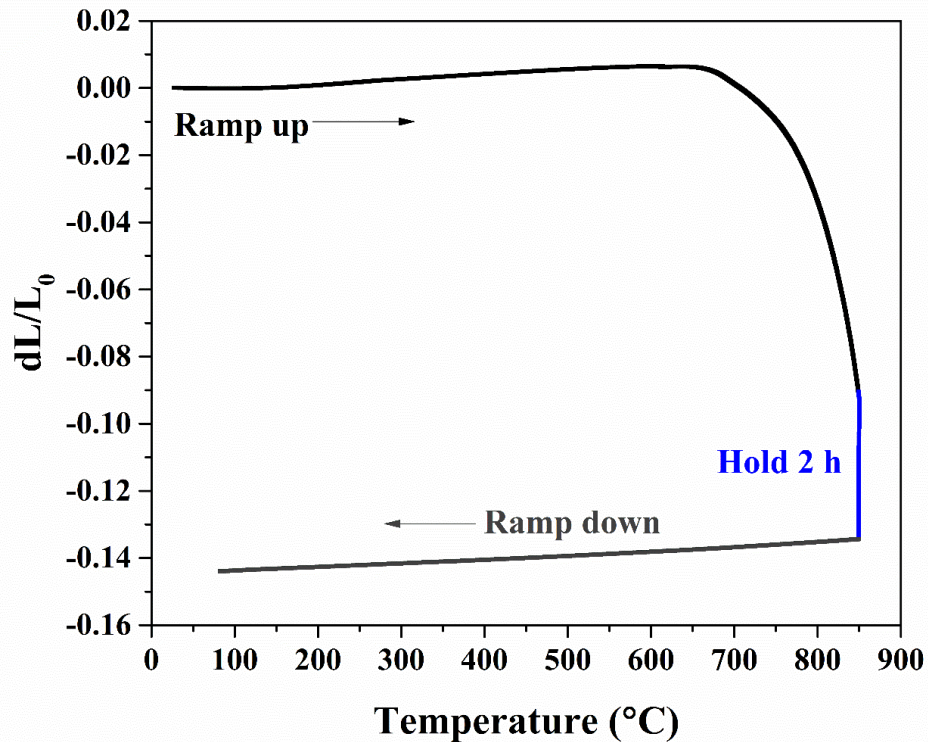


Figure 4.3 Linear shrinkage curve of calcined BiT from room temperature to 850°C.

#### 4.4.2 Rheology of BiT compounds

The rheological properties of the BiT thick paste materials with different content of PVP were then investigated to optimize the printing condition. As presented in Figure 4.4(a), at higher vol % of PVP, the viscosity profiles are shifted to higher values of viscosity. This is due to the presence of high molecular weight of PVP ( $M_w \approx 1,300,000$ ) which give resistance to the flowing behavior under applied shear stress [16, 17].

Besides nozzle diameter and viscosity of material, shear thinning behavior facilitates continuous flow through fine nozzles without clogging. Generally, this behavior is quantitatively estimated by evaluating the flow indexes ( $n$ ). Figure 4.4(b) shows the double logarithmic plot for the BiT composites; the slope of the straight line corresponds to the flow index ( $n$ ) that can be used to identify the flowing mechanism of a system [18-21]. As shown in Table 4.1, all samples exhibit shear-thinning behavior ( $n < 1$ ), lower  $n$  value indicating more-shear thinning activities. The

increase in flow index ( $n$ ) was observed with increasing content of PVP from 1.0 vol % to 7.5 vol. % and the flow index ( $n$ ) then decreased slightly as the PVP content was exceeded 7.5 vol.%.

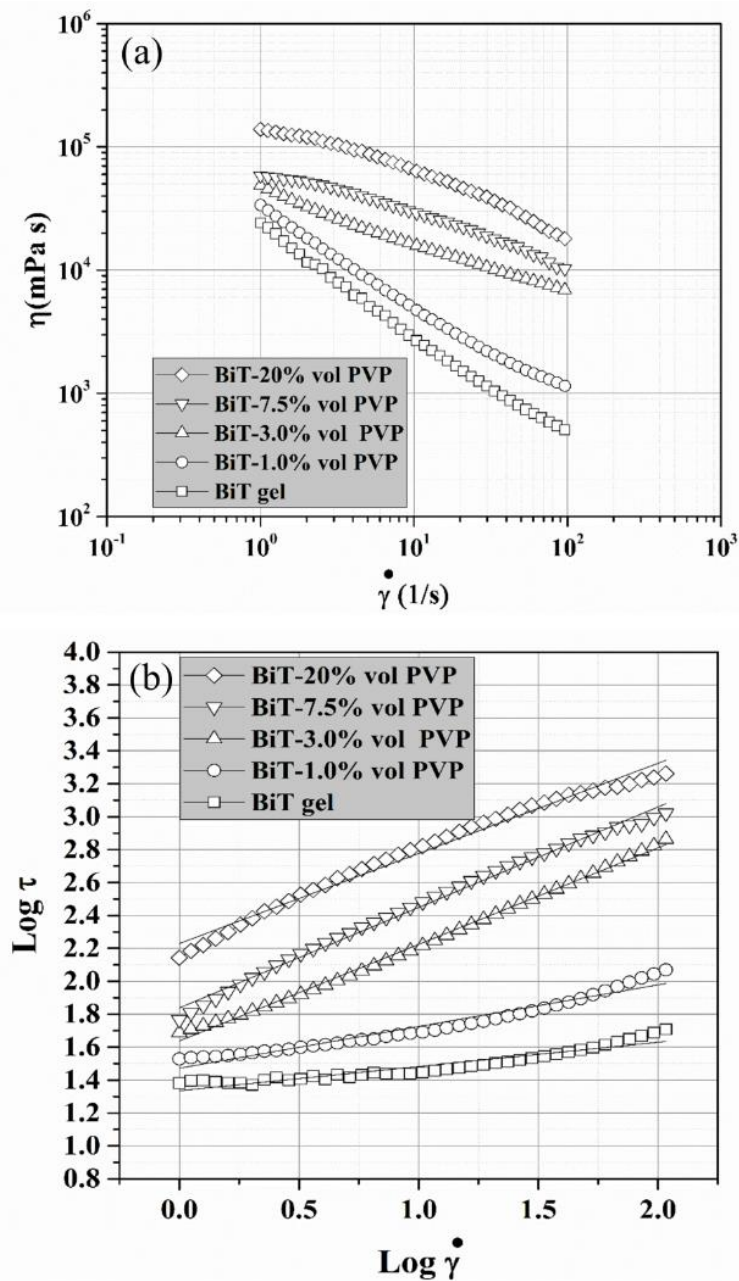


Figure 4.4 (a) Viscosity plot and (b) the corresponding double logarithmic power law plot for the complete series of BiT showing the flow index (slope).

Table 4.1 The flow indexes for the BiT gel composites.

<b>Samples</b>	<b>Flow index (<i>n</i>)</b>
BiT gel	0.15
BiT-1.0% vol. PVP	0.25
BiT-3.0% vol. PVP	0.59
BiT-7.5% vol. PVP	0.61
BiT-20% vol. PVP	0.55

Typically, the processing shear rate of extrusion process is in the range of 1-100 s<sup>-1</sup> [22]. The extrusion printing speed (*v*) is calculated from equation (4.2), at 3.0 vol. % of PVP, the extrusion printing speed could be expanded from 1 to 15 mm/s (Figure 4.5(a)). Above 3.0 vol. % of PVP, there is no significant effect of further adding PVP. Upon the addition of PVP, the processing speed is expanded by 53 % PVP molecule acted as processing aid which could reduce the wall shear rate ( $\dot{\gamma}_w$ ) corresponding to the ability of printing at higher extrusion speed. Based on rheology results, the BiT with 3.0 vol. % of PVP was selected for fabricating 3D object by FDM technique.

Figure 4.5(b) shows 3D-BiT object fabricated by extrusion-based FDM technique. By this technique, we could produce the printed object as complex shape with high precision in shape and dimension.

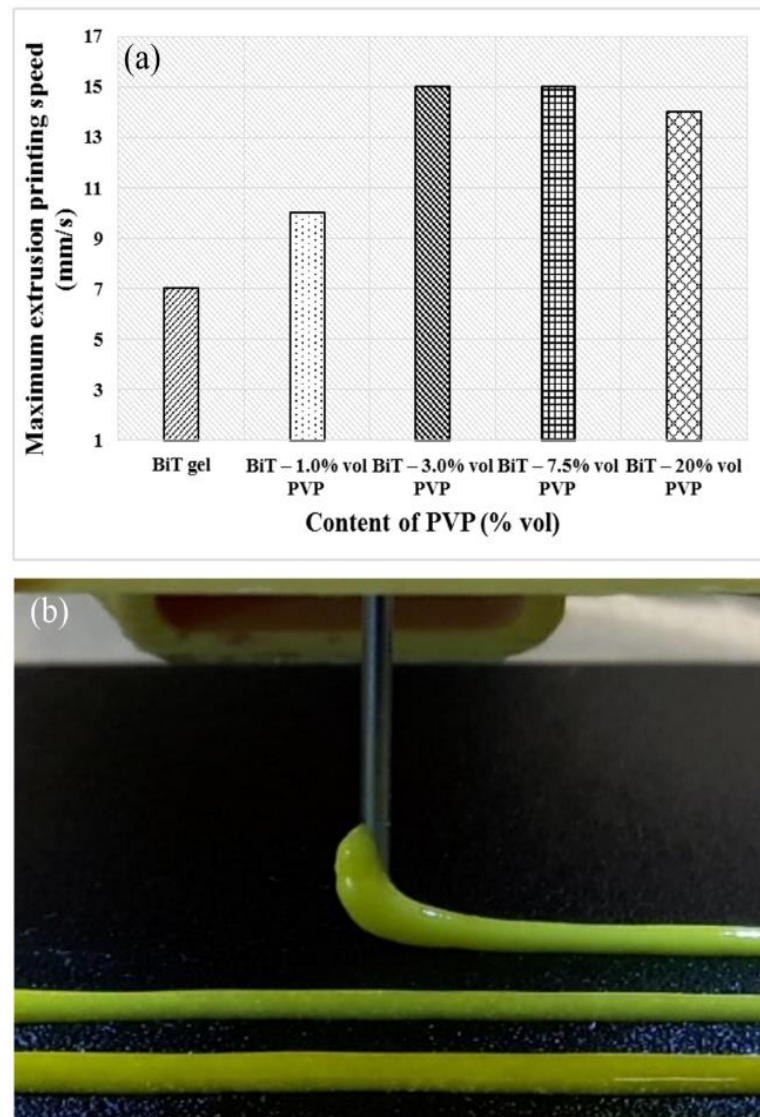


Figure 4.5 (a) Processing window for BiT gel and its composite for 1.4 mm of extrusion nozzle and (b) Extrusion based FDM technique for BiT at 3.0 % vol of PVP (3D-BiT).

#### 4.5 Conclusions

In conclusion, the 3D bismuth titanate (3D-BiT) was successfully fabricated by two step assembly method, sol-gel followed by extrusion-based fuse deposition modeling (FDM) technique. BiT phase compositions, densification behavior and rheology of printing materials were investigated. Upon the adding 3.0

vol. % of PVP, the ability to enlarge the extrusion printing speed of the thick paste materials was over 50 %, compared to pure gel BiT.

#### 4.6 References

1. Zhao, H.P., Ye, C.S. and Fan, Z.T., 3D printing of calcia-based ceramic core composites. *Advances in Science and Technology*, 2014. **88**(88): p.65-69.
2. Kim, K., et al., 3D Optical Printing of Piezoelectric Nanoparticle–Polymer Composite Materials. *ACS Nano*, 2014. **8**(10): p. 9799-9806.
3. Sun, K., et al., 3D printing of interdigitated Li-Ion microbattery architectures. *Advanced Materials*, 2013. **25**(33): p.4539-4543
4. Castles, F., et al., Microwave dielectric characterisation of 3D-printed BaTiO<sub>3</sub>/ABS polymer composites. *Scientific reports*, 2016. **6**: p. 22714.
5. Aurivillius, B., Mixed bismuth oxides with layer lattices. *Arkiv for kemi*, 1950. **1**(6): p. 499-512.
6. Macedo, Z.S., Ferrari, C.R. and Hernandez, A.C., Impedance spectroscopy of Bi<sub>4</sub>Ti<sub>3</sub>O<sub>12</sub> ceramic produced by self-propagating high-temperature synthesis technique. *Journal of the European Ceramic Society*, 2004. **24**(9): p. 2567-2574.
7. Takenaka, T. and Sakata, K., Grain orientation and electrical properties of hot-forged Bi<sub>4</sub>Ti<sub>3</sub>O<sub>12</sub> ceramics. *Japanese Journal of Applied Physics*, 1980. **19**(1): p. 31.
8. Yang, Q., et al., Bi<sub>4</sub>Ti<sub>3</sub>O<sub>12</sub> nanoparticles prepared by hydrothermal synthesis. *Journal of the European Ceramic Society*, 2003. **23**(1): p. 161-166.
9. Yao, Y.Y., et al., Doping effect on the dielectric property in bismuth titanate. *Journal of Applied Physics*, 2004. **95**(6): p. 3126-3130.
10. Noguchi, Y., et al., Defect Control for Large Remanent Polarization in Bismuth Titanate Ferroelectrics-Doping Effect of Higher-Valent Cations. *Japanese Journal of Applied Physics*, 2000. **39**(12B): p. L1259.
11. Collyer, A.A. (1993). **Techniques in rheological measurement**. London: Chapman & Hall

12. Zhang, F., Karaki, T. and Adachi, M., Coprecipitation synthesis of nanosized  $\text{Bi}_4\text{Ti}_3\text{O}_{12}$  particles. *Japanese Journal of Applied Physics*, 2006. **45**(9S): p. 7385-7388.
13. Pookmanee, P. and Phanichphant, S., Characterization of bismuth titanate powders. *Advanced Materials Research*, 2007. **26**: p. 247-250.
14. Phases, I., (1988). **JCPDS International Centre for Diffraction Data**. Swarthmore, PA.
15. Naz, S., et al., Nanosized bismuth titanate ( $\text{Bi}_4\text{Ti}_3\text{O}_{12}$ ) system drive through auto-combustion process by using suspension titania ( $\text{TiO}_2$ ). *Journal of Thermal Analysis and Calorimetry*, 2013. **114**(2): p. 719-723.
16. Wu, D., et al., Rheology of carbon nanotubes-filled poly (vinylidene fluoride) composites. *Industrial & Engineering Chemistry Research*, 2012. **51**(19): p. 6705-6713.
17. Vidhate, S., et al., Crystallization, mechanical, and rheological behavior of polyvinylidene fluoride/carbon nanofiber composites. *Journal of applied polymer science*, 2009. **112**(1): p. 254-260.
18. Marani, D., Hjelm, J. and Wandel, M., Rheological analysis of stabilized cerium-gadolinium oxide (CGO) dispersions. *European Ceramic Society Journal*, 2014. **34**(3): p. 695-702.
19. Marani, D., et al., Colloidal stabilization of cerium-gadolinium oxide (CGO) suspensions via rheology. *Journal of the European Ceramic Society*, 2015. **35**(10): p. 2823-2832.
20. Marani, D., et al., Poly (vinylpyrrolidone) as dispersing agent for cerium-gadolinium oxide (CGO) suspensions. *Journal of materials science*, 2016. **51**(2): p.1098-1106
21. Marani, D., et al., Enhanced densification of thin tape cast Ceria-Gadolinium Oxide (CGO) layers by rheological optimization of slurries. *Ceramics International*, 2017. **43**(7): p. 5647-5653.
22. Sabic Global. **Innovative Plastics High & Low Shear Rate Rheology**, Accessed on July 11, 2017. Available from: [http://www.pod-sabic.com/KBAM/Reflection/Assets/Thumbnail/10606\\_4.pdf](http://www.pod-sabic.com/KBAM/Reflection/Assets/Thumbnail/10606_4.pdf), 2013.

## Chapter 5

### 3D Printed Barium Titanate/poly(vinylidene fluoride) Nano-hybrid with Anisotropic Dielectric Properties

#### 5.1 Abstract

Electrospun BaTiO<sub>3</sub> nanofibers (BTNFs) were synthesized and blended in poly(vinylidene fluoride) (PVDF) matrix to obtain a flexible nano-hybrid composite with high dielectric constant (flexible high-k). The blending was made with different BTNFs contents (0.6, 4.5, 20 vol.%). The rheological properties of the starting materials were optimized to shape the hybrid by precision-extrusion-based fuse deposition modeling technique. The 3D printed BTNFs allowed complex shapes with different degrees of fiber alignment as the result of printing shear stress and the chemical composition of the starting material. The dielectric properties of the nano-hybrid were controlled by anisotropy with an enhancement in nanofibers cross direction ( $\perp$ ), where dielectric constant  $k^{\perp}$  at 1 kHz was increased to ca. 200 from 13 of the PVDF matrix.

#### 5.2 Introduction

Ferroelectric ceramic-polymer nanohybrid materials play a crucial role in flexible electronics and in energy technologies (e.g. capacitors, sensors and transducers), due to their merits of enabling the tailoring of specific dielectric, thermal, and mechanical properties and an easy processing [1-4]. By integrating the advantages of two phases, nanohybrid materials can offer enhanced performances with respect to those of the individual components [5]. The performance of this kind of material generally depends both on the individual properties of the two components, and on the nature and extension of the hybrid interface [6, 7]. This latter feature can easily be modulated by varying the mixing length scale and the nature of the polymer-ceramic interactions. Indeed, the larger the interfacial phase, the greater the influence of the ceramic component on the original characteristics of the PVDF [7]. This confers tuneable properties that make hybrid materials highly appealing for a

wide range of applications [7]. Yet, the unlimited possibilities deriving from this approach paves the way to advanced new materials with unique properties [7].

Owing to high dielectric constant ( $k$ ), high mechanical strength, excellent chemical stability, non-toxicity, and easy processability, the electroactive poly(vinylidene fluoride) (PVDF) is the most used as polymer in dielectric materials field [8, 9]. Concerning the ceramic component, among others barium titanate ( $\text{BaTiO}_3$ : BT), a lead-free high- $k$  ferroelectric ceramic material with a perovskite structure, is used in many applications due to its attractive piezoelectric and dielectric properties [10, 11].

Given their exceptional properties and non-toxicity, hybrid systems based on PVDF-BT combination have been largely investigated as dielectric materials [12-13]. Nanostructured functional fillers with high aspect ratio (e.g. one-dimensional, 1D) have been widely used with the aim of increasing the hybrid interface [14-20]. A significant effect on the dielectric properties of PVDF has been obtained [13-16]. Among others, nanofibers, prepared via electrospinning, offer the further advantage of an easy control over the morphology and the compositional features [18-20].

Several shaping methods have been traditionally used to process hybrid systems into thin film [21-23]. Currently, there is significant development in three dimensional (3D) assembling technology, namely 3D printing. One of the most interesting 3D printing techniques is computer-controlled fabrication via solid freeform, also known as fuse deposition modelling (FDM). This technique produces objects with controlled complex shapes and reduced size with short processing times, with relatively low cost equipment [24]. Recently, Castles et al. [25] has demonstrated  $\text{BaTiO}_3$  powder/ABS polymer dielectric composites by FDM. They obtained a dielectric constant value for the material at 20 % vol. of BT of 6.24, which matched those of bulk unprinted materials. Sun et al. prepared lithium ion micro-batteries by FDM [26] that exhibited high energy and power density. Furthermore, when anisotropic fillers are used, their orientation within the polymeric matrix is an additional parameter that has been demonstrated to significantly enhance the performances of the BTNFs/PVDF-based systems [27].

In the present work, we proposed a novel approach for preparing anisotropic BTNFs/PVDF 3D-nanohybrid dielectric materials. The nanohybrids were

designed and fabricated by FDM, where the nanofibers were embedded and aligned in the PVDF matrix by tunable internal friction during the extrusion. We especially analyzed phase compositions and properties in the hybrid as results of the rheological properties by varying the BTNFs loading and the extrusion forces that lead to fibers alignment during the 3D printing. The overall aim was thus to tune the dielectric properties in the 3D range by creating a “3D-printed” anisotropy in the BTNFs/PVDF hybrid material. This consists in combining short-range orientation of the nano-fibers, at the microstructural level, with long-range directionality in the complex shape by 3D printing technique.

### 5.3 Experimental

#### 5.3.1 Materials

The starting precursors used in this work included barium acetate (Sigma-Aldrich,  $\text{Ba}(\text{CH}_3\text{COO})_2$ ), acetic acid (Sigma-Aldrich,  $\text{CH}_3\text{COOH}$ ), titanium isopropoxide (Sigma-Aldrich,  $\text{Ti}(\text{OCH}(\text{CH}_3)_2)_4$ ), polyvinylpyrrolidone (Sigma-Aldrich, PVP ( $M_w \approx 1,300,000$ )), ethanol (Sigma-Aldrich,  $\text{C}_2\text{H}_5\text{OH}$ ), and *N*-Methyl-2-pyrrolidone (Sigma-Aldrich, NMP,  $\text{C}_5\text{H}_9\text{NO}$ ). All chemicals were analytical reagent grade and used without further purification.

#### 5.3.2 Electrospun of $\text{BaTiO}_3$ nanofibers (BTNFs)

For the BTNF synthesis [28], 1.275 g of  $\text{Ba}(\text{CH}_3\text{COO})_2$  was dissolved in 3 mL of  $\text{CH}_3\text{COOH}$  for 2 h at room temperature, under argon flow. Then, 1.475 mL of  $\text{Ti}(\text{OCH}(\text{CH}_3)_2)_4$  was added dropwise into the solution under magnetic stirring. The precursor mixture was stirred for 2 h to achieve complete dissolution and mixing. A solution of 0.2 g of PVP dissolved in 3 mL of  $\text{C}_2\text{H}_5\text{OH}$  was added to the ceramic precursor. The precursor mixture was loaded into a plastic syringe equipped with a metallic needle tip. Then, 15 kV was applied to the precursor and the distance between tip-end and collector was fixed at 9.0 cm. All electrospinning experiments were carried out by electrospinning machine (RT Advanced, Linari engineering, Italy) at room temperature. The as-synthesized fibers were dried in a fume-hood at room temperature for 24 h to remove the humidity.

In order to obtain crystallized BT nanofibers (BTNFs), the calcination temperature for the electrospun fibers was evaluated with the aid of TG/DTA (Netzsch STA 409C/CD, Germany) and an XRD (XRD: Bruker D8 Robot Tools X-ray diffraction, Bruker, Germany). The TG/DTA analysis was performed in air flux from room temperature to 850 °C at a heating rate of 1°C/min.

The XRD analysis was carried out ex-situ with a scan speed of 0.6° 2 $\theta$ /min at a 2 $\theta$  range of 20° to 80° on samples calcined at 400, 500, 600, 700 and 800 °C for 1 h. The diameter and the morphology of the crystalline fibers were evaluated with a field emission gun scanning electron microscope (ZEISS Merlin, Carl Zeiss Microscopy GmbH, Germany) at an accelerating voltage of 10 kV with In-lens and SE1 electron detector.

### **5.3.3 Preparation of anisotropic BTNFs/PVDF 3D-nanohybrid dielectric materials**

Anisotropic BTNFs/PVDF 3D-nanohybrid dielectric materials were fabricated by FDM. The concentration of PVDF in NMP solution was fixed at 30% wt. to match with the viscosity range of thick paste material (20,000-70,000 mPa·s) for consumer grade 3D printer (Zmorph 2.0S, ZMorph Sp. z o.o., Poland). First, 30 g of PVDF was dissolved in 100 g of NMP. The solution was then stirred at a 50 °C with constant stirring for 2 h until homogeneous solution appeared. The loading of the BTNFs was varied from 0 (pure PVDF) to 20% vol. to cover the range of concentration allowed by printer used. Then, defined compositions of the BTNFs and the PVDF solution were stirred with constant rate. The resulting mixture was subjected to ultrasonic agitation at a frequency of about 24 kHz for 30 minutes. The resulting solution was transferred to an extrusion syringe with different nozzles of diameters 2.5 mm and 1.2 mm and then was printed by 3D printer. All samples were printed at room temperature without using hot bed.

The rheology characteristics of pure PVDF and BTNFs/PVDF nanohybrid materials before printing were evaluated by a rotational rheometer (MCR viscometer 302, Anton Paar, Austria). The solutions were characterized in rotational mode. A constant temperature of 21°C was maintained during the experiments using a temperature control unit. All the experiments were performed using a cone-parallel

spindle of 25 mm in diameter and 4° angle (CP25-4). To remove any effects due to the sampling and loadings, the measurements were performed using a pre-shear at 1 s<sup>-1</sup> for 1 minute followed by 1 minute at rest (0 s<sup>-1</sup> shear rate), and again at 1 s<sup>-1</sup> for 1 minute. The experiments were conducted in the shear rate of 1-100 s<sup>-1</sup> in up and down ramp.

The phase compositions were analyzed by XRD technique (XRD: Bruker D8 Robot Tools X-ray diffraction, Bruker, Germany). The XRD analysis was carried out with a scan speed of 0.6° 2θ/min at a 2θ range of 10° to 50°.

The surface morphology and fibers alignment of the 3D-nanohybrid materials were evaluated with a scanning electron microscope (TM3000 Tabletop Scanning Electron Microscope, Hitachi, Japan) at an accelerating voltage of 15 kV with a backscattered electron detector.

The degree of fiber orientation in three dimensions was evaluated by focused ion beam (FIB) SEM serial sectioning technique by simultaneously collecting In-Lens (on beam axis SE1) and SE2 (Everhart-Thornley) detector secondary electron (SE) images (Zeiss 1540 XB Crossbeam Scanning Electron Microscope, Carl Zeiss Microscopy GmbH, Germany). The reconstructed volume had dimensions of approximately 20 x 17 x 20 μm, with the longest axis perpendicular to the extrusion direction and parallel to the FIB slicing direction. The voxel dimensions were 39.5 nm in the SEM imaging plane with a slice thickness of 60.6 nm. The dual imaging mode raw data was global intensity gradient corrected, aligned and cropped [29, 30]. All image processing was performed using in-house image analysis code written in MATLAB. The BTNFs were segmented in 3D from the PVDF matrix using a combination of image intensity and intensity gradient in both the In-lens and SE2 image modes combined with visual inspection to achieve the optimum segmentation and minimize image artefacts due to the serial sectioning technique. The segmented BTNF phase was skeletonized using a parallel medial axis thinning approach [31, 32] to determine the centerlines of the individual fibres, which were then converted to a network graph of links and nodes to characterize the length and orientation of fibre fragments [33]. Principle component analysis (PCA) using inbuilt MATLAB functions was then performed on the 3D coordinates of the centerlines of the each

fibre fragment to determine the orientation of the longest axis of the coordinate voxel point cloud in terms of azimuthal and elevation angles relative to the extrusion direction.

### 5.3.4 Dielectric property measurement

Broadband dielectric measurements of both pure PVDF and BTNFs/PVDF 3D- nanohybrid dielectric materials for different % vol. of BTNFs were carried out by using Impedance/Gain-Phase Analyzer (Solartron 1260A, Solartron Analytical, UK). All measurements were carried out in air at room temperature, in the frequency range of 100 Hz to 1 MHz and applied biasing voltage of 0.2 V. The frequency dependence of dielectric constant ( $k$ ) at room temperature can be calculated from the following relation [34].

$$k = \frac{C_p * t}{A * \epsilon_0} \quad (5.1)$$

where,  $C_p$  is the capacitance of materials (F),  $t$  is the thickness of nanohybrid dielectric material (m),  $A$  is the area of electrode ( $m^2$ ) and  $\epsilon_0$  is vacuum permittivity having value  $8.854 * 10^{-12}$  F/m.

Dielectric properties were measured both the extrusion direction (parallel,  $k^{\parallel}$ ) and transverse direction (cross,  $k^{\perp}$ ).

### 5.3.5 Methods

The observed enhancement in the dielectric properties of the developed hybrids was discussed according to the effective medium theory (EMT) and rule of mixture (ROM) models.

EMT model, developed by Rao et al [35], enables the estimation of the dielectric properties of composite systems by including the effect of the morphology and size of the ceramic fillers. The model is described by the following equation:

$$\epsilon = \epsilon_m \left[ 1 + \frac{f(\epsilon_f - \epsilon_m)}{\epsilon_m + n(1-f)(\epsilon_f - \epsilon_m)} \right] \quad (5.2)$$

where  $n$  is the shape-dependent parameter,  $f$  is the volume fractions of the ceramic fillers,  $\epsilon$ ,  $\epsilon_f$  and  $\epsilon_m$  represent the dielectric constant of the nanocomposites, ceramic and polymer matrix, respectively.

The ROM model instead includes in the estimation the shape fillers. The dielectric constant are estimated from the following relation [36].

$$\epsilon_{\text{mix}} = \epsilon_m + \left[ \frac{(\epsilon_i - \epsilon_m)(\epsilon_i + 5\epsilon_m)}{3(\epsilon_i + \epsilon_m)} \right] V_i \quad (5.3)$$

where,  $\epsilon_{\text{mix}}$ ,  $\epsilon_i$ ,  $\epsilon_m$  are the dielectric constants of a composite, ceramic filler material, and matrix material, respectively.  $V_i$  is the volume fraction of ceramic fillers.

#### 5.4 Results and discussion

For the formation of the BTNFs, crystallization and microstructures are controlled by the sol-gel chemistry, the electrospinning and the calcination conditions. For the chemistry and the electrospinning conditions, previous work by Junhan et al. were used as a reference, while degree of crystallinity can be modulated by the calcination thermal treatment [28]. To optimize the heat-treatment process, the TG/DTA analysis was carried out on the as-synthesized fibers. The thermal decomposition behaviour of as-synthesized fibers is shown in Figure 5.1. About 10 % weight loss from 80-150 °C was related to the evaporation of residual solvent. The weight loss between 150 °C and 330 °C and a sharp exothermic peak at 280 °C were correlated to the decomposition of organic precursors [24, 37]. The weight loss (about 7%) and the corresponding broad exothermic peak observed between 380 °C and 550 °C, are consistent with the decomposition of organic groups from the organometallic precursor and its intermediate phases, BaCO<sub>3</sub> [38]. The weight loss between 570 °C and 700 °C is indicative of the onset in crystallization of BT nanofibers. The TG/DTA results reveal about 50% weight loss that was observed with no further weight loss at temperatures > 700 °C. Accordingly, the synthesized fibers were completely crystallized and intermediate phases were removed at temperature over 700 °C [38, 39].

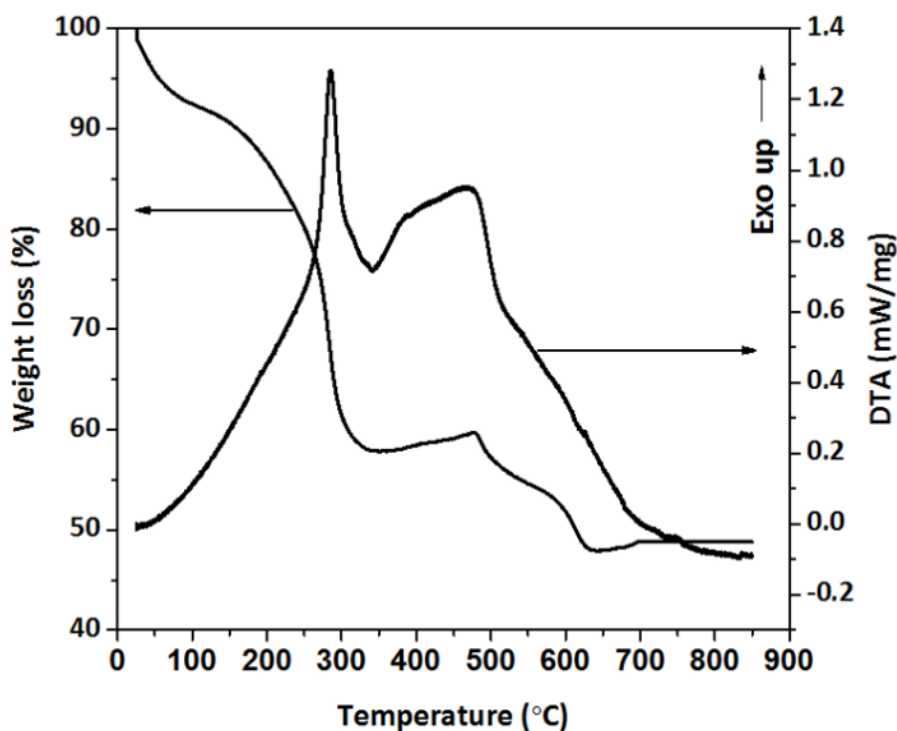


Figure 5.1 TG/DTA profiles of the as synthesized fibers.

The XRD patterns of the as synthesized and calcined fibers at temperatures between 400 °C and 800 °C are presented in Figure 5.2. The as-synthesized fibers were amorphous consisting in un-oriented structure [28, 39-41]. Two peaks were observed at  $2\theta$  around  $27^\circ$  and  $43^\circ$  of for samples treated at 500 °C and 600 °C, which are consistent with  $\text{BaTi}_2\text{O}_4$  and  $\text{BaCO}_3$  [24]. The calcined sample at 600 °C exhibited the onset of BT perovskite crystallization together with the non-perovskite peaks of an intermediate phase,  $\text{BaCO}_3$  [28, 40]. Well defined perovskite  $\text{BaTiO}_3$  patterns were instead observed for samples treated at 700 °C, the disappearance of the non-perovskite peaks is indicative of the decomposition of  $\text{BaCO}_3$ . At 800 °C, the perovskite peaks pattern became marked, due to the complete reaction of the BT formation.

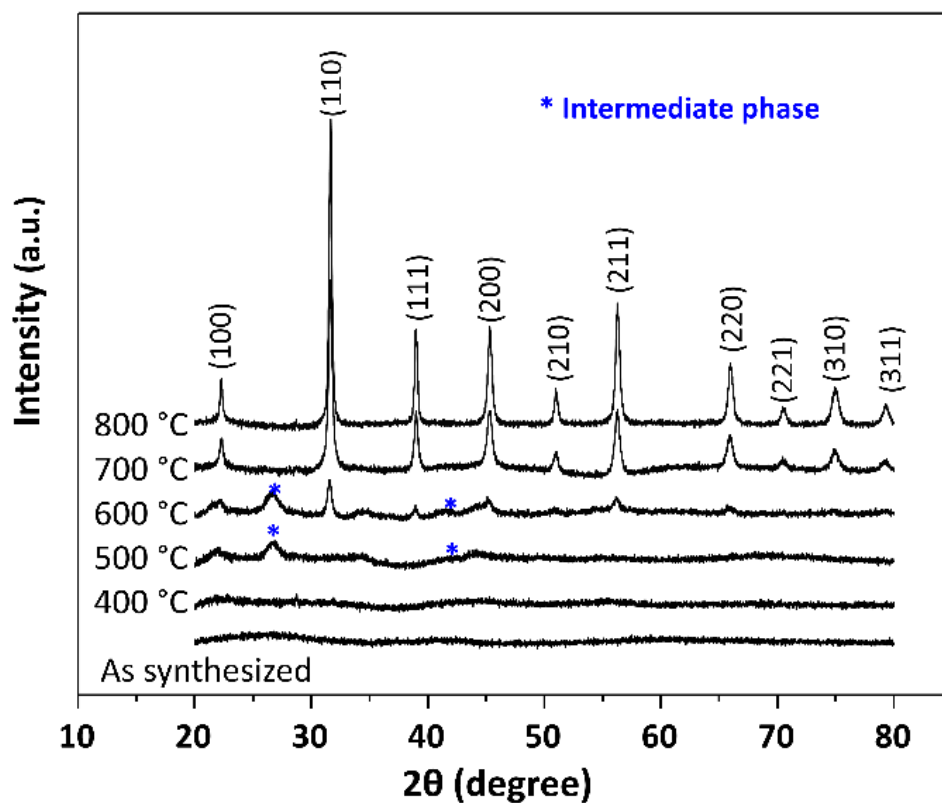


Figure 5.2 X-ray diffraction patterns of the as synthesized fibers and calcined BTNFs for 1 h at different temperatures.

The morphologies of the as-synthesized and calcined fibers were then investigated. Figure 5.3 shows the morphologies of the as synthesized fibers and BTNFs after calcination at 800 °C. The as synthesized nanofibers (Figure 5.3(a) and 5.3(b)) exhibit smooth and uniform surfaces with a random fibers orientation, whereas a polycrystalline surface is observed for the nanofibers calcined at 800 °C (Figure 5.3(c)). The crystalline nanofibers are fragile and break easily in agreement with literature [41-44].

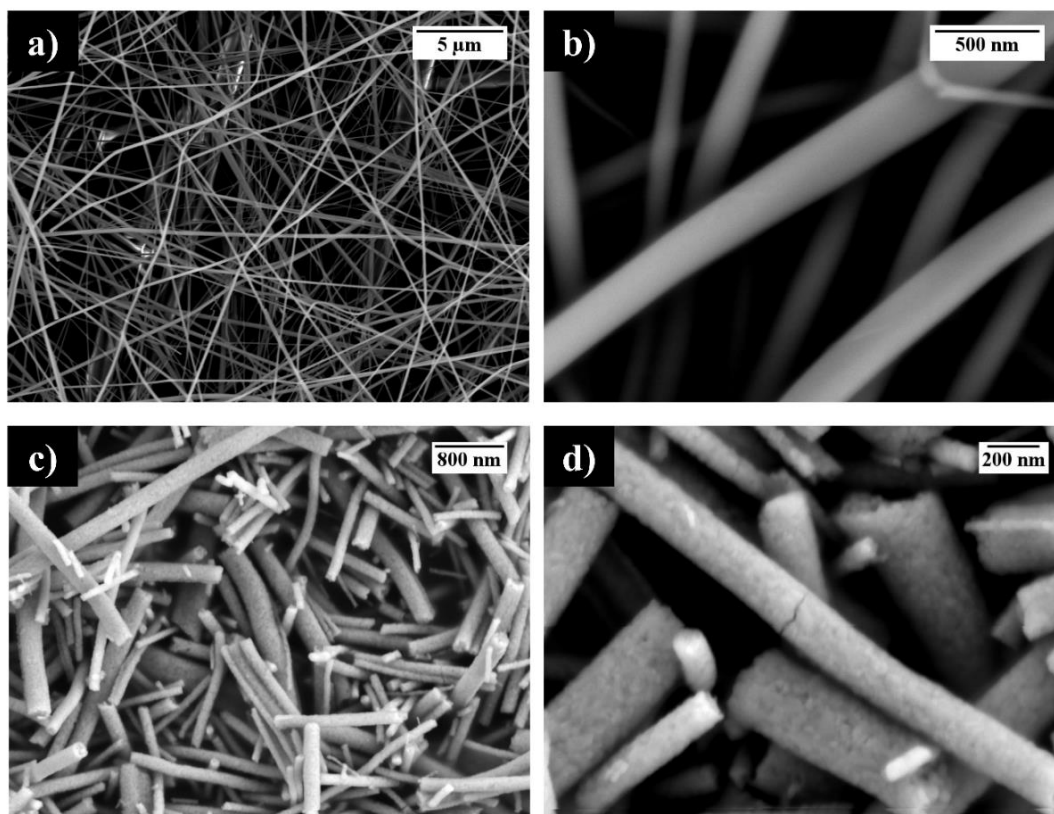


Figure 5.3 FE-SEM In-lens SEI images of (a), (b) as synthesized fibers and (c), (d) BTNFs calcined at 800 °C for 1 h.

The nanofiber diameter is observed to decrease from 800 nm to 200 nm after calcination due to decomposition of the organic components and the crystallization of the phase of interest [28, 45]. Upon the calcination process, the diameter is reduced by 75%.

There have been no previous reports on the preparing of PVDF composites using consumer 3D printer with different nozzle diameter. X-ray diffraction (XRD) pattern was then used to investigate the change in crystallinity of 3D printed from 2.5 mm and 1.2 mm. of nozzle diameter due to the addition of BTNFs in the PVDF matrix. The XRD pattern of pure PVDF in Figure 5.4 shows three main characteristic peaks, a sharp peak at 20.01 correspond to the  $\beta$ -phase (110) crystal with a fully stretched all-trans planar zigzag conformation and indicating the

semi-crystalline nature of PVDF [34, 46-49]. Furthermore, the peaks at 18.41 and 39.21 which are assigned to  $\alpha$ -phase characteristic of PVDF were observed [47-49]. In XRD pattern of BTNFs/PVDF nano-hybrids crystalline peaks, corresponding to reflection planes of at (100), (110), (111) and (200) of the perovskite BT, structure are also identified. Interestingly, at increasing amount of BTNFs from 0.6% vol. to 4.5% vol., the peak intensity of  $\alpha$  and  $\beta$  crystalline increases with respect to the pure PVDF, indicating that the addition of small amount of BTNFs can promote a more regular arrangement for PVDF, the added BTNFs act as nuclei for PVDF crystallization. When the loading of 20% vol. is reached, the intensity of  $\alpha$  and  $\beta$  characteristic peaks decreased, especially  $\alpha$  characteristic peak at 39.21. At this content of BTNFs, the  $\beta$  phase is dominant.

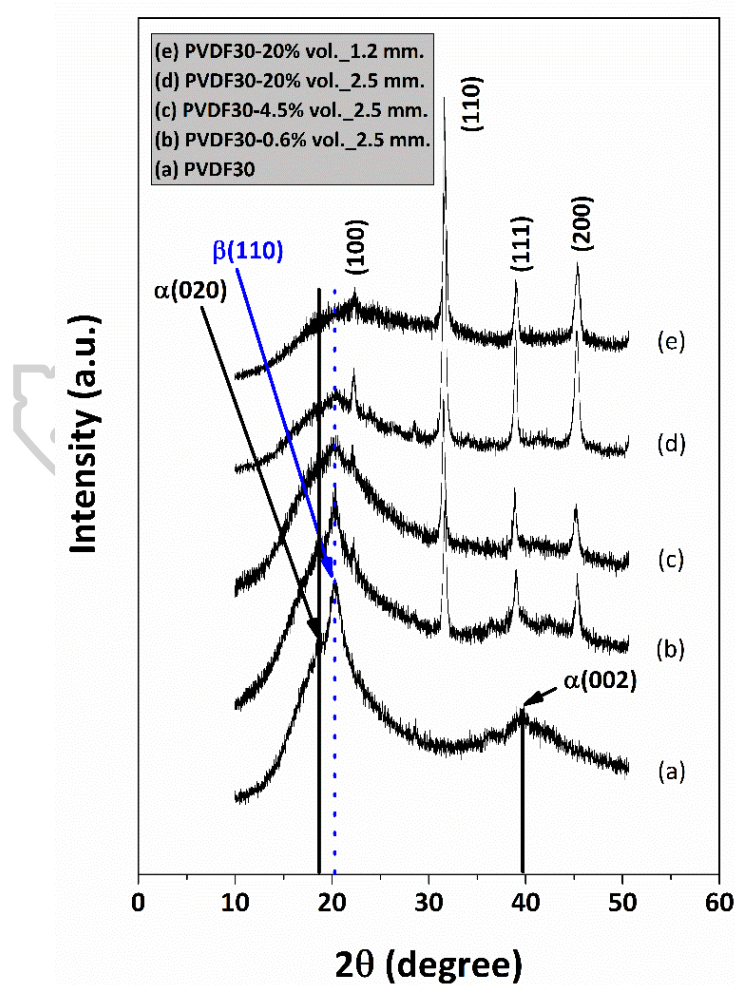


Figure 5.4 X-ray diffraction patterns of the BTNFs/PVDF 3D-nanohybrid materials at different % vol. of BTNFs.

The adding of a large amount of BTNFs might destruct the molecular regularity of PVDF chain [47]. In addition, there is no significant difference in the intensity of  $\beta$ -phase of obtained hybrids from 2.5 mm. and 1.2 mm. of nozzle diameter (line (4d) and (4e)), respectively, indicating that the nozzle diameter has no effect on  $\beta$  phase crystallinity of PVDF hybrids.

For the FDM technique, the maximum solid loading of the filler in the polymer matrix that enables printing is  $\sim 50\%$  wt [25, 26, 50]. Indeed, at high content of filler, the shear stress at nozzle extruder is high, resulting in the unstable flow at extrusion nozzle [50]. In this work, we used a consumer grade 3D printer (Zmorph 2.0S) to fabricate 3D printed dielectric materials as shown in Figure 5.5.

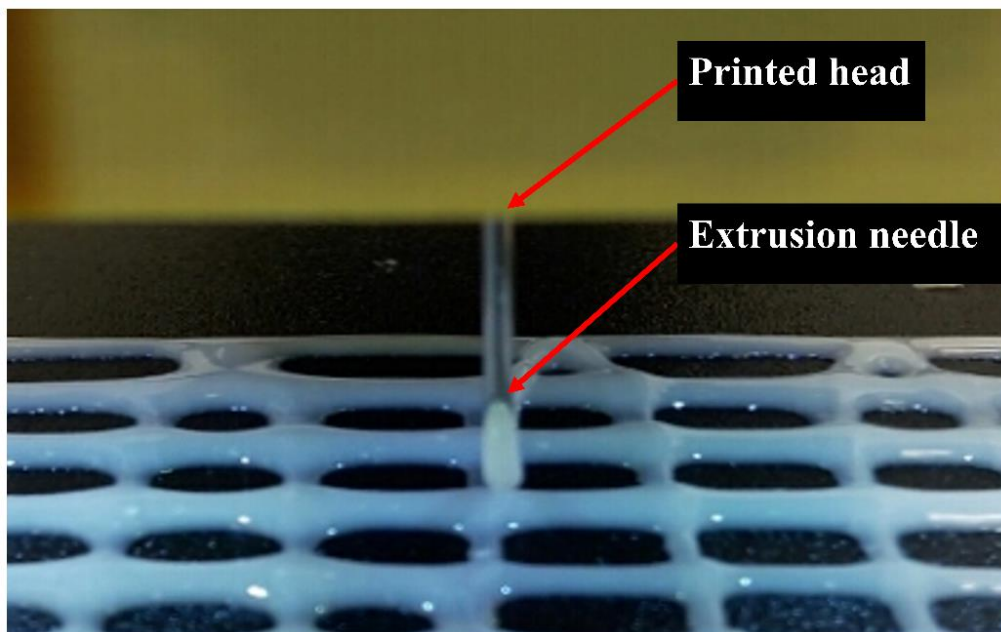


Figure 5.5 Extrusion based FDM technique for BTNFs-PVDF dielectric materials

The loading of BTNFs is varied from 0.6% vol. to 20% vol., and nozzle extruders of 2.5 mm and 1.2 mm were used to explore the effect of processing conditions on the nanofibers alignment. With a 2.5 mm nozzle diameter, a random distribution of the nanofibers is observed in SEM images for the sample at 0.6% vol. of BTNFs (Figure 5.6(a)), whereas with increasing content the BT nanofibers show clear alignment in the printing direction (Figure 5.6(c)). By contrast, in the hybrid at 20% vol. prepared using the nozzle 1.2 mm in diameter (Figure 5.6(d)) the BT

nanofibers are randomly distributed into the polymer matrix. This can be ascribed to an unstable

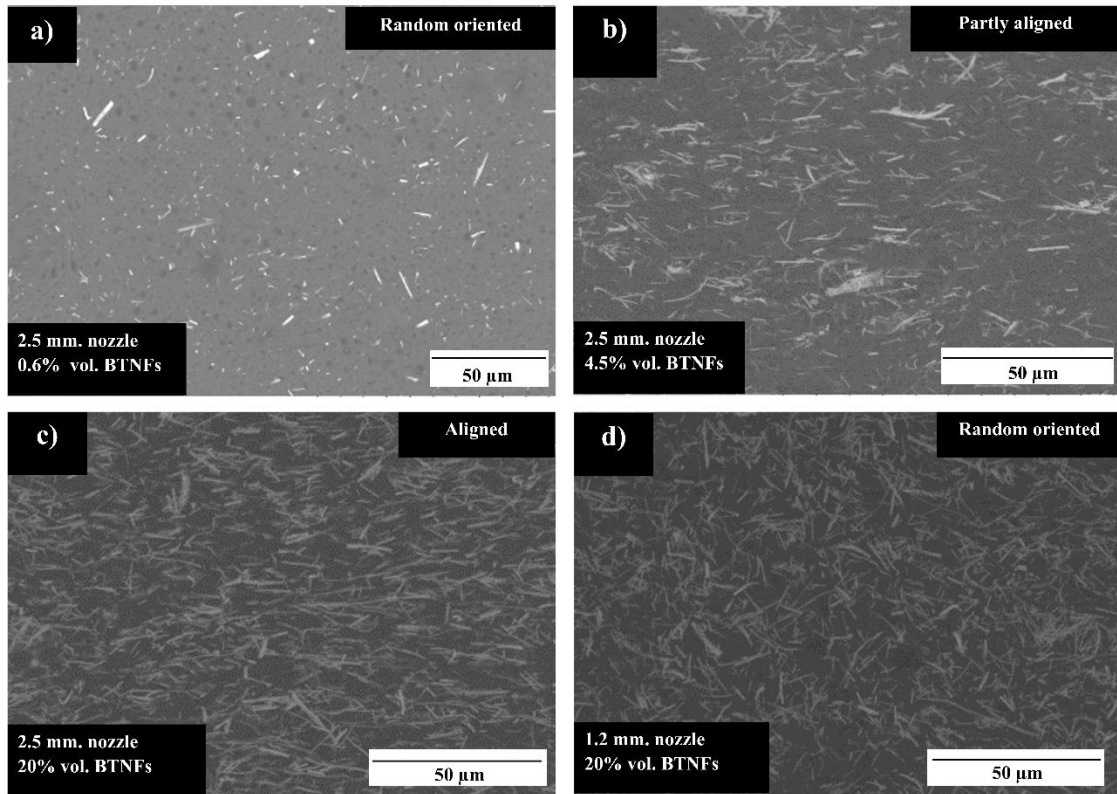


Figure 5.6 (a) Fibers alignment of BTNFs/PVDF materials printed by 2.5 mm of nozzle diameter 0.6% vol BTNFs; (b) 4.5% vol. BTNFs; (c) 20% vol. BTNFs and (d) 20% vol. BTNFs printed by 1.2 mm. of nozzle diameter.

flow generate from too high shear stress [50]. From the obtained results, we could produce the 3D printed object as complex shape and controllable fibers alignment in polymer matrix by this technique.

To further support the 2D observations in Figure 5.6, FIB-SEM 3D reconstruction of the 20% vol. BTNFs/PVDF nanohybrid sample was evaluated to verify and semi-quantitatively evaluate the degree of 3D fiber orientation. 3D FIB-SEM investigations inherently sample a smaller amount of representative microstructure. From the 2D images it can be seen that the microstructure contains nm- $\mu$ m sized highly elongated features and is spatially heterogeneous requiring

investigation of large volumes. For 3D reconstructions, these are conflicting requirements in terms of data acquisition time. Figure 5.7(a)-(b) shows a representative slice of the volume analysed.

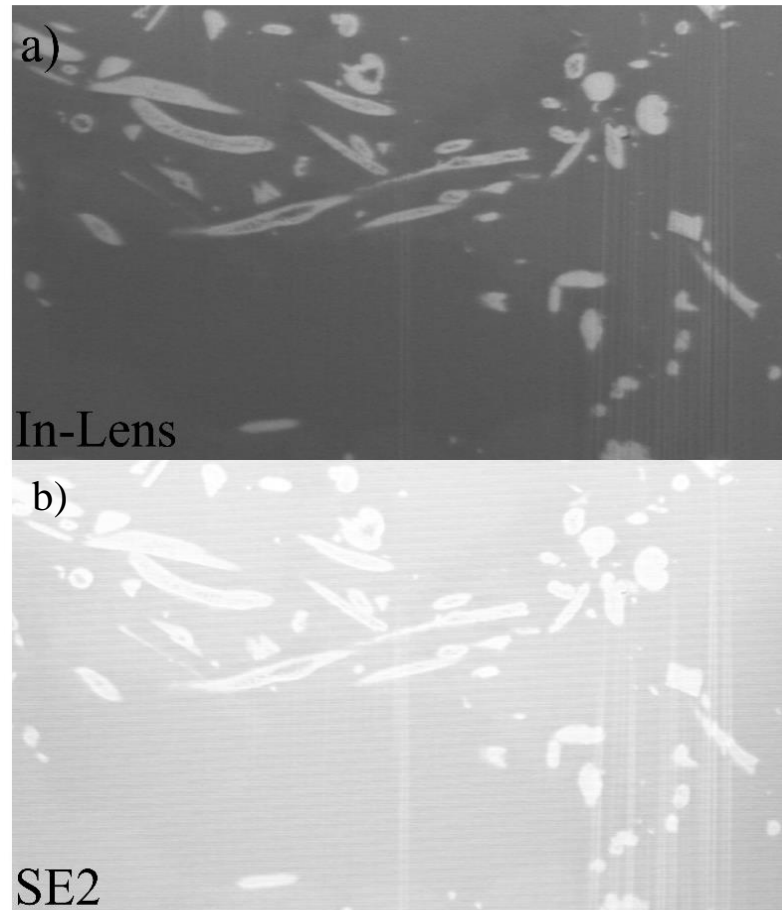


Figure 5.7 (a) In-lens (b) SE2 detector raw image slices from the middle of the vertical axis in the volume in figure 5.8 (a)

Here it can be seen in comparison to Figure 5.6(c) that the volume captures a visually representative volume with sufficient spatial resolution. Figure 5.7(a)-(b) contains both image modes, which are useful to distinguish internal porosity from edge effects and minimize FIB milling artefacts during segmentation. Visual inspection of the volume reveals internal porosity of both the BTNFs and the PVDF that is not visible in the polished cross-sections in Figure 5.6. In some reconstructed volume locations porosity induced artefacts were created in the segmentation and thus

add uncertainty to quantitative analysis. However, of the available quantitative parameters from 3D analysis, fibre orientation is one of the least sensitive to segmentation errors compared to volume fraction or particle size distribution determination. Thus, in the following analysis we discuss the results in a semi-quantitative manner.

Figure 5.8(a) shows the discretised skeleton of the BTNFs. Inspection of the BTNF phase after image segmentation revealed that although most of the BTNFs appear as isolated fibres in 2D, in 3D the majority of fibres are in contact. Thus after reconstruction from an image analysis point of view the majority of the BTNFs in the 20% vol. sample appear as an interconnected network. Thus breaking the skeleton of into a network graph of links and nodes was necessary to assess the orientation distribution of individual fibre fragments (links) visualised in arbitrary colours in Figure 5.8(a). The orientation of each fibre fragment, shown on the unit sphere in Figure 5.8(b) was determined by standard PCA where the direction of the largest variance in voxel coordinates determines the primary axis of fibre orientation. The points on the sphere represent a single fragment and are colour coded according to binned fragment lengths. This qualitatively shows that the orientations of fibre fragments shorter than approximately  $1 \mu\text{m}$  ( $\sim 20$  voxels in length) are randomly oriented. Longer fragments however tend to be oriented close to the applied shear stress/ extrusion direction (ED), and although fewer in numbers increasing fibre length correlates to stronger alignment.

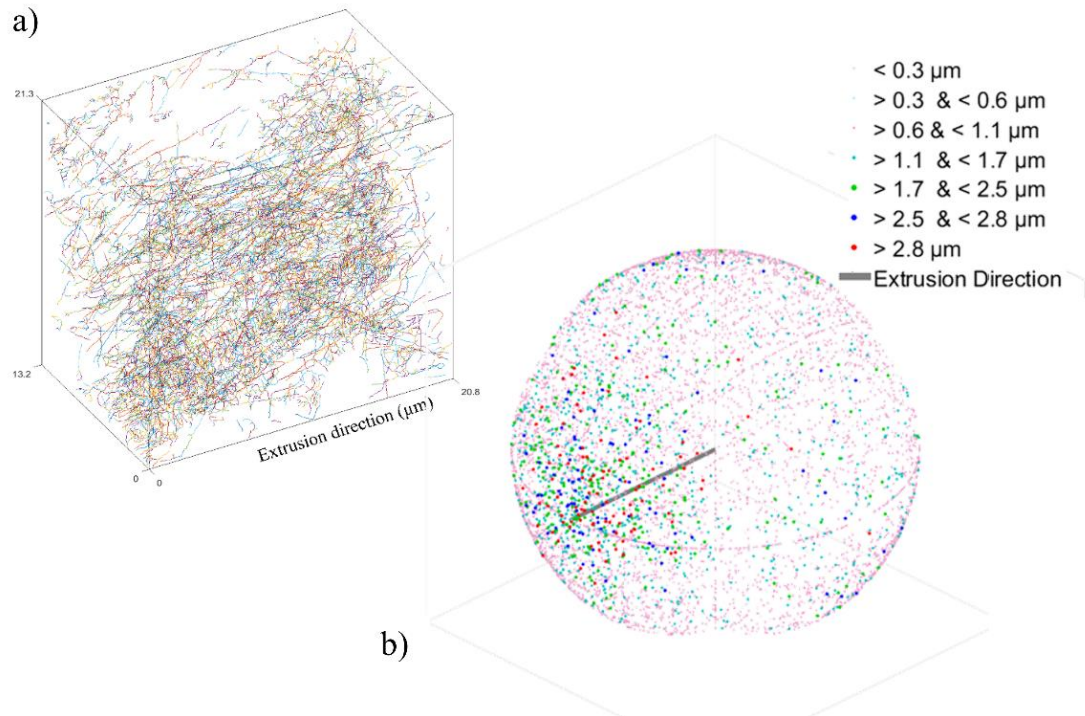


Figure 5.8 (a) A discretised skeleton of BTNFs segmented from the PVDF. Individual fragments of the BTNFs have been assigned random colours for visualisation. (b) Orientation of individual BTNF fragments plotted on a unit sphere, b and c are approximately aligned.

Figure 5.9 shows the distribution of fibre fragment ED angular deviation ( $\pm 90^\circ$  elevation angle in polar coordinates) for the same fragment length bins in Figure 5.8(b) weighted according to the cumulative fibre fragment length. Again the fragments shorter than  $\sim 1 \mu\text{m}$  reveal a wide spread in elevation angle with a strong bimodal peak parallel to ED and smaller peak centred at  $45^\circ$ . It is expected that the shorter skeleton links are more likely to be associated with the aforementioned segmentation uncertainties caused by large PVDF pores and fine scale internal BTNF porosity than the longer fragments. The peaks at  $0$  and  $45^\circ$  are also expected to be artificially increased due to the voxelisation of the skeleton links on a rectilinear grid. In Figure 5.8(a) it is possible to see long individual fibres, however the histogram statistically indicates that these fibres are broken into smaller fragments during

skeletonisation due to intersecting fibres. As seen in Figure 5.8(b) increasing fibre fragment length strongly correlates with a narrowing angular deviation and alignment with ED.

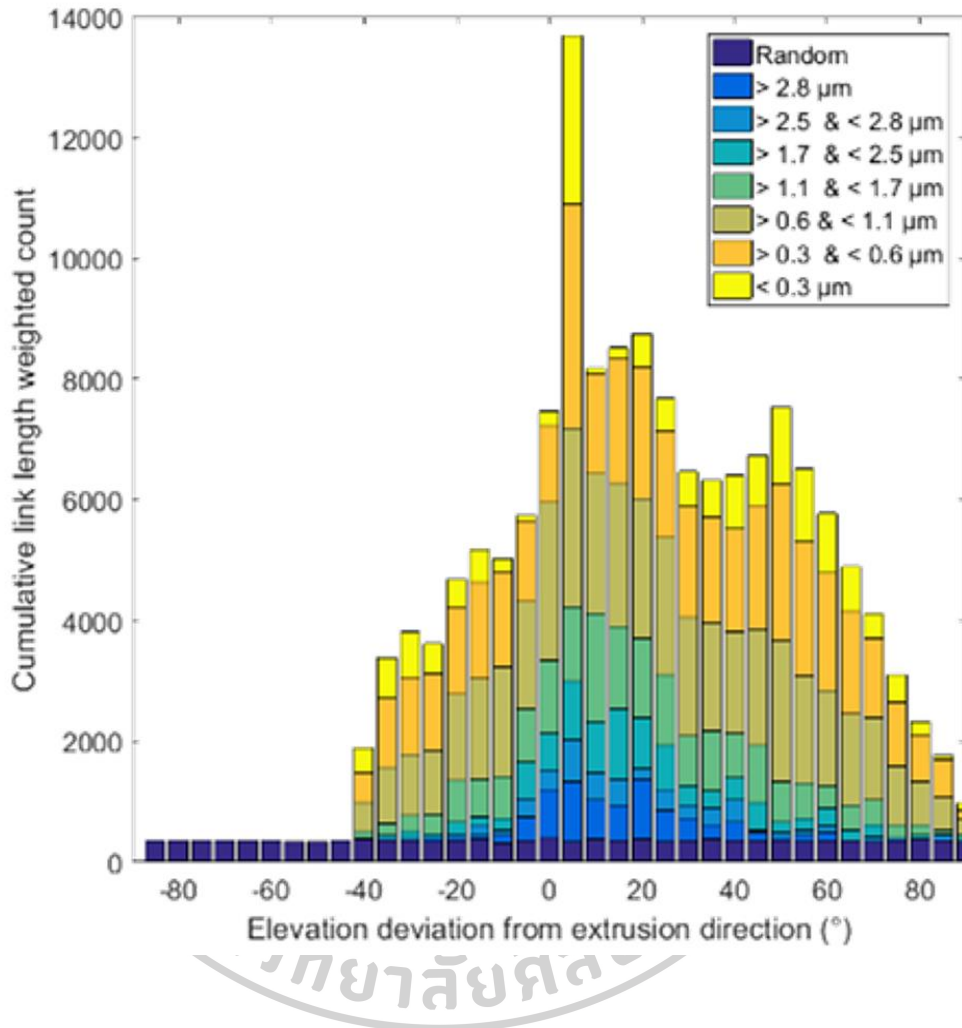


Figure 5.9 Stacked histograms of BTNF fragment angular (elevation) deviation from the extrusion direction as a function of fragment length. The histogram counts of elevation angle are weighted by fragment length. Note: the random distribution is on an arbitrary count scale.

For reference, the same number of fibre fragments (non-length weighted) a random distribution of angles was simulated using spherical point picking [51]. The grey coloured bins in the histogram show that randomly oriented fibres do not show no preferred correlation to ED contrary to the BTNFs.

To better understand the effect of the processing conditions on the nanofibers alignment, the rheological behaviour of the pure PVDF and BTNFs/PVDF nanohybrids were investigated. Particularly, the range of interest ( $1-100 \text{ s}^{-1}$ ) was selected to include the shear conditions that characterize the printing with the nozzles at 2.5 and 1.2 mm in diameter, as indicated in Figure 5.10(a). The two printing conditions identify a range of shear rate that spans from around 5 to  $30 \text{ s}^{-1}$ . The viscosity curves (Figure 5.10(a)) indicate a shear-thinning behaviour for all the samples. As expected, the profiles were progressively shifted to higher values of viscosity as the BTNFs content increases, due to the flow hindering effect [52, 53]. Yet, the solution at the highest content of BTNFs (20% vol.) not only exhibited the highest values of viscosity but also the most pronounced shear thinning profile. This behaviour was quantitatively estimated by analysing the flow indexes ( $n$ ) via the logarithmic form of the power law. The flow index is a measure of the deviation from the Newtonian behaviour ( $n=1$ ).

Plotting the experimental data, a linear trend is obtained as indicated in Figure 5.10(b), generally referred to as double logarithmic power law plot. The slope of the straight line corresponds to the flow index (estimated via a linear regression) that can be used to identify the flowing mechanism of a system [54-57]. Any variation of the flow index within a defined range of shear rates can be associated to variation in the flowing mechanism. Figure 5.10(b) shows the double logarithmic plot for the developed solutions, while in Table 5.1 the corresponding flow indexes are reported. As a consequence of the increasing BTNFs loading, the values of the flow index gradually decrease, indicating an increasing shear thinning behaviour ( $n < 1$ ) (see Table 5.1). Yet, all the samples, included the pure PVDF (see Figure 5.10(c)), exhibit a Multi Flow Index (MFI) profile with two flow indexes associated with two distinct flowing mechanisms, both resulting shear thinning. Interestingly for all of them, the second mechanism exhibits a more pronounced shear thinning behaviour, being  $n_2 < n_1$ . This result indicates for the flowing mechanism at higher shear rate a more pronounced deviation from the Newtonian behaviour likely associated with a transition in the polymer chains alignment. Interestingly, the transition is not altered by the addition of the BTNFs, since for all the PVDF samples it occurs at the same

shear rate, which is around  $20 \text{ s}^{-1}$ . This value is within the range defined by the nozzle diameters.

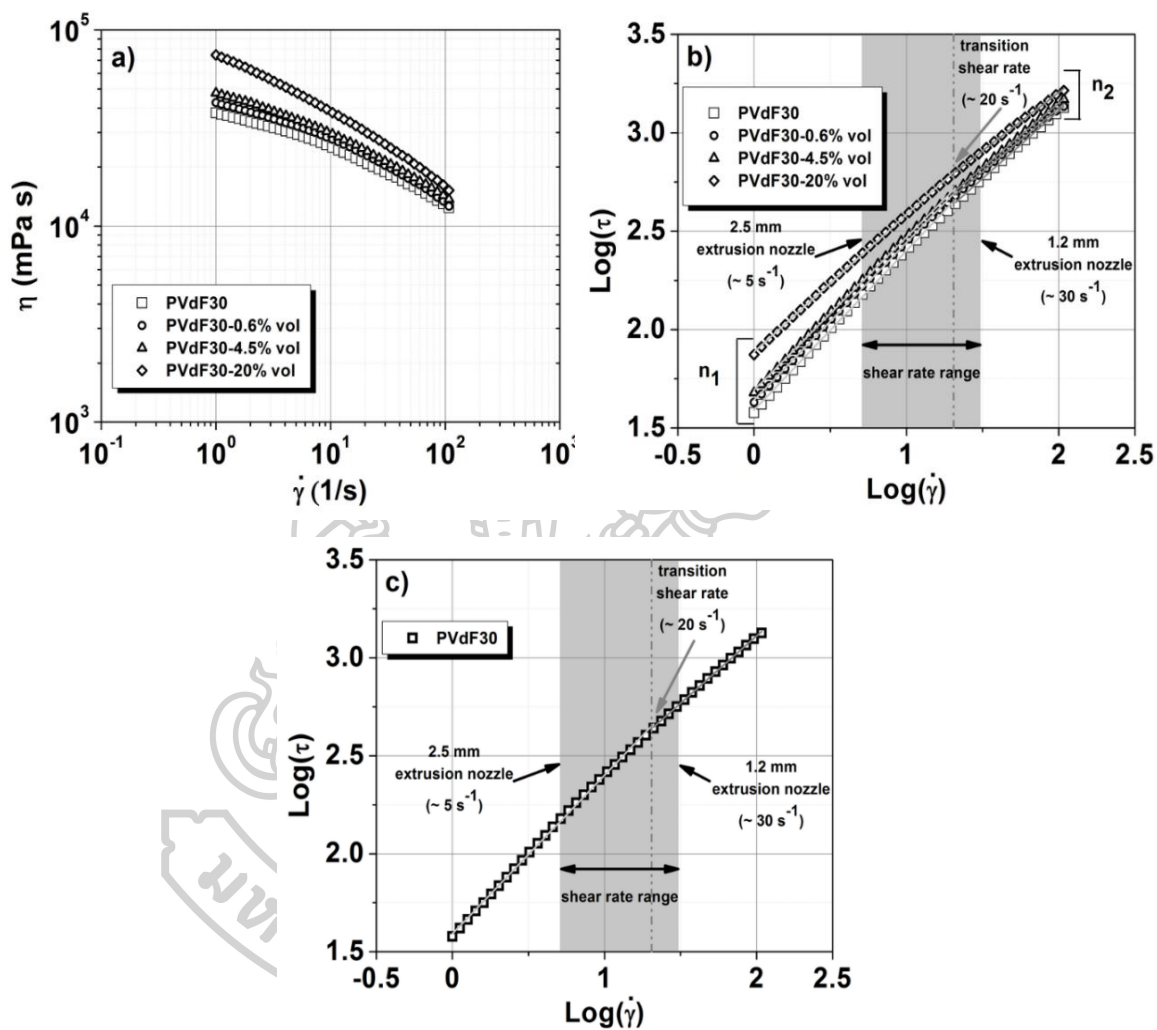


Figure 5.10 (a) Viscosity plot and the corresponding of the pure PVDF and BTNFs/PVDF nanohybrids, (b) double logarithmic power law plot for the complete series of PVDF-based solutions showing the flow index (slope), and (c) double logarithmic power law plot for the PVDF solutions.

Table 5.1 The flow indexes for the PVDF-based solutions.

Samples	Flow index	
	$n_1 (\dot{\gamma} < 20 \text{ s}^{-1})$	$n_2 (\dot{\gamma} > 20 \text{ s}^{-1})$
Pure PVDF	0.81	0.69
PVDF-BTNFs-0.6% vol.	0.80	0.67
PVDF-BTNFs-4.5% vol.	0.78	0.65
PVDF-BTNFs-20% vol.	0.70	0.59

As a result, all the PVDF samples printed using the nozzle with a diameter of 2.5 mm are processed at a shear rate (around  $5 \text{ s}^{-1}$ ) that characterizes the first mechanism of flowing. By contrast, all the PVDF samples printed using the nozzle with a diameter of 1.2 mm are processed at a shear rate (around  $30 \text{ s}^{-1}$ ) that characterizes the second mechanism of flowing. The higher flow index in the first flowing mechanism region ( $n_1$ ) indicates a lower level of interaction among PVDF chains, likely aligned into the direction of the applied shear stress. This arrangement can favour the interaction between the BT nanofibers and the polymer chains along the direction of applied shear stress. Such an arrangement is achieved when the nozzle with a diameter of 2.5 mm. By contrast, when the processing conditions exceed the identified threshold ( $20 \text{ s}^{-1}$ ,  $n_2$ ), the alignment might be disrupted, as indicated by a higher level of the interactions among the polymer chains ( $n_2 < n_1$ ). As consequence of that, BT nanofibers result randomly distributed within the polymer matrix. This is obtained when solutions are printed using the nozzle with a diameter of 1.2 mm.

Figure 5.11(a) and 5.11(b) show dielectric constant ( $k$ ) at room temperature ( $25 \text{ }^\circ\text{C}$ ) of pure PVDF and BTNFs/PVDF nanohybrids plotted against frequency for different % vol. of BTNFs in cross-direction (CD,  $k^\perp$ ) and parallel direction (PD,  $k^\parallel$ ), respectively. The dielectric constant of all the samples decreases with increasing frequency from 100 Hz to 1 MHz.

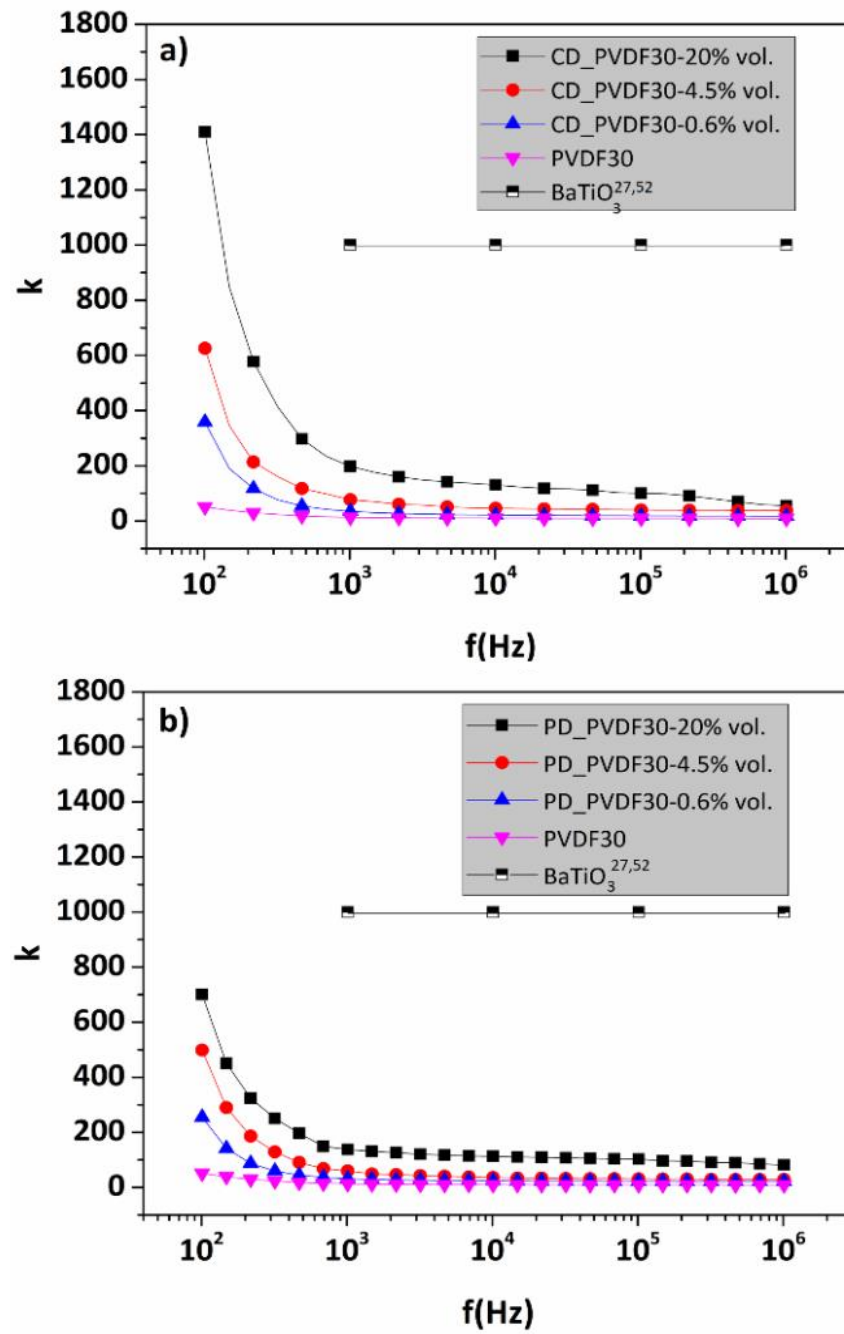


Figure 5.11 Frequency dependence of dielectric constant of (a) BTNFs/PVDF 3D-nanohybrid dielectric materials in cross direction (CD,  $k_{\perp}$ ), (b) in parallel direction (PD,  $k_{\parallel}$ ),

Higher values observed at low frequency (100 Hz ~ 1 kHz) are due to the interfacial polarization. The motion of space charges in the interface zone under the applied electric field induces significant polarization, thus producing high  $k$ -value. By contrast, at higher frequencies the dielectric properties of materials and lower values are then observed [34, 58]. In all cases, the dielectric constants of obtained BTNFs/PVDF nanohybrids are higher than the value of the pure PVDF, but lower than pure BT nanofibers (ca. 1000) [52] because of the synergy effect between the two phases [59].

The values of  $k^\perp$  are higher than  $k^\parallel$  ones at any content of BTNFs (Figure 5.12). Specifically, in hybrid materials with 20 % vol. of BTNFs at 1 kHz,  $k^\perp$  and  $k^\parallel$  values are 198 and 138, respectively. It can thus be concluded that the preferential nano-fibre alignment correlates strongly with the directionality of the observed dielectric constant [27].

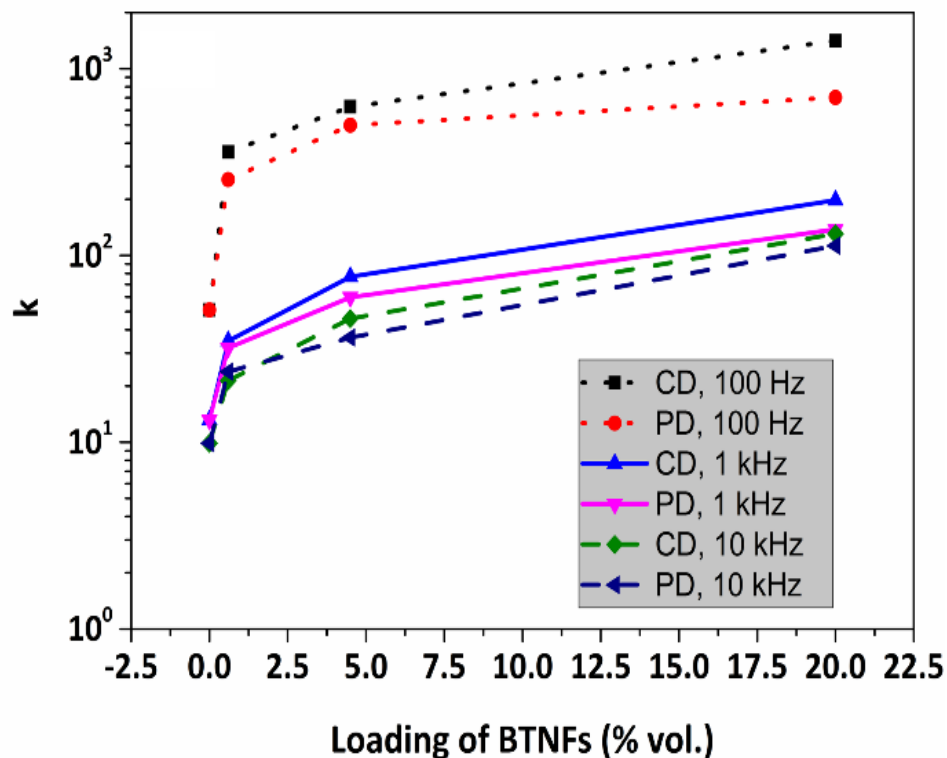


Figure 5.12 Dielectric constant of anisotropic BTNFs/PVDF 3D-nanohybrid dielectric materials at 100 Hz, 1 kHz and 10 kHz at room temperature.

At 1 kHz, the dielectric constant of hybrid samples both in cross direction (CD) and parallel direction (PD) increase with increasing amount of the BTNFs from 0.6 % vol. to 20 % vol. (Figure 5.12). This trend is due to the adding of higher amount of high-k component, resulting in higher-k values. The highest dielectric constant (k) of 198 was achieved from sample with 20 % vol. of BTNFs in cross direction evaluating.

Interestingly, compared with nanohybrids prepared with different methods and containing BT nanoparticles as fillers, BTNFs/PVDF systems herein developed show higher-k values at any content of BT nanofibers. In Figure 5.13 (a) comparison with different BT nanoparticles/PVDF hybrids prepared via solvent casting [21], spin-coating [22], and compression molding [23] is indicated.

This result can be ascribed to the incorporation of high aspect ratio nanofibers fillers that determines a significant increment of the hybrid interface (Figure 5.13(a)) [7, 17, 27]. In this work, we used effective medium theory (EMT) (eq.5.2) with fitting factor,  $n = 0.2$ ,  $\epsilon_{\text{filler}} = 1000$  and  $\epsilon_{\text{matrix}} = 13$ , and rule of mixtures (ROM) model for needle shape fillers (eq.5.3) to evaluate the k-values for the systems developed. The deviation of experimental data from models was then estimated. The results show that at any BTNFs volume fraction, the experimental data deviate from the calculated k-values (obtained with EMT and ROM models) (Figure 5.13(b)). This is especially verified at the highest content (20% vol. BTNFs), where deviations of around 80% and 50 % in average are obtained for EMT model and ROM model, respectively. This is likely ascribed to the attitude of nanostructured fillers to agglomerate that does not allow a homogeneous distribution of the nanofillers within the PVDF matrix.

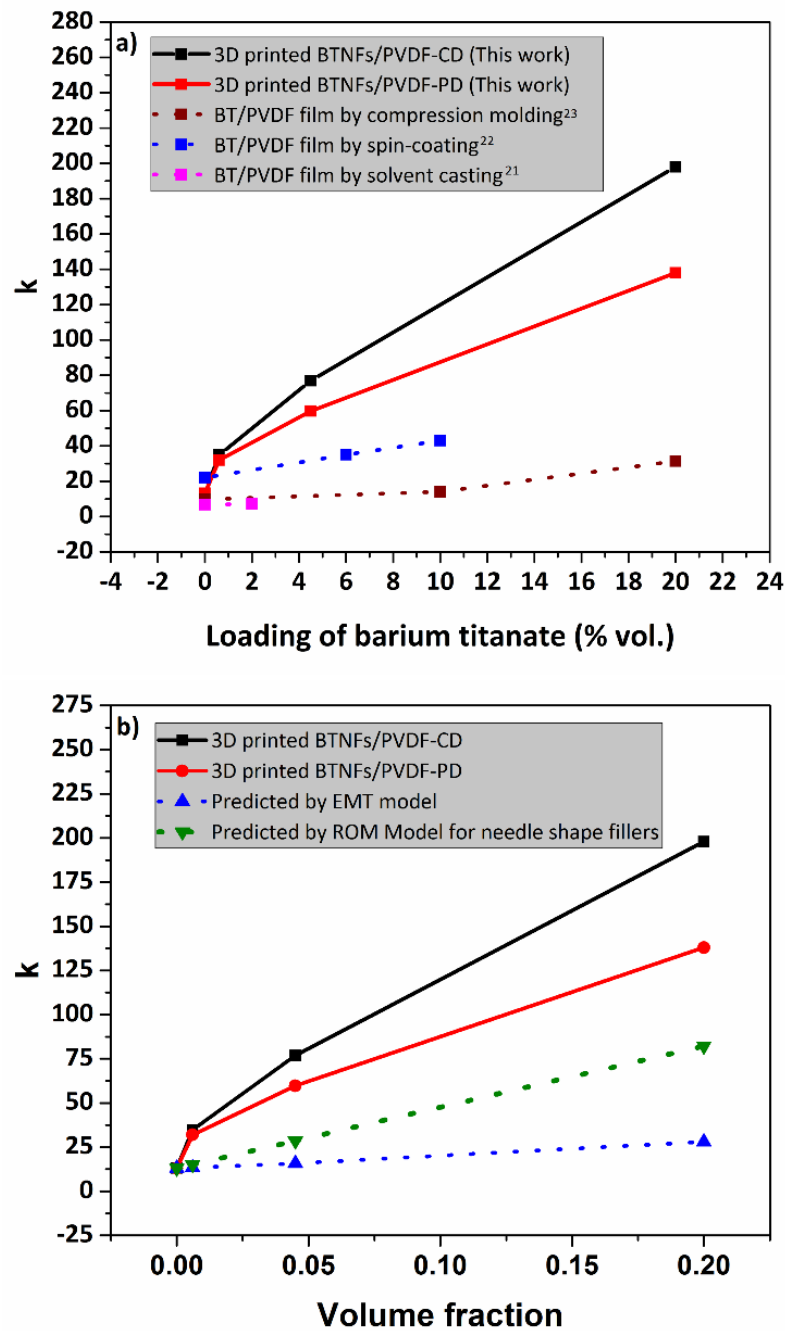


Figure 5.13 (a) Dielectric constant comparison between the 3D printed BTNFs/PVDF composites and the reported PVDF/BaTiO<sub>3</sub> composites at 1 kHz, room temperature and (b) Dielectric constant at 1 kHz from experiment vs predicted value from model equations

## 5.5 Conclusions

Barium titanate nanofibers-poly(vinylidene fluoride) nanohybrid dielectric materials (BTNFs/PVDF) are prepared by 3D-printing-FDM technique. Phase compositions, fibers alignment and dielectric constant are achieved by embedding high aspect ratio short-nanofibers in various concentrations. BTNFs induce high anisotropic behaviour in the hybrids. Alignment of BTNFs is triggered by a delicate interplay of viscoelastic effects at the printing throughout internal and external frictions within the hybrid and at the wall of the extruders at different flow rates. High enhancement of dielectric properties of more than 1 order of magnitude with respect of the pure PVDF can be achieved. Specifically, the BTNFs/PVDF 3D-nanohybrid dielectric material, with 20% vol. BTNFs, shows dielectric constant in cross-direction around 200 at frequency of 1 kHz at room temperature, vs 13 of the pristine PVDF materials. This enhancement can be associated with an extensive hybrid interface developed by the use of high aspect ratio 1D nanofillers. The anisotropic flexible 3D nano-hybrid composite with high-k constants is attractive for complex-shaped embedded capacitors and electric energy storage devices. We here demonstrate that this concept enables novel functionalities in dielectric components which could be applied for complex shaped embedded capacitor applications. We believe that the FDM technique provides great potential for developing high-k ferroelectric ceramic/polymer composites with controllable anisotropic properties.

## 5.6 References

1. Alluri, N.R., Saravanakumar, B. and Kim, S.J., Flexible, Hybrid Piezoelectric Film ( $\text{BaTi}_{(1-x)}\text{Zr}_{(x)}\text{O}_3$ )/PVDF Nanogenerator as a Self-Powered Fluid Velocity Sensor. *ACS applied materials & interfaces*, 2015. **7**(18): p. 9831-9840.
2. Ni, X., et al., Flexible Nanogenerator Based on Single  $\text{BaTiO}_3$  Nanowire. *Science of Advanced Materials*, 2013. **5**(11): p. 1781-1787.
3. Shin, S.H., et al., Hemispherically aggregated  $\text{BaTiO}_3$  nanoparticle composite thin film for high-performance flexible piezoelectric nanogenerator. *ACS nano*, 2014. **8**(3): p. 2766-2773.

4. Zhang, Y., et al., PVDF-PZT nanocomposite film based self-charging power cell. *Nanotechnology*, 2014. **25**(10): p. 105401.
5. Bai, Y., et al., High-dielectric-constant ceramic-powder polymer composites. *Applied Physics Letters*, 2000. **76**(25): p. 3804-3806.
6. Hammami, H., et al., Study of the interfacial MWS relaxation by dielectric spectroscopy in unidirectional PZT fibres/epoxy resin composites. *Journal of Alloys and Compounds*, 2007. **430**(1-2): p. 1-8.
7. Nicole, L., et al., Hybrid materials science: a promised land for the integrative design of multifunctional materials. *Nanoscale*, 2014. **6**(12): p. 6267-6292.
8. Sperati, C.A. (1989). **Polymer handbook**. New York: Wiley-Interscience
9. Chu, B., et al., A dielectric polymer with high electric energy density and fast discharge speed. *Science*, 2006. **313**(5785): p. 334-336.
10. Kobayashi, Y., et al., Fabrication and dielectric properties of the BaTiO<sub>3</sub>-polymer nano-composite thin films. *Journal of the European Ceramic Society*, 2008. **28**(1): p. 117-122.
11. Li, Y.I., Moon, K.S. and Wong, C.P., Electronics without lead. *Science*, 2005. **308**(5727): p. 1419-1420.
12. Bodkhe, S., et al., One-Step Solvent Evaporation-Assisted 3D Printing of Piezoelectric PVDF Nanocomposite Structures. *ACS applied materials & interfaces*, 2017. **9**(24):p. 20833-20842.
13. Gaur, M. S., et al., Thermally stimulated discharge current (TSDC) characteristics in  $\beta$ -phase PVDF- BaTiO<sub>3</sub> nanocomposites. *Journal of Thermal Analysis and Calorimetry*, 2014. **117**(3): p. 1407-1417.
14. Luo, H., et al., Ultra-high discharged energy density capacitor using high aspect ratio Na<sub>0.5</sub>Bi<sub>0.5</sub>TiO<sub>3</sub> nanofibers. *Journal of Materials Chemistry A*, 2017. **5**(15): p. 7091-7102.
15. Luo, H., et al., Improved Dielectric Properties and Energy Storage Density of P (VDF-HFP) Nanocomposite with Hydantoin Epoxy Resin Coated BaTiO<sub>3</sub>. *ACS applied materials & interfaces*, 2015. **7**: p. 8061-8069.
16. Tang, H., Lin, Y. and Sodano, H.A., Synthesis of high aspect ratio BaTiO<sub>3</sub> nanowires for high energy density nanocomposite capacitors. *Advanced Energy Materials*, 2013. **3**(4): p. 451-456.

17. Marani, D., et al., Titania nanosheets (TNS)/sulfonated poly ether ether ketone (SPEEK) nanocomposite proton exchange membranes for fuel cells. *Chemistry of Materials*, 2009. **22**(3): p. 1126-1133.
18. Yun, W.S., et al., Ferroelectric properties of individual barium titanate nanowires investigated by scanned probe microscopy. *Nano letters*, 2002. **2**(5): p. 447-450.
19. Yuh, J., Nino, J.C. and Sigmund, W.M., Synthesis of barium titanate ( $\text{BaTiO}_3$ ) nanofibers via electrospinning. *Materials Letters*, 2005. **59**(28): p. 3645-3647.
20. Urban, J.J., et al., Single-Crystalline Barium Titanate Nanowires. *Advanced Materials*, 2003. **15**(5): p. 423-426.
21. Upadhyay, R.H. and Deshmukh, R.R., Investigation of dielectric properties of newly prepared  $\beta$ -phase polyvinylidene fluoride–barium titanate nanocomposite films. *Journal of Electrostatics*, 2013. **71**(5): p. 945-950.
22. Li, Y.X., et al., Dielectric and Energy Storage Properties of Polyvinylidene Fluoride/Barium Titanate Nanocomposites. *Advanced Materials Research*, 2014. **833**:p. 365-369.
23. Li, Y.C., Tjong, S.C. and Li, R.K.Y., Dielectric properties of binary polyvinylidene fluoride/barium titanate nanocomposites and their nanographite doped hybrids. *eXPRESS Polymer Letters*, 2011. **5**(6): p. 526-534.
24. Kim, K., et al., 3D optical printing of piezoelectric nanoparticle-polymer composite materials. *ACS nano*, 2014. **8**(10): p. 9799-9806.
25. Castles, F., et al., Microwave dielectric characterisation of 3D-printed  $\text{BaTiO}_3$ /ABS polymer composites. *Scientific reports*, 2016. **6**: p. 22714.
26. Sun, K., et al., 3D printing of interdigitated Li-Ion microbattery architectures. *Advanced Materials*, 2013. **25**(33): p.4539-4543.
27. Krakovský, I. and Myroshnychenko, V., Modeling dielectric properties of composites by finite-element method. *Journal of applied physics*, 2002. **92**(11): p. 6743-6748.
28. Yuh, J., et al., Sol-gel based synthesis of complex oxide nanofibers. *Journal of sol-gel science and technology*, 2007. **42**(3): p. 323-329.

29. Jørgensen, P.S., Ebbenhøj, S.L. and Hauch, A., Triple phase boundary specific pathway analysis for quantitative characterization of solid oxide cell electrode microstructure. *Journal of Power Sources*, 2015. **279**: p. 686-693.
30. Jørgensen, P.S., et al., A framework for automatic segmentation in three dimensions of microstructural tomography data. *Ultramicroscopy*, 2010. **110**(3): p. 216-228.
31. GitHub, Inc., (US), (2017). **Skeleton3d-matlab**. Accessed on 22 September, 2017. Available from: <https://github.com/phi-max/skeleton3d-matlab>.
32. Kerschnitzki, M., et al., Architecture of the osteocyte network correlates with bone material quality. *Journal of bone and mineral research*, 2013. **28**(8): p. 1837-1845.
33. GitHub, Inc., (US), (2016). **Skel2graph3d-matlab**. Accessed on 22 September, 2017. Available from: <https://github.com/phi-max/skel2graph3d-matlab>.
34. Devi, P.I. and Ramachandran, K., Dielectric studies on hybridised PVDF–ZnO nanocomposites. *Journal of Experimental Nanoscience*, 2011. **6**(3): p. 281-293.
35. Yang, X., et al., Spatially-confined crystallization of poly(vinylidene fluoride). *Polymer International*, 2000. **49**(11): p. 1525-1528.
36. Chen, C., et al., Comparison of Efficiencies and Mechanisms of Catalytic Ozonation of Recalcitrant Petroleum Refinery Wastewater by Ce, Mg, and Ce-Mg Oxides Loaded Al<sub>2</sub>O<sub>3</sub>. *Catalysts*, 2017. **7**(3): p. 72.
37. Kumar, S., Messing, G.L. and White, W.B., Metal organic resin derived barium titanate: I, Formation of barium titanium oxycarbonate intermediate. *Journal of the American Ceramic Society*, 1993. **76**(3): p. 617-624.
38. Maensiri, S., et al., Nanofibers of barium strontium titanate (BST) by sol–gel processing and electrospinning. *Journal of colloid and interface science*, 2006. **297**(2): p. 578-583.
39. Kozuka, H. and Higuchi, A., Single-layer submicron-thick BaTiO<sub>3</sub> coatings from poly (vinylpyrrolidone)-containing sols: Gel-to-ceramic film conversion,

- densification, and dielectric properties. *Journal of Materials Research*, 2001. **16**(11): p. 3116-3123.
40. Lee, D.Y., et al., Effect of calcination temperature and atmosphere on crystal structure of BaTiO<sub>3</sub> nanofibers. *Metals and Materials International*, 2010. **16**(3): p. 453-457.
  41. Wang, Z.L. and Song, J., Piezoelectric nanogenerators based on zinc oxide nanowire arrays. *Science*, 2006. **312**(5771): p. 242-246.
  42. Ding, B., et al., Layer-by-layer self-assembled tubular films containing polyoxometalate on electrospun nanofibers. *Colloids and Surfaces A: Physicochemical and Engineering Aspects*, 2006. **284**: p. 257-262.
  43. Li, L., et al., Phase transformation and morphological evolution of electrospun zirconia nanofibers during thermal annealing. *Ceramics International*, 2010. **36**(2): p. 589-594.
  44. Marani, D., et al., NO<sub>x</sub> selective catalytic reduction (SCR) on self-supported V–W-doped TiO<sub>2</sub> nanofibers. *New Journal of Chemistry*, 2017. **41**(9): p. 3466-3472.
  45. Yin, L., et al., Preparation and photocatalytic activity of nanoporous zirconia electrospun fiber mats. *Materials Letters*, 2011. **65**(19-20): p. 3131-3133.
  46. Singh, R., et al., Low frequency ac conduction and dielectric relaxation behavior of solution grown and uniaxially stretched poly (vinylidene fluoride) films. *Polymer*, 2006. **47**(16): p. 5919-5928.
  47. Rajendran, S., Sivakumar, P. and Babu, R.S., Studies on the salt concentration of a PVdF-PVC based polymer blend electrolyte. *Journal of power sources*, 2007. **164**(2): p. 815-821.
  48. Yu, S., et al., Formation mechanism of  $\beta$ -phase in PVDF/CNT composite prepared by the sonication method. *Macromolecules*, 2009. **42**(22): p. 8870-8874.
  49. Li, Z., Zhang, X. and Li, G., In situ ZnO nanowire growth to promote the PVDF piezo phase and the ZnO-PVDF hybrid self-rectified nanogenerator as a touch sensor. *Physical Chemistry Chemical Physics*, 2014. **16**(12): p. 5475-5479.

50. Lewis, J.A., et al., Direct ink writing of three-dimensional ceramic structures. *Journal of the American Ceramic Society*, 2006. **89**(12): p. 3599-3609.
51. Wolfram Research, Inc. (2002). **Sphere Point Picking**. Accessed on 22 September, 2017. Available from: <http://mathworld.wolfram.com/SpherePointPicking.html>.
52. Wu, D., et al., Rheology of carbon nanotubes–filled poly (vinylidene fluoride) composites. *Industrial & Engineering Chemistry Research*, 2012. **51**(19): p. 6705-6713.
53. Vidhate, S., et al., Crystallization, mechanical, and rheological behavior of polyvinylidene fluoride/carbon nanofiber composites. *Journal of applied polymer science*, 2009. **112**(1): p. 254-260.
54. Marani, D., Hjelm, J. and Wandel, M., Rheological analysis of stabilized cerium-gadolinium oxide (CGO) dispersions. *Journal of the European Ceramic Society*, 2014. **34**(3): p. 695-702.
55. Marani, D., et al., Colloidal stabilization of cerium-gadolinium oxide (CGO) suspensions via rheology. *Journal of the European Ceramic Society*, 2015. **35**(10): p. 2823-2832.
56. Marani, D., et al., Influence of hydroxyl content of binders on rheological properties of cerium–gadolinium oxide (CGO) screen printing inks. *Journal of the European Ceramic Society*, 2015. **35**(5): p. 1495-1504.
57. Marani, D., et al., Enhanced densification of thin tape cast Ceria-Gadolinium Oxide (CGO) layers by rheological optimization of slurries. *Ceramics International*, 2017. **43**(7): p. 5647-5653.
58. Benlahrache, M., et al., Influence of polarization electric field on the dielectric properties of BaTiO<sub>3</sub>-based ceramics. *Materials science in semiconductor processing*, 2006. **9**(6): p. 1115-1118.
59. Hu, G., et al., Preparation and dielectric properties of poly (vinylidene fluoride)/Ba<sub>0.6</sub>Sr<sub>0.4</sub>TiO<sub>3</sub> composites. *Journal of Alloys and Compounds*, 2015. **619**: p. 686-692.

## Chapter 6

### Summary

Coconut shell, a food solid waste, was successfully utilized as a low cost alternative material for the electrode in supercapacitor device and the removal of textile dye. Highly porous activated carbon was successfully prepared from agricultural coconut shell waste as precursor with KOH activation at impregnation ratio of 3:1 and carbonization 800 °C. The resulting electrode from coconut shell based activated carbon showed excellent electrochemical behavior with a maximum specific capacitance of 149.65 F/g at a current density of 0.5 A/g. Furthermore, this resulting electrode also showed good rate capability and the specific capacitance decreased less than 35% (65% capacity retention) as the current density was raised from 0.5 to 4 A/g. Clearly, this obtained material is a promising and useful electrode material for electrochemical supercapacitors. Moreover, the TiO<sub>2</sub>/activated carbon double-layered film photocatalysts were successfully fabricated using an electrophoretic deposition technique without additives. The TiO<sub>2</sub>/activated carbon catalyst showed high photocatalytic efficiency and stability. The color removal efficiency of TiO<sub>2</sub>/activated carbon hybrid film obtained using the synthesized TiO<sub>2</sub> was found to be 97%. The hybrid film system has an advantage for wastewater treatment in practical applications because it is easy to separate from the process, cost-effective, eco-friendly, and reusable with relatively high photocatalytic efficiency. Therefore, the resulting photocatalyst is suitable for practical applications in heterogeneous photocatalysis technologies. Additionally, the titania-based ceramics-polymer hybrid materials; bismuth titanate/polyvinylpyrrolidone (BiT/PVP) and barium titanate/poly-(vinylidene fluoride) (BTNFs/PVDF) nanohybrids, were prepared and their performances were examined. The nanohybrids were synthesized and fabricated using the sol-gel chemistry followed by extrusion based 3D-printing (FDM) technique. The BiT/PVP sample with 3.0 vol. % of PVP displayed a good printing speed range which was enlarged over 50% of pure BiT gel. The obtained results are useful for optimizing and setting the 3D printing parameters. Moreover, the anisotropic 3D BTNFs/PVDF nanohybrids were successfully fabricated via FDM

technique, BTNFs were synthesized via sol-gel followed by electrospinning method. The BTNFs/PVDF 3D-nanohybrids with 20 vol. % BTNFs showed the highest dielectric constant in cross-direction around 200 at frequency of 1 kHz at room temperature, vs 13 of the pristine PVDF materials. In conclusion, FDM technique can provide novel functionalities in dielectric components which is applied for complex-shaped embedded capacitor applications.



## REFERENCES

1. U.S. Energy Information Administration. (2016). **World energy demand and economic outlook**. Accessed on October 24, 2016. Available from: [https://www.eia.gov/outlooks/ieo/exec\\_summ.php](https://www.eia.gov/outlooks/ieo/exec_summ.php).
2. Zou, C., et al., Energy revolution: From a fossil energy era to a new energy era. *Natural Gas Industry B*, 2016. **3**(1): p. 1-11.
3. Eurostat. (2013). **Quality of life - Natural and living environment**. Accessed on October 24, 2016. Available from: [http://ec.europa.eu/eurostat/statistics-explained/index.php?title=Quality\\_of\\_life\\_indicators\\_-\\_natural\\_and\\_living\\_environment](http://ec.europa.eu/eurostat/statistics-explained/index.php?title=Quality_of_life_indicators_-_natural_and_living_environment).
4. Victoria Transport Policy Institute. (2017). **Energy Conservation and Emission Reduction Strategies**. Accessed on April 30, 2017. Available from: <http://vtpi.org/tdm/tdm59.htm>.
5. Investment, T.B.o. (2017). **Investment Opportunities in Thailand**. Accessed on October 28, 2017. Available from: [http://www.boi.go.th/upload/content/\[Edited\]%20PPT%20for%20SG%20120917\\_EN%20as%20of%20130917\\_21011.pdf](http://www.boi.go.th/upload/content/[Edited]%20PPT%20for%20SG%20120917_EN%20as%20of%20130917_21011.pdf).
6. Kilner, J. A., et al. (2012). **Functional Materials for Sustainable Energy Applications**. Cambridge: Woodhead Publishing.
7. Butt, F.K. and Bandarenka, A.S., Microwave-assisted synthesis of functional electrode materials for energy applications. *Journal of Solid State Electrochemistry*, 2016. **20**(11): p. 2915-2928.
8. Huggins, R. A. (2010). **Energy storage**. New York: Springer.
9. Marshall, B., Charles, W. B., and Clint, P. (2017). **How Batteries Work**. Accessed on April 30, 2017. Available from: <http://electronics.howstuffworks.com/everyday-tech/battery3.htm>.
10. Divya, K.C. and Østergaard, J., Battery energy storage technology for power systems-An overview. *Electric Power Systems Research*, 2009. **79**(4): p. 511-520.
11. Joseph, A. and Shahidehpour, M. (2006). "**Battery storage systems in electric power systems.**" In Power Engineering Society General Meeting, IEEE.

12. Etacheri, V., et al., Challenges in the development of advanced Li-ion batteries: a review. *Energy & Environmental Science*, 2011. **4**(9): p. 3243-3262.
13. Aneke, M. and Wang, M., Energy storage technologies and real life applications - A state of the art review. *Applied Energy*, 2016. **179**: p. 350-377.
14. Mahlia, T. M. I., et al., A review of available methods and development on energy storage; technology update. *Renewable and Sustainable Energy Reviews*, 2014. **33**: p. 532-545.
15. Marshall, B., and Charles, W. B. (2017). **How Capacitors Work**. Accessed on April 30, 2017. Available from:  
<http://electronics.howstuffworks.com/capacitor1.htm>.
16. Jayalakshmi, M. and Balasubramanian, K., Simple capacitors to supercapacitors - an overview. *International Journal of Electrochemical Science*, 2008. **3**(11): p. 1196-1217.
17. Nishino, A., Capacitors: operating principles, current market and technical trends. *Journal of Power Sources*, 1996. **60**(2): p. 137-147.
18. Elcap. (2017). **Fixed capacitors-charge storage principles**. Accessed on October 15, 2017. Available from:  
[https://upload.wikimedia.org/wikipedia/commons/5/5b/Fixed\\_capacitors-charge\\_storage\\_principles.png](https://upload.wikimedia.org/wikipedia/commons/5/5b/Fixed_capacitors-charge_storage_principles.png)
19. Largeot, C., et al., Relation between the ion size and pore size for an electric double-layer capacitor. *Journal of the American Chemical Society*, 2008. **130**(9): p. 2730-2731.
20. Kandalkar, S. G., et al., Chemical synthesis of cobalt oxide thin film electrode for supercapacitor application. *Synthetic Metals*, 2010. **160**(11-12): p. 1299-1302.
21. Conway, B.E. (2013). **Electrochemical supercapacitors: scientific fundamentals and technological applications**. New York: Springer Science & Business Media.
22. Qian, K., et al., Recent advances in utilization of biochar. *Renewable and Sustainable Energy Reviews*, 2015. **42**: p. 1055-1064.
23. Zhao, X., et al., The role of nanomaterials in redox-based supercapacitors for

- next generation energy storage devices. *Nanoscale*, 2011. **3**(3): p.839-855.
24. Mastragostino, M., Arbizzani, C. and Soavi, F., Conducting polymers as electrode materials in supercapacitors. *Solid State Ionics*, 2002. **148**(3-4): p. 493-498.
  25. Pandolfo, A.G. and Hollenkamp, A.F., Carbon properties and their role in supercapacitors. *Journal of Power Sources*, 2006. **157**(1): p. 11-27.
  26. Tomiyasu, H., et al., An aqueous electrolyte of the widest potential window and its superior capability for capacitors. *Scientific Reports*, 2017. **7**: p. 45048.
  27. Cavaliere, S., et al., Electrospinning: designed architectures for energy conversion and storage devices. *Energy & Environmental Science*, 2011. **4**(12): p. 4761-4785.
  28. Leng, C. and Sun, K., The preparation of 3D network pore structure activated carbon as an electrode material for supercapacitors with long-term cycle stability. *RSC Advances*, 2016. **6**(62): p. 57075-57083.
  29. Olivares-Marín, M., et al., Cherry stones as precursor of activated carbons for supercapacitors. *Materials Chemistry and Physics*, 2009. **114**(1): p. 323-327.
  30. Johnson, K.E., What's an ionic liquid? *Interface-Electrochemical Society*, 2007. **16**(1): p. 38-41.
  31. Ohno, H. and Fukumoto, K., Progress in ionic liquids for electrochemical reaction matrices. *Electrochemistry*, 2008. **76**(1): p. 16-23.
  32. Snook, G.A., Kao, P., and Best, A.S., Conducting-polymer-based supercapacitor devices and electrodes. *Journal of Power Sources*, 2011. **196**(1): p. 1-12.
  33. Armand, M., et al., Ionic-liquid materials for the electrochemical challenges of the future. *Nature materials*, 2009. **8**(8): p. 621-629.
  34. Balducci, A., et al., Development of safe, green and high performance ionic liquids-based batteries (ILLIBATT project). *Journal of Power Sources*, 2011. **196**(22): p. 9719-9730.
  35. Kühnel, R.S., et al., Mixtures of ionic liquid and organic carbonate as electrolyte with improved safety and performance for rechargeable lithium batteries. *Electrochimica Acta*, 2011. **56**(11): p. 4092-4099.
  36. Arbizzani, C., Mastragostino, M., and Soavi, F., New trends in electrochemical

- supercapacitors. *Journal of Power Sources*, 2001. **100**(1-2): p. 164-170.
37. Pekala, R.W., Organic aerogels from the polycondensation of resorcinol with formaldehyde. *Journal of Materials Science*, 1989. **24**(9): p. 3221-3227.
38. Pröbstle, H., Wiener, M. and Fricke, J., Carbon Aerogels for Electrochemical Double Layer Capacitors. *Journal of Porous Materials*, 2003. **10**(4): p. 213-222.
39. Yuan, G.H., et al., Electrochemical behavior of activated-carbon capacitor material loaded with nickel oxide. *Carbon*, 2005. **43**(14): p. 2913-2917.
40. Ishikawa, M., et al., Effect of treatment of activated carbon fiber cloth electrodes with cold plasma upon performance of electric double-layer capacitors. *Journal of power sources*, 1996. **60**(2): p. 233-238.
41. Xu, B., et al., Mesoporous activated carbon fiber as electrode material for high-performance electrochemical double layer capacitors with ionic liquid electrolyte. *Journal of Power Sources*, 2010. **195**(7): p. 2118-2124.
42. Ahn, H.J., et al., Electrochemical capacitors fabricated with carbon nanotubes grown within the pores of anodized aluminum oxide templates. *Electrochemistry communications*, 2006. **8**(4): p. 513-516.
43. Sivakkumar, S.R., et al., Performance evaluation of CNT/polypyrrole/MnO<sub>2</sub> composite electrodes for electrochemical capacitors. *Electrochimica Acta*, 2007. **52**(25): p. 7377-7385.
44. Ryu, K.S., et al., Symmetric redox supercapacitor with conducting polyaniline electrodes. *Journal of Power Sources*, 2002. **103**(2): p. 305-309.
45. Ahn, Y.R., et al., Electrochemical capacitors based on electrodeposited ruthenium oxide on nanofibre substrates. *Nanotechnology*, 2006. **17**(12): p. 2865-2869.
46. Ruiz, V., et al., Effects of thermal treatment of activated carbon on the electrochemical behaviour in supercapacitors. *Electrochimica Acta*, 2007. **52**(15): p. 4969-4973.
47. Zhang, Y., et al., Progress of electrochemical capacitor electrode materials: A review. *International Journal of Hydrogen Energy*, 2009. **34**(11): p. 4889-4899.
48. Inagaki, M. and Radovic, L.R., Nanocarbons. *Carbon*, 2002. **12**(40): p. 2279-2282.

49. Candelaria, S.L., et al., Nanostructured carbon for energy storage and conversion. *Nano Energy*, 2012. **1**(2): p. 195-220.
50. Liu, M.C., et al., Porous wood carbon monolith for high-performance supercapacitors. *Electrochimica Acta*, 2012. **60**: p. 443-448.
51. Basri, N.H., et al., Supercapacitors using binderless composite monolith electrodes from carbon nanotubes and pre-carbonized biomass residues. *Biomass and Bioenergy*, 2013. **59**: p. 370-379.
52. Farma, R., et al., Preparation of highly porous binderless activated carbon electrodes from fibres of oil palm empty fruit bunches for application in supercapacitors. *Bioresource Technology*, 2013. **132**: p. 254-261.
53. Goodman, P.A., et al., Preparation and characterization of high surface area, high porosity carbon monoliths from pyrolyzed bovine bone and their performance as supercapacitor electrodes. *Carbon*, 2013. **55**: p. 291-298.
54. Jiang, J., et al., Highly ordered macroporous woody biochar with ultra-high carbon content as supercapacitor electrodes. *Electrochimica Acta*, 2013. **113**: p. 481-489.
55. Wang, G., Zhang, L. and Zhang, J., A review of electrode materials for electrochemical supercapacitors. *Chemical Society Reviews*, 2012. **41**(2): p. 797-828.
56. Fan, L.Z. and Maier, J., High-performance polypyrrole electrode materials for redox supercapacitors. *Electrochemistry communications*, 2006. **8**(6): p. 937-940.
57. Ryu, K.S., et al., Redox supercapacitor using polyaniline doped with Li salt as electrode. *Solid State Ionics*, 2002. **152-153**: p. 861-866.
58. Hughes, M., et al., Electrochemical Capacitance of a Nanoporous Composite of Carbon Nanotubes and Polypyrrole. *Chemistry of Materials*, 2002. **14**(4): p. 1610-1613.
59. Malinauskas, A., Malinauskiene, J. and Ramanavičius, A., Conducting polymer-based nanostructured materials: electrochemical aspects. *Nanotechnology*, 2005. **16**(10): p. R51-62.
60. Arbizzani, C., Mastragostino, M. and Meneghello, L., Characterization by

- impedance spectroscopy of a polymer-based supercapacitor. *Electrochimica Acta*, 1995. **40**(13-14): p. 2223-2228.
61. Vlad, A., et al., Hybrid supercapacitor-battery materials for fast electrochemical charge storage. *Scientific reports*, 2014. **4**: p.4315.
  62. Wang, Q., Wen, Z.H. and Li, J.H., A Hybrid Supercapacitor Fabricated with a Carbon Nanotube Cathode and a TiO<sub>2</sub>-B Nanowire Anode. *Advanced Functional Materials*, 2006. **16**(16): p. 2141-2146.
  63. Zhang, F., et al., A high-performance supercapacitor-battery hybrid energy storage device based on graphene-enhanced electrode materials with ultrahigh energy density. *Energy & Environmental Science*, 2013. **6**(5): p. 1623-1632.
  64. Zhao, X., Johnston, C. and Grant, P.S., A novel hybrid supercapacitor with a carbon nanotube cathode and an iron oxide/carbon nanotube composite anode. *Journal of Materials Chemistry*, 2009. **19**(46): p. 8755-8760.
  65. Crini, G., Recent developments in polysaccharide-based materials used as adsorbents in wastewater treatment. *Progress in Polymer Science*, 2005. **30**(1): p. 38-70.
  66. Rio, S. and Delebarre, A., Removal of mercury in aqueous solution by fluidized bed plant fly ash. *Fuel*, 2003. **82**(2): p. 153-159.
  67. Pearce, C.I., Lloyd, J.R. and Guthrie, J.T., The removal of colour from textile wastewater using whole bacterial cells: a review. *Dyes and pigments*, 2003. **58**(3): p. 179-196.
  68. McMullan, G., et al., Microbial decolourisation and degradation of textile dyes. *Applied microbiology and biotechnology*, 2001. **56**(1-2): p. 81-87.
  69. Fu, Y. and Viraraghavan, T., Fungal decolorization of dye wastewaters: a review. *Bioresource technology*, 2001. **79**(3): p. 251-262.
  70. Van der Bruggen, B. and Vandecasteele, C., Removal of pollutants from surface water and groundwater by nanofiltration: overview of possible applications in the drinking water industry. *Environmental pollution*, 2003. **122**(3): p. 435-445.
  71. Cassano, A., et al., Treatment of aqueous effluents of the leather industry by membrane processes: a review. *Journal of Membrane Science*, 2001. **181**(1): p. 111-126.

72. Goncharuk, V. V., et al., Removal of organic substances from aqueous solutions by reagent enhanced reverse osmosis. *Desalination*, 2002. **143**(1): p. 45-51.
73. Hu, Z., et al., Chromium adsorption on high-performance activated carbons from aqueous solution. *Separation and Purification Technology*, 2003. **31**(1): p. 13-18.
74. Chern, J.M. and Chien, Y.W., Competitive adsorption of benzoic acid and p-nitrophenol onto activated carbon: isotherm and breakthrough curves. *Water Research*, 2003. **37**(10): p. 2347-2356.
75. Pereira, M.F.R., et al., Adsorption of dyes on activated carbons: influence of surface chemical groups. *Carbon*, 2003. **41**(4): p. 811-821.
76. Rivera-Utrilla, J., et al., Bioadsorption of Pb (II), Cd (II), and Cr (VI) on activated carbon from aqueous solutions. *Carbon*, 2003. **41**(2): p. 323-330.
77. Nouri, S., Haghseresht, F. and Lu, G.M., Comparison of adsorption capacity of p-cresol & p-nitrophenol by activated carbon in single and double solute. *Adsorption*, 2002. **8**(3): p. 215-223.
78. Lee, J.M., et al., Photodegradation of acid red 114 dissolved using a photo-Fenton process with TiO<sub>2</sub>. *Dyes and Pigments*, 2003. **56**(1): p. 59-67.
79. Kurbus, T., et al., The use of experimental design for the evaluation of the influence of variables on the H<sub>2</sub>O<sub>2</sub>/UV treatment of model textile waste water. *Dyes and Pigments*, 2003. **58**(2): p. 171-178.
80. Torrades, F., et al., Experimental design of Fenton and photo-Fenton reactions for the treatment of cellulose bleaching effluents. *Chemosphere*, 2003. **53**(10): p. 1211-1220.
81. Al-Momani, F., et al., Biodegradability enhancement of textile dyes and textile wastewater by VUV photolysis. *Journal of photochemistry and Photobiology A: Chemistry*, 2002. **153**(1-3): p. 191-197.
82. Pelaez, M., et al., A review on the visible light active titanium dioxide photocatalysts for environmental applications. *Applied Catalysis B: Environmental*, 2012. **125**: p. 331-349.
83. Mills, A. and Le Hunte, S., An overview of semiconductor photocatalysis. *Journal of photochemistry and photobiology A: Chemistry*, 1997. **108**(1): p. 1-35.

84. Fujishima, A. and Honda, K., Electrochemical photolysis of water at a semiconductor electrode. *nature*, 1972. **238**(5358): p. 37-38.
85. Guesh, K., et al., Enhanced photocatalytic activity of TiO<sub>2</sub> supported on zeolites tested in real wastewaters from the textile industry of Ethiopia. *Microporous and Mesoporous Materials*, 2016. **225**: p. 88-97.
86. Imamura, K., et al., Stoichiometric production of aminobenzenes and ketones by photocatalytic reduction of nitrobenzenes in secondary alcoholic suspension of titanium (IV) oxide under metal-free conditions. *Applied Catalysis B: Environmental*, 2013. **134-135**: p. 193-197.
87. Rawal, S.B., et al., Design of visible-light photocatalysts by coupling of narrow bandgap semiconductors and TiO<sub>2</sub>: effect of their relative energy band positions on the photocatalytic efficiency. *Catalysis Science & Technology*, 2013. **3**(7): p. 1822-1830.
88. Janotti, A. and Van de Walle, C.G., Fundamentals of zinc oxide as a semiconductor. *Reports on progress in physics*, 2009. **72**(12): p. 126501.
89. Reynolds, D., et al., Valence-band ordering in ZnO. *Physical Review B*, 1999. **60**(4): p. 2340.
90. Chen, Y., et al., Plasma assisted molecular beam epitaxy of ZnO on c-plane sapphire: growth and characterization. *Journal of Applied Physics*, 1998. **84**(7): p. 3912-3918.
91. Daneshvar, N., Salari, D. and Khataee, A.R., Photocatalytic degradation of azo dye acid red 14 in water on ZnO as an alternative catalyst to TiO<sub>2</sub>. *Journal of photochemistry and photobiology A: chemistry*, 2004. **162**(2-3): p. 317-322.
92. Yeber, M.C., et al., Photocatalytic degradation of cellulose bleaching effluent by supported TiO<sub>2</sub> and ZnO. *Chemosphere*, 2000. **41**(8): p. 1193-1197.
93. Lee, S.Y. and Park, S.J., TiO<sub>2</sub> photocatalyst for water treatment applications. *Journal of Industrial and Engineering Chemistry*, 2013. **19**(6): p. 1761-1769.
94. Schmidt-Mende, L. and MacManus-Driscoll, J.L., ZnO-nanostructures, defects, and devices. *Materials today*, 2007. **10**(5): p. 40-48.
95. Behnajady, M.A., Modirshahla, N. and Hamzavi, R., Kinetic study on photocatalytic degradation of CI Acid Yellow 23 by ZnO photocatalyst. *Journal*

- of hazardous materials, 2006. **133**(1-3): p. 226-232.
96. Goesmann, H. and Feldmann, C., Nanoparticulate Functional Materials. *Angewandte Chemie International Edition*, 2010. **49**(8): p. 1362-1395.
  97. Xia, X.H., et al., Preparation of multi-walled carbon nanotube supported TiO<sub>2</sub> and its photocatalytic activity in the reduction of CO<sub>2</sub> with H<sub>2</sub>O. *Carbon*, 2007. **45**(4): p. 717-721.
  98. Woan, K., Pyrgiotakis, G. and Sigmund, W., Photocatalytic Carbon-Nanotube-TiO<sub>2</sub> Composites. *Advanced Materials*, 2009. **21**(21): p. 2233-2239.
  99. Xu, Y.J., Zhuang, Y. and Fu, X., New insight for enhanced photocatalytic activity of TiO<sub>2</sub> by doping carbon nanotubes: a case study on degradation of benzene and methyl orange. *The Journal of Physical Chemistry C*, 2010. **114**(6): p. 2669-2676.
  100. Apostolopoulou, V., et al., Preparation and characterization of [60] fullerene nanoparticles supported on titania used as a photocatalyst. *Colloids and Surfaces A: Physicochemical and Engineering Aspects*, 2009. **349**(1-3): p. 189-194.
  101. Meng, Z.D., et al., Effect of Pt treated fullerene/TiO<sub>2</sub> on the photocatalytic degradation of MO under visible light. *Journal of Materials Chemistry*, 2011. **21**(21): p. 7596-7603.
  102. Dai, Q., et al., Ozonation catalyzed by cerium supported on activated carbon for the degradation of typical pharmaceutical wastewater. *Separation and Purification Technology*, 2014. **127**: p. 112-120.
  103. Ou-Yang, Z., et al., Preparation of TiO<sub>2</sub>-supported activated carbon and its application in papermaking wastewater. *Advanced Materials Research*, 2013, **791**: p. 7-11.
  104. Benton, O., et al., Photodegradation of Molasses Wastewater Using TiO<sub>2</sub>-ZnO Nanohybrid Photocatalyst Supported on Activated Carbon. *Chemical Engineering Communications*, 2016. **203**(11): p. 1443-1454.
  105. Leary, R. and Westwood, A., Carbonaceous nanomaterials for the enhancement of TiO<sub>2</sub> photocatalysis. *Carbon*, 2011. **49**(3): p. 741-772.
  106. Chingombe, P., Saha, B. and Wakeman, R.J., Surface modification and characterisation of a coal-based activated carbon. *Carbon*, 2005. **43**(15): p. 3132-

- 3143.
107. Lim, T.T., et al., TiO<sub>2</sub>/AC composites for synergistic adsorption-photocatalysis processes: present challenges and further developments for water treatment and reclamation. *Critical Reviews in Environmental Science and Technology*, 2011. **41**(13): p. 1173-1230.
  108. Gar Alalm, M., Tawfik, A. and Ookawara, S., Solar photocatalytic degradation of phenol by TiO<sub>2</sub>/AC prepared by temperature impregnation method. *Desalination and Water Treatment*, 2016. **57**(2): p. 835-844.
  109. Quiñones, D.H., et al., Enhanced activity and reusability of TiO<sub>2</sub> loaded magnetic activated carbon for solar photocatalytic ozonation. *Applied Catalysis B: Environmental*, 2014. **144**: p. 96-106.
  110. McEvoy, J.G., Cui, W. and Zhang, Z., Synthesis and characterization of Ag/AgCl-activated carbon composites for enhanced visible light photocatalysis. *Applied Catalysis B: Environmental*, 2014. **144**: p. 702-712.
  111. Shukla, P.R., et al., Activated carbon supported cobalt catalysts for advanced oxidation of organic contaminants in aqueous solution. *Applied Catalysis B: Environmental*, 2010. **100**(3-4): p. 529-534.
  112. Roonasi, P. and Mazinani, M., Synthesis and application of barium ferrite/activated carbon composite as an effective solar photocatalyst for discoloration of organic dye contaminants in wastewater. *Journal of Environmental Chemical Engineering*, 2017. **5**(4): p. 3822-3827.
  113. Vinayagam, M., et al., Photocatalytic degradation of orange G dye using ZnO/biomass activated carbon nanocomposite. *Journal of Environmental Chemical Engineering*, 2017. **6**(3): p. 3726-3734.
  114. Lee, D., et al., Adsorbability enhancement of activated carbon by dielectric barrier discharge plasma treatment. *Surface and Coatings Technology*, 2005. **200**(7): p. 2277-2282.
  115. Li, Y.H., Lee, C.W. and Gullett, B.K., Gullett, Importance of activated carbon's oxygen surface functional groups on elemental mercury adsorption. *Fuel*, 2003. **82**(4): p. 451-457.
  116. Guo, Q., et al., Supercapacitors based on hybrid carbon nanofibers containing

- multiwalled carbon nanotubes. *Journal of Materials Chemistry*, 2009. **19**(18): p. 2810-2816.
117. Niu, H., et al., Preparation, structure and supercapacitance of bonded carbon nanofiber electrode materials. *Carbon*, 2011. **49**(7): p. 2380-2388.
118. Agarwal, U.P., Zhu, J.Y. and Ralph, S.A., Enzymatic hydrolysis of loblolly pine: effects of cellulose crystallinity and delignification. *Holzforschung*, 2013. **67**(4): p. 371-377.
119. Chen, H. (2014). **Biotechnology of lignocellulose**. Dordrecht: Springer.
120. Ali, I., Asim, M. and Khan, T.A., Low cost adsorbents for the removal of organic pollutants from wastewater. *Journal of environmental management*, 2012. **113**: p. 170-183.
121. Ioannidou, O. and Zabaniotou, A., Agricultural residues as precursors for activated carbon production-a review. *Renewable and Sustainable Energy Reviews*, 2007. **11**(9): p. 1966-2005.
122. Jin, H., et al., A high-performance carbon derived from corn stover via microwave and slow pyrolysis for supercapacitors. *Journal of Analytical and Applied Pyrolysis*, 2014. **110**: p. 18-23.
123. Bansal, R.C., Donnet, J.B. and Stoeckli, F. (1988). **Active Carbon**. New York: Marcel Dekker.
124. Rodriguez-Reinoso, F. and Molina-Sabio, M., Activated carbons from lignocellulosic materials by chemical and/or physical activation: an overview. *Carbon*, 1992. **30**(7): p. 1111-1118.
125. Ahmadpour, A. and Do, D.D., The preparation of active carbons from coal by chemical and physical activation. *Carbon*, 1996. **34**(4): p. 471-479.
126. Lozano-Castelló, D., et al., Influence of pore structure and surface chemistry on electric double layer capacitance in non-aqueous electrolyte. *Carbon*, 2003. **41**(9): p. 1765-1775.
127. Gryglewicz, G., et al., Effect of pore size distribution of coal-based activated carbons on double layer capacitance. *Electrochimica Acta*, 2005. **50**(5): p. 1197-1206.
128. Daud, W.M.A.W., Ali, W.S.W. and Sulaiman, M.Z., The effects of

- carbonization temperature on pore development in palm-shell-based activated carbon. *Carbon*, 2000. **38**(14): p. 1925-1932.
129. Daud, W.M.A.W. and Ali, W.S.W., Comparison on pore development of activated carbon produced from palm shell and coconut shell. *Bioresource Technology*, 2004. **93**(1): p. 63-69.
  130. Adinata, D., Daud, W.M.A.W. and Aroua, M.K., Preparation and characterization of activated carbon from palm shell by chemical activation with  $K_2CO_3$ . *Bioresource Technology*, 2007. **98**(1): p. 145-149.
  131. Jiang, J., et al., Highly ordered macroporous woody biochar with ultra-high carbon content as supercapacitor electrodes. *Electrochimica Acta*, 2013. **113**: p. 481-489.
  132. Jin, H., et al., A high-performance carbon derived from corn stover via microwave and slow pyrolysis for supercapacitors. *Journal of Analytical and Applied Pyrolysis*, 2014. **110**: p. 18-23.
  133. Li, Q.Y., et al., Novel activated carbons as electrode materials for electrochemical capacitors from a series of starch. *Solid State Ionics*, 2008. **179**(7-8): p. 269-273.
  134. Balathanigaimani, M. S., et al., Highly porous electrodes from novel corn grains-based activated carbons for electrical double layer capacitors. *Electrochemistry Communications*, 2008. **10**(6): p. 868-871.
  135. Li, X., et al., Preparation of capacitor's electrode from sunflower seed shell. *Bioresource technology*, 2011. **102**(2): p. 1118-1123.
  136. Misnon, I.I., et al., Electrochemical properties of carbon from oil palm kernel shell for high performance supercapacitors. *Electrochimica Acta*, 2015. **174**: p. 78-86.
  137. Malak-Polaczyk, A., et al., Carbon/ $\lambda$ - $MnO_2$  composites for supercapacitor electrodes. *Journal of Solid State Chemistry*, 2010. **183**(4): p. 969-974.
  138. Wang, S.X., Jin, C.C. and Qian, W.J.,  $Bi_2O_3$  with activated carbon composite as a supercapacitor electrode. *Journal of Alloys and Compounds*, 2014. **615**: p. 12-17.
  139. Zhao, C., et al., Synthesis and electrochemical properties of ordered mesoporous

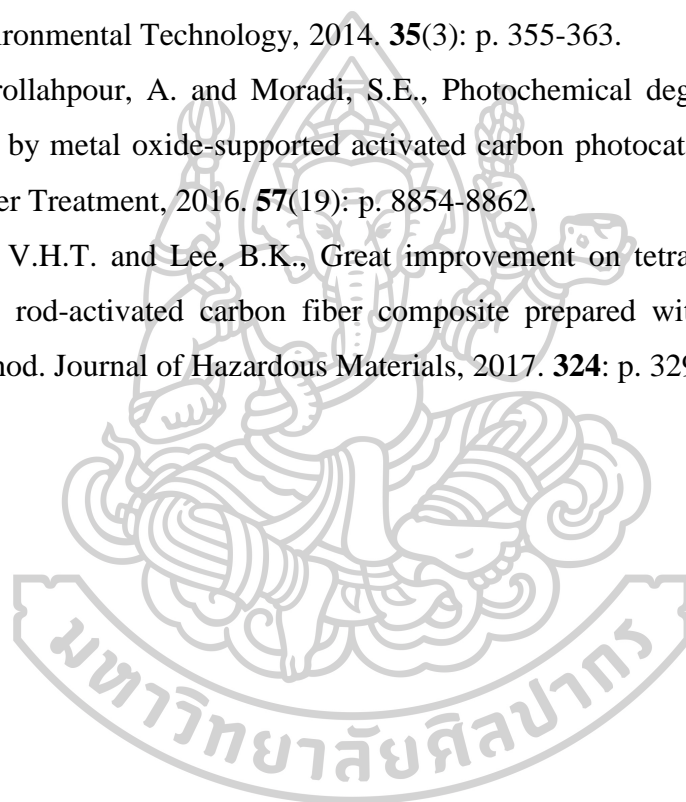
- carbon supported well-dispersed cobalt oxide nanoparticles for supercapacitor. *Materials Research Bulletin*, 2015. **64**: p. 55-60.
140. Mondal, K., Kumar, R. and Sharma, A., Metal-Oxide Decorated Multilayered Three-Dimensional (3D) Porous Carbon Thin Films for Supercapacitor Electrodes. *Industrial & Engineering Chemistry Research*, 2016. **55**(49): p. 12569-12581.
  141. Zhang, X., et al., A universal strategy for metal oxide anchored and binder-free carbon matrix electrode: A supercapacitor case with superior rate performance and high mass loading. *Nano Energy*, 2017. **31**: p. 311-321.
  142. Frackowiak, E., et al., Supercapacitor electrodes from multiwalled carbon nanotubes. *Applied Physics Letters*, 2000. **77**(15): p. 2421-2423.
  143. Chen, J. H., et al., Electrochemical characterization of carbon nanotubes as electrode in electrochemical double-layer capacitors. *Carbon*, 2002. **40**(8): p. 1193-1197.
  144. Niu, C., et al., High power electrochemical capacitors based on carbon nanotube electrodes. *Applied Physics Letters*, 1997. **70**(11): p. 1480-1482.
  145. Ma, R.Z., et al., Study of electrochemical capacitors utilizing carbon nanotube electrodes. *Journal of Power Sources*, 1999. **84**(1): p. 126-129.
  146. Kim, J.H., et al., Fabrication and electrochemical properties of carbon nanotube film electrodes. *Carbon*, 2006. **44**(10): p. 1963-1968.
  147. Vix-Guterl, C., et al., Electrochemical energy storage in ordered porous carbon materials. *Carbon*, 2005. **43**(6): p. 1293-1302.
  148. Zhang, B., et al., Electric double-layer capacitors using carbon nanotube electrodes and organic electrolyte. *Materials Letters*, 2001. **51**(6): p. 539-542.
  149. Yoon, B.J., et al., Electrical properties of electrical double layer capacitors with integrated carbon nanotube electrodes. *Chemical Physics Letters*, 2004. **388**(1-3): p. 170-174.
  150. Li, C., et al., A study of activated carbon nanotubes as double-layer capacitors electrode materials. *Materials Letters*, 2004. **58**(29): p. 3774-3777.
  151. Xu, B., et al., Room temperature molten salt as electrolyte for carbon nanotube-based electric double layer capacitors. *Journal of Power Sources*, 2006. **158**(1):

- p. 773-778.
152. Ye, J.S., et al., Preparation and characterization of aligned carbon nanotube–ruthenium oxide nanocomposites for supercapacitors. *Small*, 2005. **1**(5): p. 560-565.
  153. Reddy, A.L.M. and Ramaprabhu, S., Nanocrystalline metal oxides dispersed multiwalled carbon nanotubes as supercapacitor electrodes. *The Journal of Physical Chemistry C*, 2007. **111**(21): p. 7727-7734.
  154. Zhang, H., et al., Growth of Manganese Oxide Nanoflowers on Vertically-Aligned Carbon Nanotube Arrays for High-Rate Electrochemical Capacitive Energy Storage. *Nano Letters*, 2008. **8**(9): p. 2664-2668.
  155. Sellers, M.C., Castle, B.M. and Marsh, C.P., Three-dimensional manganese dioxide-functionalized carbon nanotube electrodes for electrochemical supercapacitors. *Journal of Solid State Electrochemistry*, 2013. **17**(1): p. 175-182.
  156. Su, Y. and Zhitomirsky, I., Hybrid MnO<sub>2</sub>/carbon nanotube-VN/carbon nanotube supercapacitors. *Journal of Power Sources*, 2014. **267**: p. 235-242.
  157. Zhang, J., et al., One-pot synthesis of a Mn(MnO)/Mn<sub>5</sub>C<sub>2</sub>/carbon nanotube nanocomposite for supercapacitors. *RSC Advances*, 2014. **4**(109): p. 64162-64168.
  158. Kao, E., et al. (2015). "**ALD titanium nitride coated carbon nanotube electrodes for electrochemical supercapacitors.**" In *Solid-State Sensors, Actuators and Microsystems (TRANSDUCERS)*, Transducers-2015 18th International Conference on 2015. IEEE.
  159. Lines, M.E. and Glass, A.M. (2001). **Principles and Applications of Ferroelectrics and Related Materials**. Oxford: Oxford University Press.
  160. Smolenskiĭ, G.A. (1984). **Ferroelectrics and related materials**, New York: Taylor & Francis.
  161. Scott, J.F., et al., Nano-phase SBT-family ferroelectric memories, *Integrated Ferroelectrics*, 1998. **21**(1-4): p. 1-14.
  162. Mathews, S., et al., Ferroelectric Field Effect Transistor Based on Epitaxial Perovskite Heterostructures. *Science*, 1997. **276**(5310): p. 238-240.

163. Park, B.H., et al., Lanthanum-substituted bismuth titanate for use in non-volatile memories. *Nature*, 1999. **401**(6754): p. 682-684.
164. Upadhyay, R.H. and Deshmukh, R.R., Investigation of dielectric properties of newly prepared  $\beta$ -phase polyvinylidene fluoride-barium titanate nanocomposite films. *Journal of Electrostatics*, 2013. **71**(5): p. 945-950.
165. Chen, S., et al., Ferroelectric poly(vinylidene fluoride) thin films on Si substrate with the  $\beta$  phase promoted by hydrated magnesium nitrate. *Journal of Applied Physics*, 2007. **102**(10): p. 104108.
166. Yang, X., et al., Spatially-confined crystallization of poly(vinylidene fluoride). *Polymer International*, 2000. **49**(11): p. 1525-1528.
167. Ma, W., Zhang, J. and Wang, X., Formation of poly(vinylidene fluoride) crystalline phases from tetrahydrofuran/N, N-dimethylformamide mixed solvent. *Journal of Materials Science*, 2008. **43**(1): p. 398-401.
168. Lebedev, S.M., Gefle, O.S. and Tkachenko, S.N., Metal-polymer PVDF/nickel composites and evaluation of their dielectric and thermal properties. *Journal of Electrostatics*, 2010. **68**(2): p. 122-127.
169. Prasad, K., et al., Electrical Conduction in 0-3 BaTiO<sub>3</sub>/PVDF Composites. *Integrated Ferroelectrics*, 2010. **117**(1): p. 55-67.
170. Hajeesaeh, S. and Muensit, S., Theory and measurements for 0-3 BaTiO<sub>3</sub>/PVDF composites. *Songklanakarin Journal of Science and Technology*, 2007. **29**(2): p. 413-418.
171. Upadhyay, R.H. and Deshmukh, R.R., A new low dielectric constant barium titanate-poly (methyl methacrylate) nanocomposite films. *Advances in Materials Research*, 2013. **2**(2): p. 99-109.
172. Li, Y.C., Tjong, S.C. and Li, R.K.Y., Dielectric properties of binary polyvinylidene fluoride/barium titanate nanocomposites and their nanographite doped hybrids. *eXPRESS Polymer Letters*, 2011. **5**(6): p. 526-534.
173. Yang, X.J., Li, J.Y. and Lei, Y.P., The Preparation and Dielectric Properties of BT/PANI/PVDF Composite. *Advanced Materials Research*, 2013. **668**: p. 17-20.
174. Wang, Y.J., et al. Preparation and Dielectric Property of Ag/PVDF Composite Film. *Advanced Materials Research*, 2014. **989**: p. 242-245.

175. Luo, B., et al., Fabrication, characterization, properties and theoretical analysis of ceramic/PVDF composite flexible films with high dielectric constant and low dielectric loss. *Journal of Materials Chemistry A*, 2014. **2**(2): p. 510-519.
176. Bunnak, N., et al., Increment of dielectric constant in binary composite based on PVDF/clay system. *Journal of Materials Science: Materials in Electronics*, 2015. **26**(9): p. 7270-7276.
177. Cho, S., Lee, J.S. and Jang, J., Enhanced Crystallinity, Dielectric, and Energy Harvesting Performances of Surface-Treated Barium Titanate Hollow Nanospheres/PVDF Nanocomposites. *Advanced Materials Interfaces*, 2015. **2**(10): p. 1500098.
178. Zhang, Z., et al., Enhancement of dielectric and electrical properties in BT/SiC/PVDF three-phase composite through microstructure tailoring. *Composites Part A: Applied Science and Manufacturing*, 2015. **74**: p. 88-95.
179. Castles, F., et al., Microwave dielectric characterisation of 3D-printed BaTiO<sub>3</sub>/ABS polymer composites. *Scientific Reports*, 2016. **6**: p. 22714.
180. Gondal, M. A., et al., Facile preparation of magnetic C/TiO<sub>2</sub>/Ni composites and their photocatalytic performance for removal of a dye from water under UV light irradiation. *Journal of Environmental Science and Health, Part A*, 2012. **47**(4): p. 570-576.
181. Zhang, X., Zhou, M. and Lei, L., Preparation of photocatalytic TiO<sub>2</sub> coatings of nanosized particles on activated carbon by AP-MOCVD. *Carbon*, 2005. **43**(8): p. 1700-1708.
182. Ao, Y., et al., Low temperature preparation of anatase TiO<sub>2</sub>-activated carbon composite film. *Applied Surface Science*, 2008. **254**(13): p. 4001-4006.
183. Ao, Y., et al., Low temperature preparation of anatase TiO<sub>2</sub>-coated activated carbon. *Colloids and Surfaces A: Physicochemical and Engineering Aspects*, 2008. **312**(2-3): p. 125-130.
184. Byrappa, K., et al., Impregnation of ZnO onto activated carbon under hydrothermal conditions and its photocatalytic properties. *Journal of Materials Science*, 2006. **41**(5): p. 1355-1362.
185. Sobana, N., Muruganandam, M. and Swaminathan, M., Characterization of AC-

- ZnO catalyst and its photocatalytic activity on 4-acetylphenol degradation. *Catalysis Communications*, 2008. **9**(2): p. 262-268.
186. Sobana, N., B. Krishnakumar, and M. Swaminathan, Synergism and effect of operational parameters on solar photocatalytic degradation of an azo dye (Direct Yellow 4) using activated carbon-loaded zinc oxide. *Materials Science in Semiconductor Processing*, 2013. **16**(3): p. 1046-1051.
187. Andriantsiferana, C., Mohamed, E.F. and Delmas, H., Photocatalytic degradation of an azo-dye on TiO<sub>2</sub>/activated carbon composite material. *Environmental Technology*, 2014. **35**(3): p. 355-363.
188. Nasrollahpour, A. and Moradi, S.E., Photochemical degradation of methylene blue by metal oxide-supported activated carbon photocatalyst. *Desalination and Water Treatment*, 2016. **57**(19): p. 8854-8862.
189. Thi, V.H.T. and Lee, B.K., Great improvement on tetracycline removal using ZnO rod-activated carbon fiber composite prepared with a facile microwave method. *Journal of Hazardous Materials*, 2017. **324**: p. 329-339.



**VITA**

**NAME** Nuntanid Phatharapeetranun

**DATE OF BIRTH** 14 May 1986

**PLACE OF BIRTH** Photharam, Ratchaburi, Thailand

**INSTITUTIONS ATTENDED** Department of Material Science and Engineering, Faculty of Engineering and Industrial Technology, Silpakorn University

**HOME ADDRESS** 98 Moo 3 Sub-district Bangtanode, District Photharam, Province Ratchaburi

**PUBLICATION**

1. Phatharapeetranun, N., Ksapabutr, B., Marani, D., Bowen, J. R. and Esposito, V., 3D-printed barium titanate/poly-(vinylidene fluoride) nano-hybrids with anisotropic dielectric properties. *Journal of Materials Chemistry C*, 2017. 5: p. 12430-12440.
2. Christophe, G., Phatharapeetranun, N., Ksapabutr, B., J.-C. Grivel and Esposito, V., Stoichiometric control in Bi<sub>4</sub>Ti<sub>3</sub>O<sub>12</sub> synthesis by novel hybrid solid state reaction. *Materials Letters*, 2017. 221: p. 101-103.
3. Pornsit, L., Phatharapeetranun, N., Ksapabutr, B., Wongkasemjit, S., Chaiyut, N., Panapoy, M., Double-layered TiO<sub>2</sub>/activated carbon films with enhanced photocatalytic activity towards methylene blue degradation. *Optoelectronics and Advanced Materials-Rapid Communications*, 2018. 12: p. 347-352.
4. Phatharapeetranun, N., et al., Assembly Three Dimensional Bismuth titanate (3D-BIT) by Extrusion-Based Fuse Deposition Modeling Technique. *Academics World: International Conference on Engineering, Technology and Innovations (IACETI)*, Bangkok, Thailand, 2017.